Lithos 162–163 (2013) 195–220

Contents lists available at SciVerse ScienceDirect

Lithos

journal homepage: www.elsevier.com/locate/lithos

# The fast evolution of a crustal hot zone at the end of a transpressional regime: The Saint-Tropez peninsula granites and related dykes (Maures Massif, SE France)

Jean-Clair Duchesne [a,*], Jean-Paul Liégeois [a,b], Olivier Bolle [a], Jacqueline Vander Auwera [a], Olivier Bruguier [c], Dmitry I. Matukov [d], Sergey A. Sergeev [d]

[a] Département de Géologie, Université de Liège, Bat. B20, B-4000 Sart Tilman, Belgium
[b] Isotope Geology, Dpt Earth Sciences, Royal Museum for Central Africa, B-3080 Tervuren, Belgium
[c] Géosciences Montpellier, Université de Montpellier II, F-34095 Montpellier, France
[d] Center of Isotopic Research, All-Russian Geological Research Institute (VSEGEI), 74 Sredny Prospect, 199106 St.-Petersburg, Russia

ARTICLE INFO

*Article history:*
Received 16 June 2012
Accepted 30 December 2012
Available online 10 January 2013

*Keywords:*
Leucogranite
Variscan orogeny
Shear zone plutonism
Mafic–felsic magma interaction
Geochemical modeling
Non-CHARAC behavior

ABSTRACT

Granite and dolerite occurring in the eastern unit of the Maures Massif (southern France Variscan belt) were emplaced in the waning stage of the evolution of a dextral shear zone along the Gondwana border with Laurasia. We present a geochronological and petro-geochemical study (major and trace elements, Sr–Nd isotopes) of (1) the foliated Moulin Blanc cordierite granite and related foliated dykes; (2) the equant Camarat granite and dyke; and (3) the andesite–basalt dolerite dykes (frequently mingled with leucogranite material at Pinet and Capon tips) and cross-cutting leucogranitic dykes. Zircon and monazite dating of the Moulin Blanc granite gives a crystallization age of 301 ± 2 Ma. SHRIMP dating on zircons from the leucogranite component of a Pinet composite dyke only reveals zircon core ages of mainly 310 ± 10 Ma (age of migmatization of the host gneiss). Undulating contacts of dolerite dykes within the *c.* 300 Ma old Camarat granite suggest penecontemporary relationships between the two intrusions. The age interval between the Moulin Blanc granite and the dolerite dykes would thus be very short. The Moulin Blanc pluton is formed by mingling and mixing of melts of granitic and dioritic composition, the latter occurring mainly as microgranular mafic enclaves. Two other types of diorites are also identified in the pluton. The foliated dykes are similar in composition to the Moulin Blanc granite, which confirms their relationship to the main pluton. The Moulin Blanc granite is a typical example of a pluton formed by repeated recharges coming from a deeper magma chamber. Formation of the Camarat dykes is controlled by hydrothermal fluids that are responsible for the non-CHARAC behavior of trace elements. The Pinet and Capon leucogranite components of the dolerite dykes have distinct geochemical signatures, different from the Camarat granite and dykes. The cross-cutting leucogranitic dykes have much geochemical similarities with the Capon granite. The age of similar dykes in the Tanneron Massif supports the contemporaneity of Camarat granite and dolerites. The dolerite geochemistry was deeply modified by alteration processes, but an andesite–basalt composition is still recognizable by using immobile element ratios. In a $\varepsilon_{Nd}$ vs. Sri diagram, all rocks plot close to a mixing hyperbola between a depleted mantle component and a crustal component, characteristic of the Variscan crust in the French Massif Central. There is a broad correlation between the $NdT_{DM}$ 2-stage model ages and the degree of fractionation of the rocks. Modeling of dehydration melting in a range of P–T conditions reveals that a variety of lithologies were the source of the Saint-Tropez magmas: high-alumina and alkali-basalt amphibolites, metagraywackes, metapelites and meta-arkoses. These sources were melted almost simultaneously at different levels in the crust. The calculated critical dyke width required to transport the granitic melt by buoyancy is far too large compared to the observed granitic dyke thicknesses. Therefore, tectonic processes and/or melt overpressure must have played a role in the emplacement mechanism. Thermo-mechanical constraints on mixing between mafic and felsic melts suggest that, in the Pinet composite dykes, both melts should have mixed. The observed lack of mixing is interpreted as due to quick cooling. The region was affected by a hot zone at the end of a transpressional regime.



## 1. Introduction

The Variscan orogeny is characterized by nappe stacking due to collision, followed by formation of large shear zones generating transpressional to transtensional regimes (Matte, 1986 and references therein). A variety of granitic intrusions were emplaced at different stages of the geodynamic evolution. Peraluminous leucogranite magmatism is commonly associated with the collision stage of an orogeny, but can also occur in post-collisional settings (Sylvester, 1998 and references therein). The present study focuses on a series of intrusions of intermediate to silicic compositions, outcropping in the Saint-Tropez

* Corresponding author. Tel.: +32 4 366 2255; fax: +32 4 366 2029.
*E-mail address:* jc.duchesne@ulg.ac.be (J.-C. Duchesne).

0024-4937/$ – see front matter © 2013 Elsevier B.V. All rights reserved.
http://dx.doi.org/10.1016/j.lithos.2012.12.019

peninsula (Maures–Tanneron Massif, SE France). These intrusions, mostly leucogranitic in composition, were emplaced in the waning stages of a shear zone regime in a very short time interval at the end of the Variscan orogeny. The magmatism illustrates several processes that are central to igneous petrology, i.e. granite formation, magma transport and emplacement (Barbey, 2009; Burgisser and Bergantz, 2011; Petford et al., 2000 and references therein). In this study, a variety of magma types are identified and characterized through a geochemical study (major and trace elements, Sr–Nd isotopes). Various differentiation mechanisms will be explored and fractional crystallization will appear as less effective than hybridization and hydrothermal fluid interaction (Bau, 1996). One of the granite intrusions brings further evidence supporting the view that granite plutons usually emplace in several pulses (e.g. Clemens et al., 2010a; Miller et al., 2011; Vigneresse, 2007). Each pulse is possibly triggered by a new influx of mafic magma in a magma chamber located at a deeper level than the level of final emplacement of the pluton. These repeated interactions between magmas of different types, typified by mingling structures, deeply modify the composition of the resident magma by hybridization. Composite doleritic dykes in which mafic and felsic materials are mingled in various proportions are good cases to model the physical interaction between the two magmas following the approach of Frost and Mahood (1987). It will also be shown that emplacement of granitic melts in thin dykes cannot be exclusively explained by buoyancy of the magma, but requires tectonic or gas overpressures in the melt.

The concept of crustal hot zone, developed by Annen et al. (2006), will prove to be a relevant framework to explain the variety of magmas from intermediate to acidic compositions produced almost simultaneously by melting different sources at various levels in the deep crust. It also accounts for the interaction of the various melts at the source, during ascent in feeder dykes, or in shallower reservoirs. Perhaps the most significant impact of the study will be to show through new U–Pb zircon ages that the intrusion and folding of a granite were very shortly followed by granite and dolerite emplacement at the end of a transpressional regime.

## 2. Geological framework

The Maures Massif and its northern prolongation, the Tanneron Massif (Fig. 1), are part of the Variscan belt which results from the collision of Laurasia and some Gondwana-affinity microplates (Carosi et al., 2012; Guillot and Ménot, 2009; Matte, 2001). The Maures Massif is made up of three metamorphic units: a western unit formed by low-grade metasediments, a central unit composed of micaschists, amphibolites and gneisses, and an eastern unit essentially made up of migmatitic gneisses and granites. The latter two units are separated by the Grimaud fault, a major strike-slip fault (Vauchez and Bufalo, 1988) which is displaced westward by a late fault in the Saint-Tropez gulf and which is continued by the Joyeuse fault in the Tanneron Massif.

The polyphased tectonometamorphic evolution of the Maures–Tanneron Massif is complex (Bellot, 2005; Corsini and Rolland, 2009; Rolland et al., 2009) and belongs to the Southern Variscides evolution marked by high-grade metamorphism and abundant post-collisional magmatism between 325 and 290 Ma, with, in Spain, the maximum granitic activity between 313 and 298 Ma (Orejana et al., 2012 and references therein). This major event would result from the clockwise rotation of Gondwana relative to Laurasia, yielding large en echelon strike-slip faults from Central Europe to northern Africa (Matte, 2001). The Maures–Tanneron Massif evolution started with the development of a rift environment, with bimodal magmatism, in a Pre-Variscan extensional setting and was followed by subduction. A frontal collision in Variscan times induced the first phase of deformation ($D_1$) characterized by isoclinal folding and nappe stacking in amphibolite facies metamorphism. The next deformation phases are characterized by isoclinal folding and backthrusting ($D_2$ phase), then formation of large-scale upright folds coeval with dextral ductile shearing (Corsini and Rolland, 2009; Rolland et al., 2009) centered on N10W to N20E trending major strike-slip shear zones (the Grimaud–Joyeuse Fault and, in the Tanneron Massif, the La Moure fault; Fig. 1) ($D_3$ phase). The $D_2$ and $D_3$ phases may be ascribed to orogen-parallel shearing in a transpressional regime due to oblique convergence, typical of a post-collisional period (Liégeois et al., 1998 and references therein). Doming and ductile to brittle normal faulting, accompanied by a low-pressure retrograde metamorphism characterize the last phase of deformation ($D_4 = D_{4-5}$ phase of Bellot, 2005). During this phase, the eastern unit was intruded by several granites, the region was rapidly exhumed and intracontinental basins were formed along the Grimaud–Joyeuse and La Moure faults (Fig. 1). After Bellot (2005), the $D_4$ phase typifies a syn- to postorogenic extensional regime, whereas, following Corsini and Rolland (2009) and Rolland et al. (2009), it corresponds to a late phase of the transpressional tectonics.

The eastern unit of the Maures Massif, in which the granites studied here are localized, is made up of migmatitic paragneisses, orthogneisses, remnants of amphibolitized eclogites, and anatectic granites. Migmatization is dated at 331 ± 3 Ma (U–Pb monazite; Moussavou, 1998) in the Eastern Maures and at 317 ± 1 Ma (U–Pb monazite) in central Tanneron (Demoux et al., 2008), the last authors accepting that migmatization could have lasted 14 myr. The Plan-de-la-Tour granite and its northern prolongation, the Rouet granite, which form the largest granitic pluton of the Maures–Tanneron Massif (Fig. 1) emplaced at 302 ± 4 Ma (U–Pb monazite age of the Rouet granite; Demoux et al., 2008), along the *c.* N–S Grimaud–Joyeuse Fault. The E–W elongated Camarat granite has been dated at 297 ± 5 Ma (Rb–Sr on whole rocks), an age initially determined by Roubault et al. (1970) and recalculated by Amenzou (1988). This age is consistent within error with biotite and muscovite $^{39}Ar/^{40}Ar$ plateau ages of 299.4 ± 0.6 Ma and 300.2 ± 0.6 Ma respectively obtained on biotite and muscovite from the granite (Morillon et al., 2000). The whole eastern unit of the Maures Massif has been exhumed rapidly after the intrusion of the Camarat granite and, according to $^{39}Ar/^{40}Ar$ plateau ages, has crossed the 400 °C–450 °C isotherm between 306.0 ± 2.4 Ma and 300.0 ± 1.0 Ma (Morillon et al., 2000). Finally, the Eastern Maures is crosscut by E–W trending dolerite dykes, grossly parallel to the Camarat granite and to a graben of Permian age that separates the Maures and Tanneron Massifs. An attempt to date these dolerite dykes turned out to be unsuccessful (Zheng et al., 1992).

## 3. The post-collisional intrusions: dykes and granites

The post-collisional intrusions of the Maures Massif, which are the focus of this study, are (in relative age order): the Moulin Blanc foliated granite and folded granitic dykes, the Camarat granite and dykes, and doleritic dykes, some of them being composite associating mafic and felsic material. These intrusions have been studied and sampled along the coastline of the Saint-Tropez peninsula, where they are superbly displayed (Fig. 2): (1) along the seashore, east of Saint-Tropez, where various facies of the Moulin Blanc granite outcrop; (2) in the section from the Capon tip to the Pampelonne cove passing through the Pinet tip, characterized by doleritic composite dykes parallel to thin granitic dykes and by folded granitic dykes; and (3) the Camarat granite along the cliffs of the Camarat cape with cross-cutting dolerite dykes and, at its northern contact with the enclosing gneisses, offshoots of granitic dykes.

### 3.1. The Moulin Blanc granite and associated foliated dykes

The muscovite-bearing Moulin Blanc granite is strongly foliated (subvertical, *c.* N–S striking penetrative foliation, parallel to the foliation in the gneissic country rocks) and typically shows patches of a weathered out cordierite. Under the microscope, plagioclase is euhedral, unzoned, uniformly saussuritized and undeformed. Quartz is interstitial relative to plagioclase and is the only mineral showing evidence of

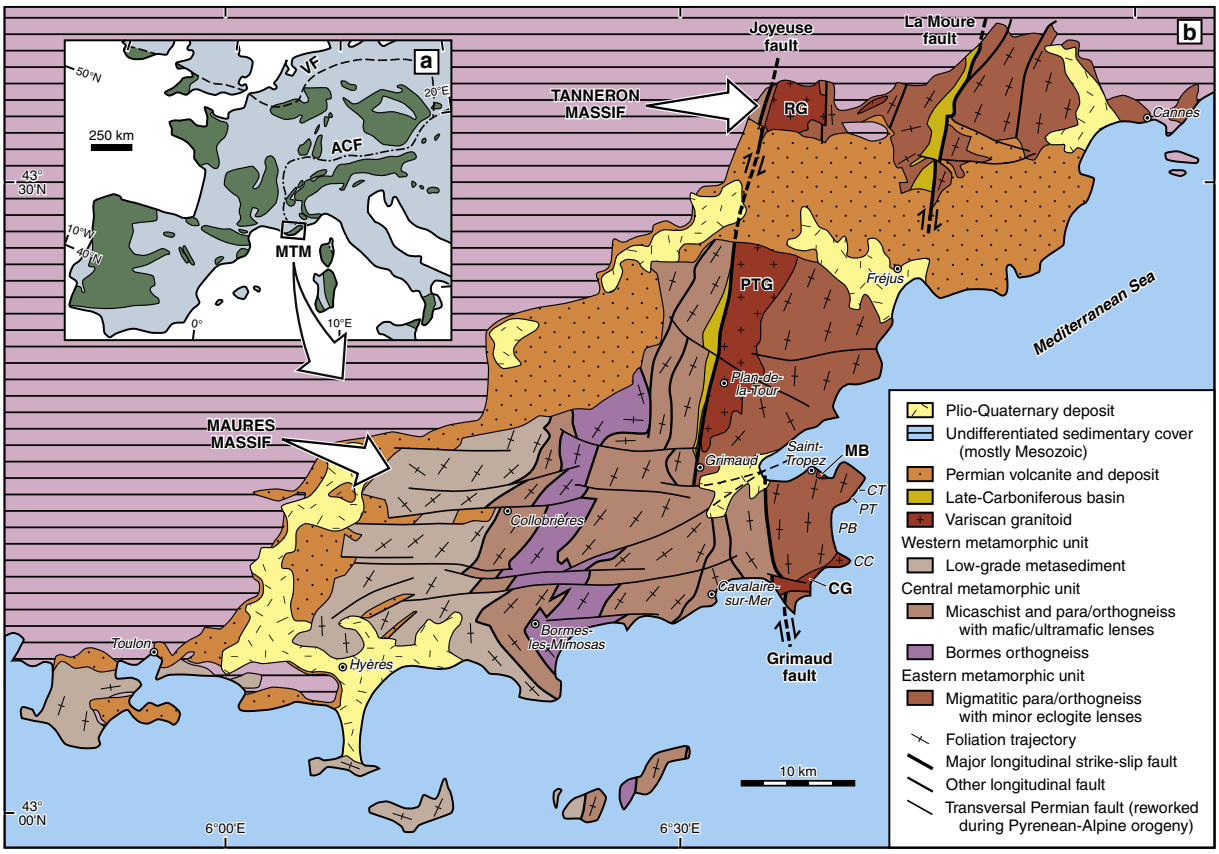


**Fig. 1.** (a). Distribution map of Variscan and/or older basement areas in Western Europe, with location of the Maures–Tanneron Massif (MTM; simplified from von Raumer et al., 2002); VF, Variscan deformation Front (after Franke, 1989); ACF, present-day Alpine–Carpathian deformation Front (after Cavazza et al., 2004). (b) Simplified geological map of the Maures–Tanneron Massif (modified from Rouire, 1979a,b, with additional structural data from Bellot (2005), Corsini and Rolland (2009) and references therein). Granite plutons to the east of the Grimaud–Joyeuse Fault, from north to south: RG: Rouet granite; PTG: Plan-de-la-Tour granite; MB: Moulin Blanc granite; CG: Camarat granite. Abbreviations along the Saint-Tropez peninsula coastline, from north to south: CT: Capon tip; PT: Pinet tip; PB: Pampelonne cove; CC: Camarat cape.

deformation (occurrence of subgrains) and dynamic recrystallization into small new grains. K-feldspar develops poikilitic grains including plagioclase and quartz. Large crystals of muscovite, formed early in the crystallization sequence, clearly belong to the primary association. Biotite is less abundant and usually chloritized. Andalusite (up to 5 mm), tourmaline and cordierite are scarce. Apatite and zircon are trace minerals.

The granite is associated with various types of granodiorites that are made up of various proportions of two constituents: (i) a matrix (0.25–0.5 mm) of plagioclase, quartz, (chloritized) biotite, secondary muscovite (associated with alteration products) and apatite; and (ii) phenocrysts (up to 2.5 mm) of plagioclase with a sharply defined saussuritized core rimmed by clear plagioclase, with local evidence of resorption. The amount of plagioclase phenocrysts increases with the mafic character. This typically suggests hybrid rocks in which plagioclase is mixed with other components.

Swarms of rounded enclaves of more mafic material than the host rocks, usually finer-grained (microgranular mafic enclaves, MME) and flattened in the foliation plane, are conspicuous (Fig. 3A). Some of the MME themselves contain darker enclaves (nested enclaves) (Fig. 3B). A massive (apparently unfoliated) diorite crosscuts the foliated granitoids. This occurrence, together with the various MME shows that several dioritic melts have played a role at different stages of the formation and deformation of the Moulin Blanc body.

Foliated and folded granitic dykes outcrop in the Pinet–Capon section (Fig. 3D). The foliated character and the presence of weathered-out cordierite are indicative of their relationship with the Moulin Blanc granite, though their direct connections with the main body have not been observed. Another typical foliated dyke (sample #91M4) has also been sampled further south, at the Bonne Terrasse tip, north of the Camarat granite (Fig. 2).

### 3.2. The Camarat granite and dykes

The Camarat leucogranite is made up of several facies (Amenzou and Pupin, 1986). We have focused on the main type (which outcrops in the area of the Camarat Cape) and on related dykes, which crosscut the granite itself and the surrounding gneissic rocks close to the contact. The granite is equigranular (*c.* 0.5–1 cm) and isotropic. Plagioclase is euhedral, zoned ($An_{25-05}$) and saussuritized. K-feldspar is subhedral (Carlsbad twinning) and perthitic, and contains plagioclase and quartz inclusions. Quartz is mainly interstitial, but may also develop larger subspherical grains with embayments. Biotite, partly chloritized, sometimes with prehnite, contains inclusions of apatite, zircon and opaques. Muscovite is essentially of secondary origin, primary grains being very rare in the analyzed samples. Fluorite clearly associated with secondary muscovite has been observed.

The dykes have the same mineralogy as the granite, but are finer-grained and more leucocratic. They tend to develop a porphyritic texture with phenocrysts (up to 0.5 cm) of rounded quartz and euhedral feldspars in a quartzo-feldspathic matrix.

### 3.3. The dolerite dykes and associated granites (Pinet and Capon tips)

Up to 10-m-thick dolerite dykes cut across the Camarat granite. Noteworthily, some of them have undulating contacts with the granite, which suggests that they emplaced shortly after the granite, when the latter was still soft and not completely solidified. A series of thinner

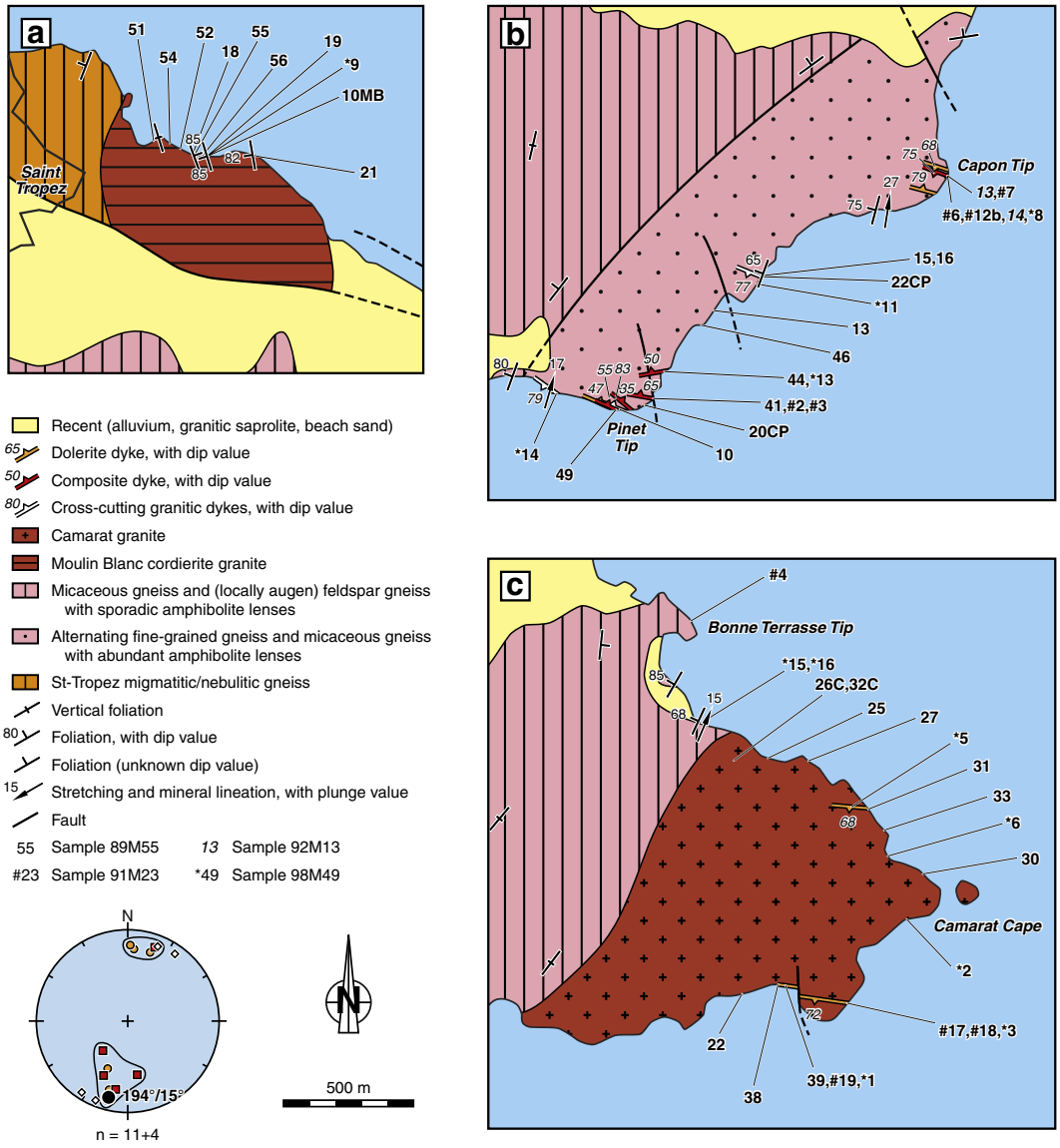


**Fig. 2.** Geological maps of the study areas (after Bordet et al., 1967) with location of the samples: (a) Moulin Blanc granite, (b) Pinet–Capon section, (c) eastern tip of the Camarat granite (area of Camarat Cape). Foliation and lineation measurements are from this study, except vertical foliations in the hinterland and foliations with unknown dip values (from Bordet et al., 1967). An equal-area projection (lower hemisphere) shows the poles of six dolerites dykes (dots), five composite dykes (squares) and four cross-cutting granitic dykes (diamonds) from (b) and (c); the average orientation of the dolerite and composite dykes is also displayed (large dot).

dolerite dykes also outcrop around the Pinet tip, where they cut across the country gneisses. Most of them are composite dykes in which doleritic and leucogranitic materials are mingled. Interestingly, the proportion of the two components may vary from dyke to dyke (Fig. 4). In some cases, the granitic component is absent or in minor amount at the contacts with enclosing rocks (Fig. 4B and C). In other cases the granitic component dominates over the dolerite, which itself forms chilled pillows (Fig. 4A and E). These dyke structures have been reported in numerous locations (see e.g. Wiebe et al., 2002) and clearly indicate mingling of two different magmas. Typically, the dolerite has a hyalophitic texture with microlithic plagioclase, clinopyroxene, oxides, needles of apatite, and secondary chlorite in a microcrystalline matrix.

The leucogranitic component of the Pinet composite dykes, here called the Pinet granite, has a fine-grained texture with early crystallized rounded quartz, euhedral stocky saussuritized plagioclase and larger interstitial K-feldspar developing a poikilitic texture in a finer grained matrix (0.25 mm). A characteristic graphic texture can develop around the feldspars. Thin early-crystallized biotite (with pleochroic halos) is the main mafic mineral, muscovite being usually secondary. Small corroded garnet grains are not rare.

At the Capon tip, a spectacular composite dyke has been studied (Fig. 5). The granitic component contains a large doleritic pillow, which nearly obstructs the dyke width, and itself contains a “septum” of leucotonalite. The dolerite resembles the Pinet and Camarat dolerites except for some minor quantities of biotite and interstitial quartz. The granitic component of the Capon composite dyke (Capon granite for short) has a similar mineralogy and texture to the Pinet granite, but K-feldspar is less abundant, graphic texture is less developed, and biotite, primary muscovite and garnet are ubiquitous accessory minerals. The leucotonalite (sample #91M12B) shows a very peculiar texture with radiating plagioclase (Fig. 5) with high aspect ratios (up to 1:10) contrasting with the more stubby habit of the plagioclase in the granite enveloping the dolerite. Following Lofgren (1980), this feature suggests that the leucotonalitic melt was strongly superheated in contact with the dolerite and then quickly undercooled when the dolerite emplaced in the colder country gneiss.

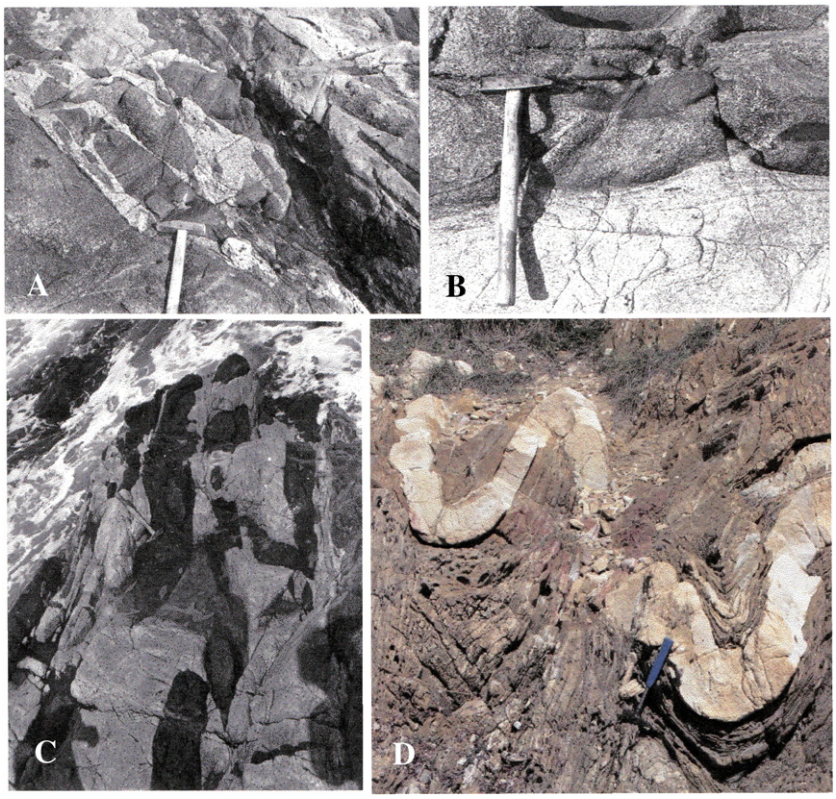


**Fig. 3.** Photographs of structures observed in the Moulin Blanc granite (seacoast east of Saint-Tropez) and of an example of folded granitic dyke (Pinet–Capon section). (A) Mingling relationships between dioritic and granodioritic material. Rounded microgranular mafic enclaves (MME), mingled with granodiorite, are elongated parallel to the contact with a diorite. (B) Dark MMEs are contained in a diorite that is itself in contact with a granodiorite. Note the lobate contacts and the foliation developed in the granodiorite parallel to the contact. (C) A swarm of MME in granite. All enclaves are flattened parallel to the foliation in the granite. Hammer in A, B and C is 40 cm-long. (D) Folded granitic dyke in gneisses. The $D_3$ deformation has folded the dyke and enclosing gneisses and a subvertical axial plane foliation has developed in the dyke. On the right, the dyke was emplaced parallel to the gneiss foliation (opportunistic dyke) and, on the left, it clearly cuts across the foliation. Hammer is 30 cm-long.

The orientation of composite and dolerite dykes from the Pinet–Capon section, as well as the orientation of dolerite dykes cutting across the Camarat granite were carefully measured. The dykes are E–W to SE–NW-striking, with moderate to steep dips (average of 104N75; Fig. 2). The less inclined dykes would correspond to dykes oblique to the $\sigma_3$ principal paleostress, either tension-shear dykes, equivalent to normal faults given their orientation, or dykes for which the magma was injected into preexisting fractures ("passive" dykes), whereas the steepest dykes would be classical pure tension dykes perpendicular to $\sigma_3$ (Geoffroy and Angelier, 1995).

Noteworthily, in the Pinet–Capon section, thin granitic dykes crosscut the foliation of the enclosing gneisses at high angle (Fig. 4D), parallel to the steepest dolerite and composite dykes (Fig. 2). Under the microscope, they resemble the Capon granite described above, particularly with small garnet grains (sample #98M14). Primary muscovite is conspicuous and andalusite is locally present. We call these dykes "cross-cutting leucogranitic dykes" in the following discussions. We will show below that some of these dykes are geochemically identical with the Capon granite. This strongly suggests that the granitic component of the composite dyke (Capon granite) could intrude independently of the dolerite material.

## 4. Zircon and monazite dating results

For U–Pb dating, zircon and monazite grains were extracted from rock samples and separated by conventional techniques (see Appendix A, which also describes the complete analytical procedure of the U–Pb dating).

### 4.1. Moulin Blanc granite

Zircon and monazite from one sample of the Moulin Blanc granite (sample #89M55; Fig. 2) have been analyzed for U–Pb dating by laser ICP-MS. The 18 analyzed zircons are concordant and give a well-constrained age of 301 ± 2 Ma (Fig. 6). The relatively high MSWD of concordance (6.1) is due to a slight shift to the right of the concordia resulting from higher uncertainties on the measurement of the $^{207}Pb$ isotope at these relatively young ages. The $^{206}Pb/^{238}U$ weighted mean age is 301 ± 2 Ma (MSWD = 0.4), i.e., identical to the concordia age. This age can thus be considered as dating the emplacement and crystallization of the Moulin Blanc granite. The 16 analyzed monazites are also concordant and give a similar well-constrained age of 300 ± 1 Ma with a low MSWD of concordance (1.1), although located slightly to the left of the concordia. The $^{206}Pb/^{238}U$ mean age is identical at 300 ± 1 Ma (MSWD = 1.1).

These ages are within error identical to the $^{39}Ar/^{40}Ar$ plateau age (301.5 ± 1.2 Ma; 2σ) obtained on a single muscovite grain by Morillon et al. (2000). This shows that the crystallization of the granite could be quickly followed by exhumation through the 400 °C–450 °C white mica closing isotherm, confirming rapid cooling. This means that the age of 301 ± 2 Ma can be considered as an excellent estimate of the emplacement of the Moulin Blanc granite.

### 4.2. Pinet granite

Within the leucogranitic component of the Pinet composite, zircons are scarce and of small size, rendering them difficult to separate. Ten zircons separated from granitic sample #92M11 have been

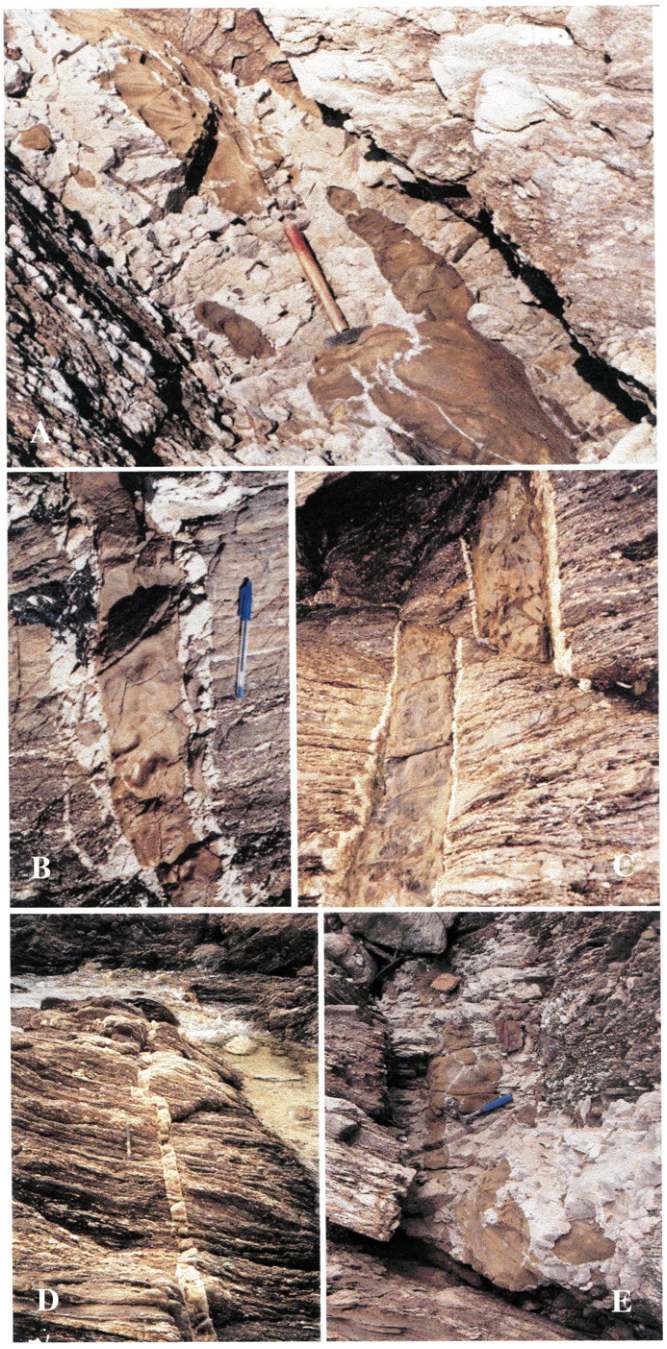


**Fig. 4.** Photographs of dykes around the Pinet tip. (A) Composite dyke in which the granitic component dominates over the doleritic component. Doleritic pillows are elongated parallel to the walls and locally invaded by flame structures and thin dykelets of granitic melt. In this outcrop, the fraction of mafic rock in the dyke is $x_{maf} = 0.35$. A model of evolution of this system is developed in Fig. 18. At the equilibrium temperature (*c.* 1000 °C), both melts have similar viscosities, a favorable condition for mixing and hybridization. Hammer is 40 cm-long. (B) Dolerite dyke with granitic material mingled with doleritic pillows at both walls. Note the thin offshoot of granite on the left and the thin elongated dolerite pillow at the right contact. Pen is 18 cm-long. (C) Doleritic dyke with veneers of granite at both contacts with enclosing gneisses. The proportion of mafic rock is $x_{maf}$ ~0.85. According to the model developed in Fig. 18, at ca. 1200 °C, the temperature of equilibrium between the two components, the granitic melt is highly superheated. The dyke is ca. 40 cm-thick. (D) Cross-cutting leucogranitic dyke at high angle with the foliation in the migmatitic gneisses (sample #89M10). The dyke thickness is ca. 10 cm. Hammer is 35 cm-long. (E) Another example of mafic–felsic association in a composite dyke. Rounded doleritic pillows and thin granitic dykelets dissecting pillows (close to hammer). Hammer is 30 cm-long.

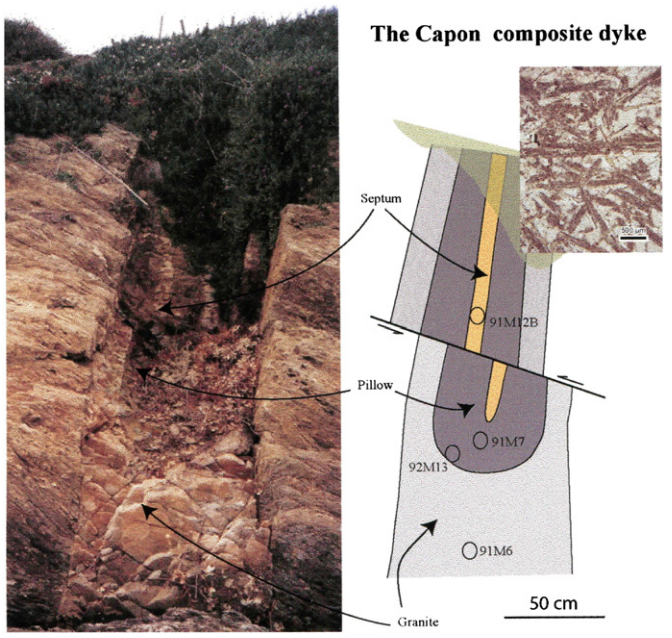


**Fig. 5.** Photograph of the Capon composite dyke and sketch showing the relationships between the granitic component, the doleritic pillow and the tonalitic "septum" within the dolerite pillow. The dyke is cut across by a subhorizontal fault. The outcrop is partly covered by vegetation masking the observed contacts shown on the sketch. In the inset is a photo in plane-polarized light of the leucotonalite showing the peculiar texture of (saussuritized) plagioclase with high aspect ratio. The scale bar is 500 μm.

analyzed by SHRIMP (Fig. 6). Five concordant zircons give an age of 310 ± 10 Ma (MSWD = 0.23). Older ages of 512 ± 10 Ma (2 zircons, MSWD = 0.0003) and 1015 ± 52 Ma (1 zircon, MSWD = 0.001) are also determined. The remaining 2 zircons are discordant and do not provide well constrained ages; their $^{206}Pb/^{238}U$ ages are in the 550–500 Ma age range, implying an inherited character.

The 1015 ± 52 Ma and 512 ± 10 Ma are clearly inherited ages. Ages at the end of the Stenian period are known in detrital zircons in the Cambrian of Sardinia (Avigad et al., 2012 and references therein). Such ages are rare in Saharan Africa and mainly known as zircon xenocrysts in the Arabian–Nubian Shield (Stern et al., 2010). However, small still unknown exotic terranes cannot be precluded. The 512 ± 10 Ma age could be related to the Pre-Variscan extensional setting that occurred along the north Gondwana margin during the Cambrian times and that has led to the drifting of the Peri-Gondwanan terranes (e.g. Cocks and Torsvik, 2006). Bimodal magmatism related to early stages of this protracted event is indeed known in the Western Maures (548 +15/−7 Ma felsic volcanic rock from a leptyno–amphibolitic complex; U–Pb zircon age; Innocent et al., 2003). The younger age of 310 ± 10 Ma can correspond either to the emplacement age of the dyke or to other inherited zircons. A close inspection revealed that Pinet zircons are rimmed by a thin border, most probably formed when the dyke crystallized. They are too thin to be dated, but we postulate that they are younger: dykes, due to their rapid emplacement and to their fine-grained habit, rarely develop independent zircon crystals, magmatic zircon being represented by thin rims on preexisting, inherited, crystals. This can be demonstrated when some rims are large enough to be dated (e.g. Tin Amali dykes, Algeria; Fezaa et al., 2010). In addition, when dykes are emplaced using the same "plumbing" system as previous plutons, they often contain slightly older zircons from earlier magma batches (Fezaa et al., 2010). We thus infer that the spots giving the 310 ± 10 Ma age belong to zircon cores inherited from the source rocks and/or caught from wall rocks during ascent. It should be pointed out here that, as already reported above, the age of migmatization of the enclosing gneiss falls in the interval 331–317 Ma (Demoux et al., 2008), and also that a syntectonic leucogranite vein (sample TGD-01; Demoux

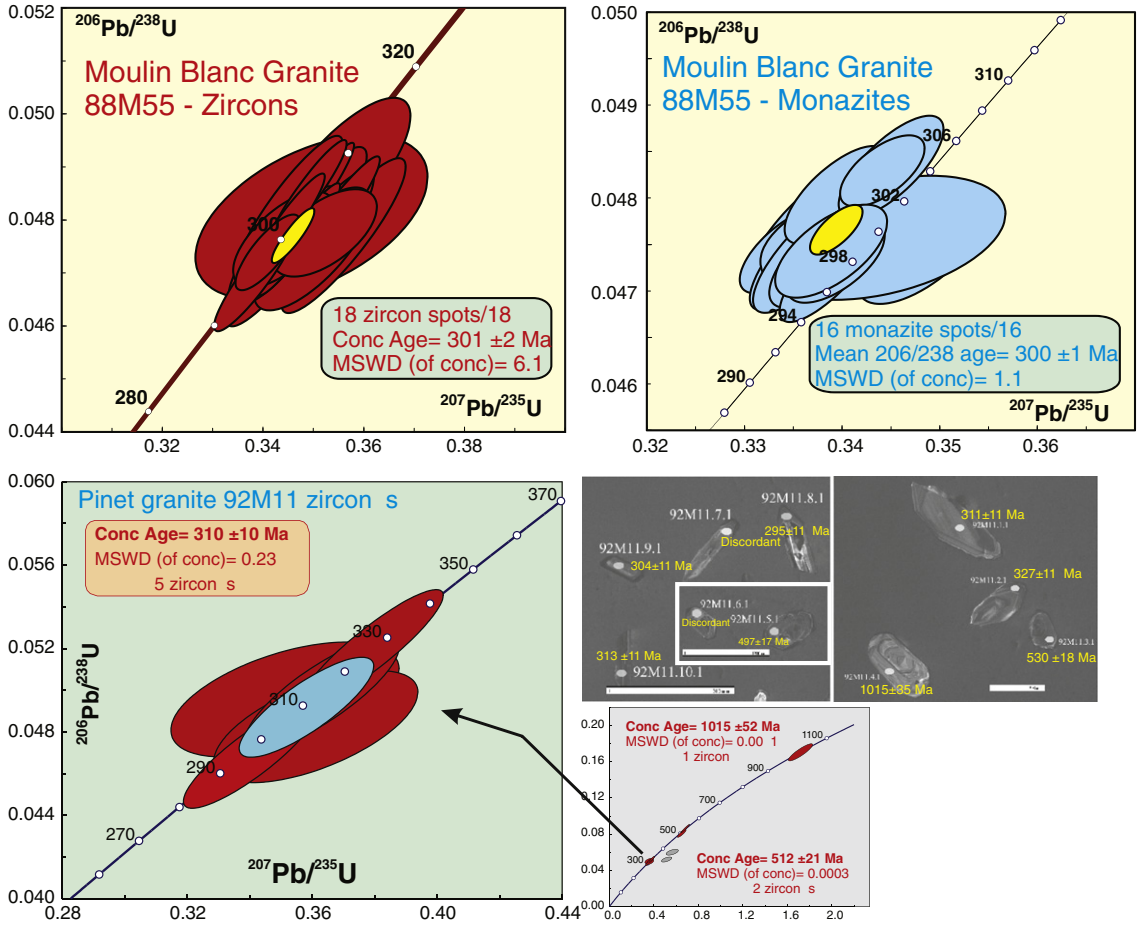


**Fig. 6.** Zircon and monazite U–Pb ages. (upper two diagrams) Zircon and monazite U–Pb ages (laser ICP-MS) for the Moulin Blanc granite (Concordia diagrams). Zircon and monazite ages are identical within error limits and represent the age of intrusion of the Moulin Blanc granite. (lower diagrams and photos) Zircon SHRIMP U–Pb ages from the Pinet granite concordia diagram and CL-images of some of the dated zircons. All dated zircons are inherited, emplacement of the Pinet granite being at *c.* 300 Ma (see text).

et al., 2008) in the migmatitic gneisses of the Tanneron Massif gave an age of 309 ± 5 Ma.

Consequently, the age of crystallization of the Pinet composite dykes cannot be directly determined. However, considering that some dolerite dykes have undulating contacts with the Camarat granite, we may infer that the system of dolerite dykes, including the Pinet and Capon composite dykes, was penecontemporaneous with the Camarat granite dated at 300.2 ± 0.6 and 299.4 ± 0.6 (Ar–Ar on biotite and muscovite, respectively; Morillon et al., 2000). Interestingly, Demoux et al. (2008) have studied a leucogranitic dyke in the Tanneron Massif (sample BOC-01) "which cross-cuts, at high angle, the foliation of the host migmatitic augengneiss". This dyke has a monazite U–Pb age of 297.1 ± 4.9 Ma, and the same petrographical characteristics as the Pinet–Capon cross-cutting leucogranitic dykes (including small garnet grains) that we consider to be contemporaneous with the composite dykes. All these observations suggest that the Pinet and Capon composite dykes emplaced at *c.* 300 Ma.

This would imply a very short period of time (302–299 Ma, taking into account analytical errors) for the whole late-Variscan magmatic evolution of the Saint-Tropez peninsula (emplacement of the Moulin Blanc and Camarat granites, and associated dykes). This age span corresponds to the Gzhelian stage (from 303.4 ± 0.9 to 299.0 ± 0.8 Ma; International Commission on Stratigraphy 2010; http://www.stratigraphy.org/column.php?id=Chart/Time Scale), the very end of the Carboniferous Period. This short period fits the age of the Plan-de-la-Tour–Rouet granite emplaced along the Grimaud–Joyeuse Fault (302 ± 4 Ma; Demoux et al., 2008), and the age of the leucogranitic dyke from the Tanneron Massif quoted above (297 ± 5 Ma; Demoux et al., 2008). It is close to the age of late-Variscan granites from Corsica and the external crystalline massifs of the western Alps (307–295 Ma; references in Corsini and Rolland, 2009; Demoux et al., 2008), and also close to the age of 306–300 Ma found for late-Variscan granites in the Cevennes (French Massif Central; Brichau et al., 2008; Bruguier et al., 2003a,b).

## 5. Geochemical data

A collection of 27 samples from the Moulin Blanc granitoids and foliated dykes, 12 samples from the Camarat pluton and dykes, 7 samples of granitic components of the Pinet–Capon composite dykes, a sample of the leucotonalitic component of the Capon composite dyke, and 4 samples of cross-cutting leucogranitic dykes in the Pinet–Capon section have been analyzed for major and trace elements following methods described in the Appendix A.

The geochemical approach will document various types of magmas, decipher several differentiation mechanisms and make possible the definition of rheological properties of melts.

### 5.1. Major and trace elements

#### 5.1.1. The Moulin Blanc pluton and foliated dykes

The geochemical composition of the Moulin Blanc samples are plotted on Harker diagrams (Fig. 7) and representative analyses are reported in Table 1. The series of rocks shows a peraluminous character (Table 1) and the samples with $SiO_2$ >71% and B* values of Debon and Le Fort (1988) <10 are leucogranites. On Harker diagrams, three types of diorites

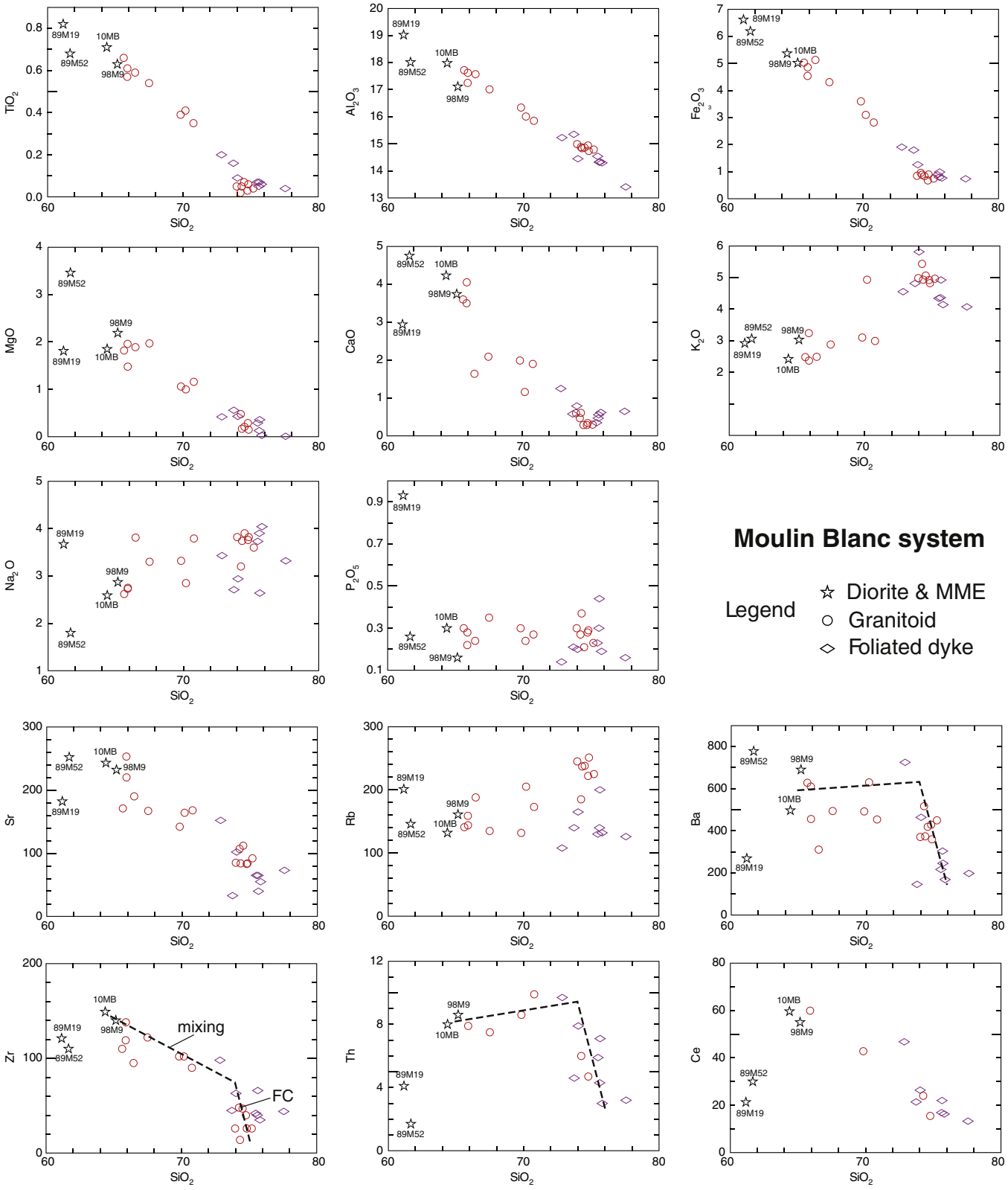


**Fig. 7.** Harker diagrams for the Moulin Blanc series of rocks and the foliated granitic dykes. The dashed lines in the Ba, Th and Zr diagrams suggest a mixing trend from sample #10MB to a 74% $SiO_2$ granite followed by fractional crystallization in the granite compositions. Major elements in wt.%; trace elements in ppm. Data in Table 1.

can be identified: (i) MMEs represented by samples #10MB and #98M9; (ii) a foliated diorite (#89M19); and (iii) the massive diorite (#89M52). The three diorite types differ by their Mg, Ca, P, Th, Nb and Ce and Y contents (Fig. 7). On the other hand, their REE distributions are similar, with relatively high $[La/Yb]_N$ ~10, which is distinctive when compared to the other rock types which have ratio values between 3 and 5 (Fig. 8; Table 1).

The Moulin Blanc granite and granodiorite plot on or close to linear arrays (Fig. 7) starting at the dioritic MME #10MB (64% $SiO_2$) and ending

**Table 1**
Major and trace element composition of selected samples of Moulin Blanc granite and associated foliated dykes.

| | Moulin Blanc pluton | | | | | | | | | | Foliated dykes | | | | | |
|---|---|---|---|---|---|---|---|---|---|---|---|---|---|---|---|---|
| | | | MME | MME | | | | | | | B. Ter. | Pinet | | | | |
| | 89M19 | 89M52 | 10-MB | 98M9 | 89M55 | 89M18 | 89M51 | 89M54 | 89M56 | 89M21 | 91M4 | 89M13 | 89M15 | 89M16 | 98M11 | 20CP |
| $SiO_2$ | 60.92 | 61.57 | 64.56 | 64.67 | 65.69 | 67.29 | 69.82 | 70.58 | 74.18 | 75.20 | 73.31 | 73.42 | 75.34 | 75.33 | 76.86 | 75.80 |
| $TiO_2$ | 0.82 | 0.68 | 0.71 | 0.63 | 0.61 | 0.54 | 0.39 | 0.35 | 0.02 | 0.03 | 0.20 | 0.16 | 0.05 | 0.07 | 0.04 | 0.06 |
| $Al_2O_3$ | 18.94 | 17.99 | 18.03 | 16.98 | 17.56 | 16.96 | 16.33 | 15.81 | 14.87 | 15.03 | 15.33 | 15.28 | 14.27 | 14.51 | 13.29 | 14.30 |
| $Fe_2O_3t$ | 6.59 | 6.18 | 4.85 | 4.99 | 4.84 | 4.29 | 3.60 | 2.81 | 0.96 | 0.68 | 1.92 | 1.79 | 0.80 | 0.89 | 0.73 | 0.77 |
| MnO | 0.10 | 0.11 | 0.16 | 0.08 | 0.08 | 0.06 | 0.06 | 0.08 | 0.03 | 0.04 | 0.02 | 0.10 | 0.05 | 0.06 | 0.05 | 0.05 |
| MgO | 1.80 | 3.46 | 1.86 | 2.17 | 1.48 | 1.96 | 1.06 | 1.16 | 0.48 | 0.29 | 0.42 | 0.56 | 0.13 | 0.29 | 0.01 | 0.03 |
| CaO | 2.93 | 4.75 | 4.24 | 3.71 | 4.03 | 2.08 | 1.99 | 1.90 | 0.47 | 0.29 | 1.26 | 0.58 | 0.47 | 0.35 | 0.64 | 0.62 |
| $Na_2O$ | 3.66 | 1.79 | 2.60 | 2.85 | 2.74 | 3.29 | 3.32 | 3.78 | 3.20 | 3.78 | 3.45 | 2.70 | 3.89 | 3.72 | 3.29 | 4.04 |
| $K_2O$ | 2.91 | 3.05 | 2.43 | 3.00 | 2.37 | 2.87 | 3.10 | 2.98 | 5.42 | 4.95 | 4.58 | 4.79 | 4.34 | 4.33 | 4.03 | 4.14 |
| $P_2O_5$ | 0.93 | 0.26 | 0.30 | 0.16 | 0.28 | 0.35 | 0.30 | 0.27 | 0.27 | 0.28 | 0.14 | 0.21 | 0.30 | 0.23 | 0.16 | 0.19 |
| Total | 99.60 | 99.85 | 99.74 | 99.25 | 99.69 | 99.70 | 99.98 | 99.72 | 99.90 | 100.57 | 100.63 | 99.58 | 99.64 | 99.79 | 99.10 | 100.00 |
| LOI | 1.67 | 2.60 | | 1.05 | 1.07 | 2.00 | 1.60 | 1.30 | 1.00 | 1.07 | 0.91 | 1.21 | 0.99 | 0.97 | 1.00 | |
| U | 3.7 | 2.0 | 4.0 | 3.8 | 3.0 | 2.5 | 3.8 | 3.3 | 5.7 | 5.9 | 4.5 | 5.5 | 2.8 | 2.9 | 4.5 | 3.4 |
| Th | 4.0 | 1.7 | 8.0 | 8.6 | 8.0 | 7.5 | 8.0 | 10.0 | 6.0 | 4.7 | 9.7 | 4.6 | 4.3 | 5.9 | 3.2 | 3 |
| Zr | 121 | 110 | 149 | 140 | 138 | 122 | 102 | 90 | 48 | 40 | 98 | 45 | 40 | 42 | 44 | 35 |
| Hf | | | 3.4 | 3.4 | | | | | 2.1 | 1.5 | 3.2 | | | | 2 | 2.2 |
| Nb | 35 | 9 | 10 | 9 | 10 | 12 | 9 | 9 | 8 | 10 | 10 | 14 | 11 | 13 | 10 | 16 |
| Ta | | | 2.0 | 0.8 | | | | | 1.4 | 4.1 | 1.0 | | | | 3.3 | 3.4 |
| Rb | 200 | 146 | 132 | 161 | 144 | 135 | 132 | 173 | 185 | 222 | 109 | 140 | 140 | 130 | 126 | 134 |
| Sr | 182 | 252 | 243 | 232 | 220 | 167 | 142 | 168 | 107 | 83 | 149 | 33 | 65 | 65 | 73 | 61 |
| Ba | 269 | 778 | 497 | 690 | 456 | 494 | 492 | 454 | 517 | 429 | 725 | 146 | 304 | 217 | 198 | 169 |
| Rb/Sr | 1.1 | 0.58 | 0.54 | 0.69 | 0.65 | 0.81 | 0.93 | 1.0 | 1.7 | 2.7 | 0.73 | 4.2 | 2.2 | 2.0 | 1.7 | 2.20 |
| Sr/Ba | 0.68 | 0.32 | 0.49 | 0.34 | 0.48 | 0.34 | 0.29 | 0.37 | 0.21 | 0.19 | 0.21 | 0.23 | 0.21 | 0.30 | 0.37 | 0.36 |
| Rb/Ba | 0.74 | 0.19 | 0.27 | 0.23 | 0.32 | 0.27 | 0.27 | 0.38 | 0.36 | 0.52 | 0.15 | 0.96 | 0.46 | 0.60 | 0.64 | 0.79 |
| Ni | 11 | 20 | 18 | 15 | 7 | 8 | <4 | <4 | <4 | <4 | <4 | <4 | <4 | <4 | 10 | <4 |
| V | 159 | 186 | 166 | 98 | 137 | 11 | 75 | 59 | <5 | <5 | 14 | 12 | <5 | <5 | 5 | <5 |
| Cr | 23 | 150 | 66 | 16 | 62 | 50 | 57 | 30 | 30 | 12 | 20 | 33 | 15 | 16 | | |
| Zn | 151 | 71 | 73 | 71 | 66 | 50 | 52 | 51 | 35 | 31 | 35 | 36 | 23 | 27 | 14 | |
| Ga | 32 | 18 | 21 | 19 | 19 | 20 | 18 | 17 | 14 | 15 | 16 | 23 | 15 | 16 | 14 | 14 |
| Pb | 20 | 11 | 13 | 24 | 16 | 26 | 25 | 28 | 45 | 41 | 48 | 27 | 31 | 31 | 41 | 34 |
| Y | 45 | 24 | 24 | 27 | 7 | 19 | 20 | 18 | 21 | 19 | 14 | 13 | 12 | 12 | 10 | 11 |
| La | 9.2 | 14.8 | 24.6 | 27.4 | 30.9 | | 22.6 | | 10.5 | 7.8 | 25.8 | 8.7 | 8.8 | | 6.8 | 6.7 |
| Ce | 21.3 | 30.0 | 59.6 | 55.0 | 59.9 | | 42.8 | | 23.8 | 15.5 | 46.8 | 21.4 | 16.9 | | 13.3 | 16.3 |
| Pr | | | 7.4 | 6.6 | | | | | 2.6 | 1.7 | 5.8 | 2.5 | | | 1.6 | 1.7 |
| Nd | 13.6 | 17.7 | 31.0 | 26.4 | 24.2 | | 20.1 | | 10.3 | 7.1 | 21.8 | 10.8 | 7.0 | | 7.1 | 7.3 |
| Sm | 5.4 | 4.4 | 5.4 | 5.2 | 3.7 | | 4.3 | | 2.7 | 1.9 | 4.4 | 2.1 | 1.5 | | 1.5 | 1.8 |
| Eu | 0.9 | 1.3 | 1.1 | 1.1 | 1.2 | | 1.0 | | 0.8 | 0.5 | 0.9 | 0.1 | 0.4 | | 0.5 | 0.2 |
| Gd | 6.7 | 4.1 | 6.0 | 4.3 | 2.3 | | 3.6 | | 3.9 | 2.2 | 3.4 | 2.9 | 1.3 | | 1.5 | 2.4 |
| Tb | | | 0.74 | 0.56 | | | | | 0.65 | 0.44 | 0.52 | 0.44 | | | | 0.31 |
| Dy | 7.1 | 3.7 | 4.4 | 3.3 | 1.3 | | 3.2 | | 3.8 | 2.2 | 2.6 | 2.5 | 1.4 | | 1.7 | 1.8 |
| Ho | | | 0.87 | 0.72 | | | | | 0.70 | 0.52 | 0.53 | | | | 0.37 | 0.34 |
| Er | | | 2.2 | 1.9 | | | | | 1.64 | 1.22 | 1.20 | 1.25 | | | 1.06 | 1.03 |
| Tm | | | 0.25 | 0.23 | | | | | 0.23 | 0.17 | 0.18 | 0.20 | | | 0.16 | |
| Yb | 2.2 | 2.0 | 1.7 | 1.4 | 0.76 | | 1.5 | | 1.3 | 1.0 | 1.1 | 1.2 | 0.88 | | 1.2 | 1.0 |
| Lu | 0.24 | 0.26 | 0.22 | 0.18 | 0.11 | | 0.20 | | 0.13 | 0.13 | 0.17 | 0.16 | 0.12 | | 0.21 | 0.15 |
| La/Yb n | 3 | 5 | 9 | 11 | 26 | | 10 | | 5 | 5 | 15 | 4 | 6 | | 4 | 4 |
| Y/Ho | | | 28 | 38 | | | | | 30 | 37 | 27 | | | | 27 | 32 |
| Eu/Eu* | 0.48 | 0.92 | 0.6 | 0.7 | 1.2 | | 0.8 | | 0.8 | 0.8 | 0.7 | 0.2 | 0.8 | | 1.0 | 0.3 |
| Ce/Ce* | | | | | | | | | 1.1 | 1.0 | 1.0 | 1.2 | | | 1.0 | 1.2 |
| Pr/Pr* | | | | | | | | | 1.0 | 1.0 | 1.0 | 1.0 | | | 0.9 | 1.0 |
| TE1 | | | | | | | | | 1.1 | 1.0 | 1.0 | 1.1 | | | 1.0 | 1.1 |
| Q | 123 | 162 | 172 | 159 | 178 | 181 | 191 | 184 | 188 | 187 | 183 | 212 | 195 | 202 | 227 | 195 |
| P | −109 | −78 | −108 | −94 | −110 | −82 | −77 | −93 | 3 | −22 | −37 | 4 | −42 | −34 | −32 | −54 |
| A | 87 | 61 | 67 | 45 | 62 | 91 | 76 | 57 | 57 | 57 | 47 | 91 | 45 | 60 | 46 | 40 |
| B | 137 | 172 | 116 | 124 | 105 | 109 | 76 | 68 | 24 | 16 | 37 | 38 | 14 | 19 | 10 | 11 |
| F | 294 | 221 | 267 | 272 | 272 | 265 | 288 | 303 | 343 | 352 | 335 | 305 | 346 | 334 | 318 | 349 |
| B* | 24.8 | 30.9 | 20.9 | 22.4 | 18.9 | 19.7 | 13.7 | 12.3 | 4.4 | 2.9 | 6.7 | 6.9 | 2.5 | 3.5 | 1.8 | 2.0 |
| A/CNK | 1.31 | 1.21 | 1.23 | 1.16 | 1.22 | 1.38 | 1.31 | 1.23 | 1.24 | 1.24 | 1.19 | 1.43 | 1.19 | 1.27 | 1.22 | 1.17 |
| NK/A | 0.48 | 0.35 | 0.38 | 0.47 | 0.40 | 0.50 | 0.54 | 0.60 | 0.75 | 0.77 | 0.69 | 0.63 | 0.78 | 0.74 | 0.74 | 0.78 |
| MALI | 3.6 | 0.1 | 0.8 | 2.1 | 1.1 | 4.1 | 4.4 | 4.9 | 8.2 | 8.4 | 6.8 | 6.9 | 7.8 | 7.7 | 6.7 | 7.6 |
| Fe* | 0.77 | 0.62 | 0.70 | 0.67 | 0.75 | 0.66 | 0.75 | 0.69 | 0.64 | 0.68 | 0.80 | 0.74 | 0.85 | 0.73 | 0.99 | 0.96 |
| T sat zr | 767 | 753 | 785 | 773 | 779 | 781 | 765 | 749 | 705 | 692 | 756 | 710 | 691 | 698 | 701 | 679 |
| T sat ap | 1088 | 916 | 967 | 895 | 972 | 1017 | 1023 | 1018 | 1050 | 1064 | 969 | 1015 | 1073 | 1043 | 1015 | 1023 |

Major elements (wt.%); trace elements (ppm).
Q, P, A, B, F and the proportion of dark minerals in wt.% $B^* = 100^*B/(Q+F+B)$ from Debon and Le Fort (1988).
$A/CNK = Al_2O_3/(CaO + Na_2O + K_2O)$ (wt.%); $MALI = Na_2O + K_2O - CaO$ (wt.%); $Fe^* = FeOt/(FeOt + MgO)$ (wt.%); mg# = MgO/(MGO + FeO) (mol%).
T sat zr and T sat ap are the zircon and apatite saturation temperatures, after Harrison and Watson (1984) and Watson and Harrison (1983), respectively.
$Ce/Ce^* = Ce_N/(La_N^{0,66*}Nd_N^{0,33})$; $Pr/Pr^* = Pr_N/(La_N^{0,33*}Nd_N^{0,66})$; $TE1 = (Ce/Ce^* \times Pr/Pr^*)^{0.5}$.

at *c.* 74% $SiO_2$ where all granites and foliated dykes are grouped close to an eutectic composition ($Q_{33}Or_{31}Ab_{35}An_{01}$). These linear arrays are well defined for Ti, Fe, Al, Mg, Sr, and Ce, and somewhat less distinct for Ca, Na, and Rb, probably due to the mobility of these elements in alteration processes (saussuritization, retrometamorphism, interaction between magmas, etc.). Th and Ba show more complex evolutions that can be divided into a linear trend from MME #10MB to 74% $SiO_2$ followed by an abrupt decrease in the granitic rocks and foliated dykes to 76% $SiO_2$. $K_2O$ shows also a decrease for rocks >74% as well as, although more markedly, Zr. This suggests the late crystallization of K-feldspar and zircon. The REE distribution in the Moulin Blanc granites (Fig. 8) resembles those in the foliated dykes (similar $[La/Yb]_N$ ratios, similar range of concentrations), except for sample #91M4 (Bonne Terrasse dyke) which is richer in LREE and has a higher $[La/Yb]_N$ ratio. However, in most foliated dykes, spidergrams indicate (Fig. 8) that the most incompatible elements are depleted and Eu anomalies are more variable, pointing to a more fractionated character for these dykes. In contrast, sample #91M4 is much higher in Th, Zr, Hf and Ti than the other foliated dykes (Fig. 8).

*5.1.2. The Camarat granite and dykes, and the Pinet and Capon granites*

The compositions of these various granitic rocks are reported in Table 2 together with the values of several parameters. According to Debon and Le Fort (1988), all granites are peraluminous leucogranites. Following the classification parameters of Frost et al. (2001), the MALI index straddles the limit between calc-alkalic and alkali-calcic types and the Fe* index oscillates between ferroan and magnesian types. The A/CNK index varies between 1.02 and 1.40; it is higher than 1.1 in the Camarat, Pinet and Capon granites, which are thus strongly peraluminous (Sylvester, 1989). The CaO content is relatively low and haplogranitic compositions are approached. In the Capon granite, the amount of $P_2O_5$ is higher than the appropriate amount of Ca necessary to form apatite, thus some P is incorporated in alkali feldspar (Bea et al., 1992). The Camarat dykes' REE patterns are distinctly different from the Camarat granite (Fig. 9a and b) with much lower $[La/Yb]_N$ ratios (1–2 vs 5–12 in the granites) and larger negative Eu anomalies. The Pinet granite has $[La/Yb]_N$ and Eu/Eu* values close to the Camarat granite but lower REE concentrations (Fig. 9c). The Capon granite and the cross-cutting leucogranitic dykes have the lowest REE contents, low $[La/Yb]_N$ and Eu/Eu* ratios down to 0.07 (Fig. 9c and d). A lanthanide tetrad effect following Irber (1999), with values of TE1 ($= (Ce/Ce^* \times Pr/Pr^*)^{0.5}$) ≥1.2 is characteristic of the Camarat dykes (Table 2). In spidergrams normalized to MORB (Fig. 10), further differences appear between the Camarat, Pinet and Capon granites: the Camarat granite is particularly rich in Th, Nb, Zr and REE; the Capon granite is very poor in Ba, REE and Zr and very rich in Nb; the Pinet granite is intermediate between the Camarat and Capon granites and resembles the Moulin Blanc granite and dykes.

Sample #91M12B coming from the elongated pillow inside the dolerite of the Capon composite dyke (Fig. 5) is a magnesian calc-alkaline peraluminous leucotonalite.

*5.1.3. Dolerite dykes*

Chemical analyses of dolerites are reported in Table 3. A series of samples has been collected in a dyke south of the Camarat cape (Fig. 2)

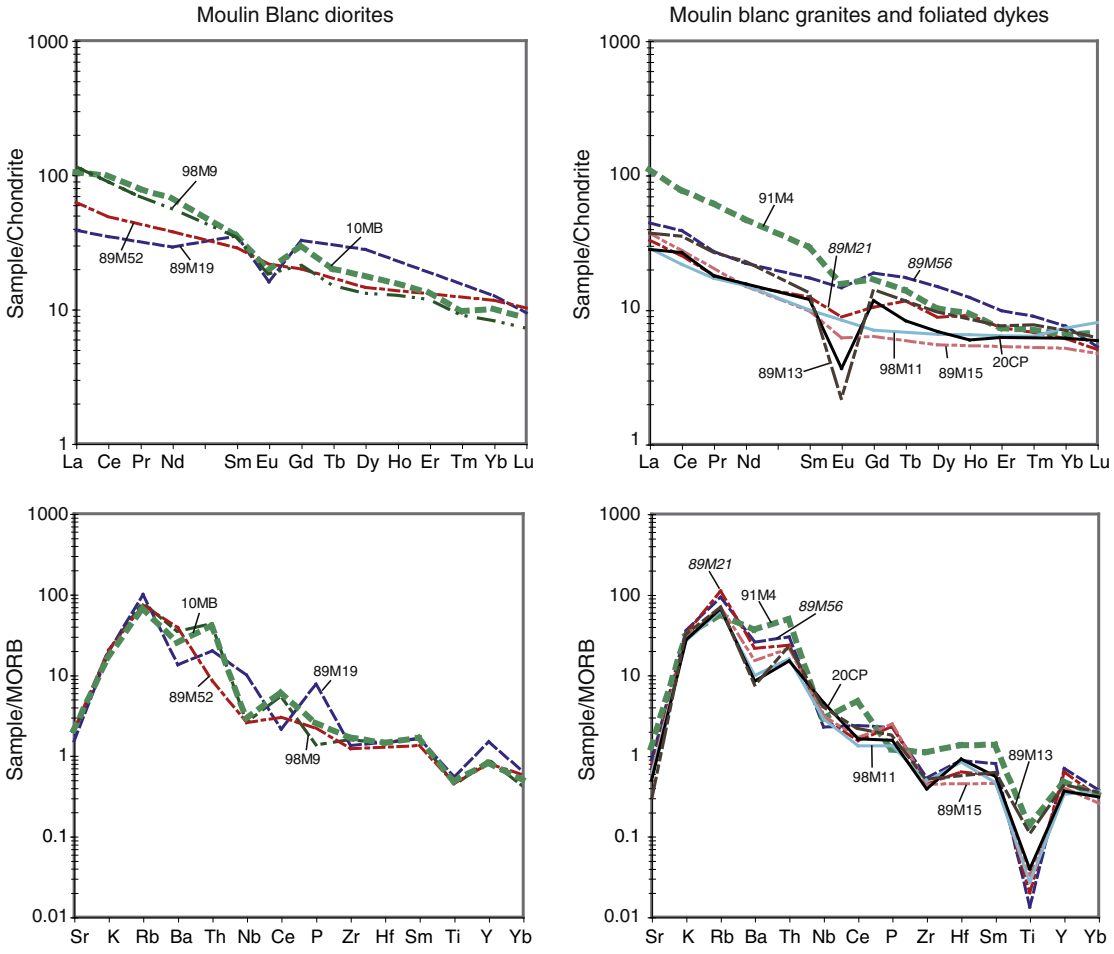


**Fig. 8.** REE chondrite normalized values and spidergram normalized to MORB composition of Pearce (1983) in the Moulin Blanc diorites (left column) and in the Moulin Blanc granites #89M56 and #89M21 (rock numbers in italics) and foliated granitic dykes (right column). Data in Table 1.

named Camarat 1 in Table 3. The composition of these samples display a relatively large variation in $SiO_2$ (50.1–54.7%), CaO (2.7 to 6.8%), $K_2O$ (1.6 to 3.0%) and $Na_2O$ (2.8 to 4.4%), compared to the other elements $TiO_2$, $Al_2O_3$, $Fe_2O_3$t and MgO. They are grossly comparable to the Pinet dolerite, but are lower in $SiO_2$ and $K_2O$ than the Capon dolerite (#91M7). Another dolerite dyke, named Camarat 2, north of the Camarat tip (Fig. 2; sample #98M5), has a somewhat different major element composition than Camarat 1, particularly with lower $SiO_2$ and higher $Fe_2O_3$, MgO, $TiO_2$ and $P_2O_5$. Moreover it is very low in CaO (1.63%). Another peculiar sample (#92M13) has been taken in the Capon composite dyke just at the contact of the dolerite with the granite component of the dyke (Fig. 5): its major element composition is close to the Capon dolerite #91M7 except for a very low CaO content (0.76%) and a higher $Na_2O$ content.

The average REE content in Camarat 1 and Pinet and in Capon #91M7 dolerites show very similar patterns (Fig. 11) with low $[La/Yb]_N = 4.0–7.0$ ratios and a Eu/Eu* ratio close to unity in the Camarat and Pinet samples and a slightly negative anomaly in the Capon samples. Camarat 2 has the same REE distribution but with higher values, and sample #92M13 is lower in REE and more irregular.

In spidergrams (Fig. 11) all dolerites show profiles similar to high-K calc-alkaline basalts, with high LILE, Nb–Ta negative anomalies and moderate decrease towards less incompatible elements. In the discrimination diagram, $Zr/TiO_2$ vs Nb/Y diagram (Pearce, 1996; Winchester and Floyd, 1977) (Fig. 12a), all dolerite samples plot at the limit between andesite and andesite–basalt. In Th/Yb vs Nb/Yb diagram (Fig. 12b), the samples show high Th/Yb ratios distinctly above the asthenospheric mantle area (Pearce, 1983), typical for calc-alkaline rocks, with the highest ratio for the Capon dolerite and the lowest for Camarat 2 (#98M5) dolerite.

### 5.2. Sr and Nd isotopes

Representative samples of the studied granite plutons and dykes have been analyzed for Sr and Nd isotopes (Table 4). The $\varepsilon_{Nd}$ and $^{87}Sr/^{86}Sr$ ratios recalculated to 300 Ma (granite zircon ages) are presented in Fig. 13a together with the mixing curve between the classical Variscan end-member components inferred from lower crustal granulite xenoliths in the French Massif Central (Downes et al., 1990). Nd model ages following Nelson and DePaolo (1985), considered to be based on the most realistic model for the mantle evolution (Liégeois and Stern, 2010 and references therein) are also presented in Table 4. Both 1-stage and 2-stage model ages are provided. The latter uses a mean crust $^{147}Sm/^{144}Nd$ value (0.12) for the $^{143}Nd/^{144}Nd$ evolution beyond the crystallization age. This is especially needed when magmatic processes have strongly modified the $^{147}Sm/^{144}Nd$ of the source. Moreover, when the $^{147}Sm/^{144}Nd$ of the rock is >0.15, no meaningful 1-stage model ages can be calculated, the sample evolution being not enough oblique to that of the mantle (no value provided in Table 4 in these cases). In the following text, only the $NdT_{DM}$ 2-stage model ages will be used and they will be simply noted for convenience $NdT_{DM}$. $NdT_{DM}$ are plotted against $SiO_2$, taken as the differentiation index, in Fig. 13b.

Most of the samples plot in the vicinity of the mixing hyperbola between the Variscan mantle and lower crust end-members, a large part being located in the vicinity of the old continental crust end-member. $NdT_{DM}$ vs $SiO_2$ diagram (Fig. 13b) displays a positive correlation between model ages and silica for the dolerites and a Moulin Blanc diorite. Model ages of the mafic magmas are significantly older (>400 myr) than their emplacement age, which suggests an AFC process affecting already enriched mafic magmas. Moulin Blanc granite and dykes have $NdT_{DM}$ model ages in the 1.4–1.6 Ga range. The other granitic samples (>70% $SiO_2$) display $NdT_{DM}$ model ages between 1.1 and 1.45 Ga. These $NdT_{DM}$ result most probably from the mixing of Paleoproterozoic/Archean and Neoproterozoic/Paleozoic sources and not from a Mesoproterozoic source. Indeed, European Pre-Variscan terranes formed in the periphery of Northern Gondwana (see below Fig. 19), more precisely close to West Africa (Melleton et al., 2009 and references therein), characterized by the absence of Mesoproterozoic lithologies and events (Ennih and Liégeois, 2008 and references therein). Bimodal Paleoproterozoic and Neoproterozoic inherited zircon populations are present in the French Massif Central in both granites and orthogneisses and in metasedimentary rocks (Melleton et al., 2009). Mesoproterozoic $NdT_{DM}$ model ages of Maures felsic magmas would thus result from the mixing between Carboniferous mantle magmas and a crustal melt deriving from an old basement. The Maures $NdT_{DM}$ model ages imply that the old continental end-member is older than 1.6 Ga, in agreement with the abundant inherited Paleoproterozoic zircons from the Orosirian period (2.05–1.8 Ga; International Commission on Stratigraphy 2010; http://www.stratigraphy.org/column.php?id=Chart/Time Scale) found in magmatic and metasedimentary rocks of the French Massif Central (Melleton et al., 2009).

In more detail, Fig. 13a shows that the Camarat dolerites (andesite basalt) with $\varepsilon_{Nd}$ values close to zero or positive ($NdT_{DM}$: 0.7–0.9 Ga), show relatively large amounts of crustal contamination (close to 20–30% in the model using values of Downes et al. (1990)); the Capon dolerite is more contaminated than the Camarat dolerite and can result from the contamination of the latter by 40% of crustal end-member. The Camarat dykes have a larger crustal component than the main pluton to which they are related. Finally, the Pinet granite and dolerite show an altered Sr isotope signature.

## 6. Discussion

### 6.1. Granites: processes, sources and dyke emplacement

#### 6.1.1. The Moulin Blanc granite: evidence of mixing process and emplacement mechanism

What is the meaning of the linear arrays which appear on Harker diagrams for immobile elements (Fig. 7) and what are the possible relationships of the diorite samples with these linear trends?

We have used the PELE algorithm (Boudreau, 1999) to simulate the possible evolution by fractional crystallization of the three dioritic melt compositions. At 2–3 kbar and $fO_2$ at the FMQ buffer, the 3 melts start crystallizing a low-Ca pyroxene ($En_{73–82}$), the subtraction of which leads to a rapid decrease in MgO content which falls below the observed trend. It is thus not possible that these compositions could be parental to the observed linear trends. Since fractional crystallization is precluded, we suggest that the linear trends, particularly well defined for the less mobile elements (Fig. 7), indicate a mixing process between the MME diorite (#10MB and #98M9) and a granite at 74% $SiO_2$, the two magmas having distinct isotopic signatures (Fig. 13). We thus conclude that the intermediate compositions of the Moulin Blanc series are hybrid magmas, a conclusion also supported by the rock microstructure that suggests a phenocryst–matrix mixture.

A second process, however, is required to explain the evolution of some elements in the most silicic rocks, i.e. the granite and the associated foliated dykes, particularly the decrease in Ba, Th and Zr (Fig. 7). We have calculated with currently accepted partition coefficients (e.g. Martin, 1987) a Rayleigh fractional crystallization model which shows that crystallization of an eutectic assemblage with trace amounts of monazite (0.015%), zircon (0.1%), apatite (2%) and garnet (2%) can explain the observed evolution. This geochemical kindred between granite and dykes, together with their similar isotopic signatures (Fig. 13) and overall trace element distributions (Fig. 10), convincingly corroborate their mineralogical similitude (namely the occurrence of cordierite) and their common foliated character. Sample #91M4 from the Bonne Terrasse foliated dyke with its high LREE, Th, Zr, Hf and Ti contents, and low Rb/Sr and Rb/Ba ratios (see below) seems, however, related to an unknown granite, other than the Moulin Blanc granite.

**Table 2**
Major and trace element composition of samples of the Camarat granites and dykes, the granitic component of composite dykes, and of cross-cutting leucogranitic dykes.

| | Camarat pluton | | | | | | | | | | | |
|---|---|---|---|---|---|---|---|---|---|---|---|---|
| | Granite | | | | Dyke | | | | | | | |
| | 89M25 | 89M22 | 89M27 | 89M30 | 98M6 | 98M15 | 98M16 | 26-C | 89M31 | 89M33 | 32-C | 98M2 |
| $SiO_2$ | 73.38 | 77.00 | 75.09 | 75.07 | 78.01 | 76.96 | 77.64 | 76.92 | 78.30 | 76.23 | 76.53 | 77.37 |
| $TiO_2$ | 0.19 | 0.14 | 0.18 | 0.17 | 0.06 | 0.04 | 0.03 | 0.03 | 0.06 | 0.10 | 0.02 | 0.03 |
| $Al_2O_3$ | 14.27 | 13.02 | 13.69 | 13.12 | 12.24 | 13.33 | 13.16 | 12.84 | 11.82 | 13.58 | 13.29 | 13.12 |
| $Fe_2O_3t$ | 2.18 | 0.82 | 1.99 | 1.78 | 0.73 | 0.31 | 0.54 | 0.49 | 0.97 | 0.92 | 0.61 | 0.74 |
| MnO | 0.08 | 0.05 | 0.09 | 0.09 | 0.01 | 0.01 | 0.02 | 0.02 | 0.05 | 0.05 | 0.03 | 0.02 |
| MgO | 0.39 | 0.18 | 0.49 | 0.66 | 0.23 | 0.02 | 0.01 | 0.15 | 0.28 | 0.30 | 0.07 | 0.06 |
| CaO | 0.63 | 0.50 | 0.68 | 0.53 | 0.08 | 0.27 | 0.31 | 0.54 | 0.27 | 0.63 | 0.18 | 0.21 |
| $Na_2O$ | 3.69 | 3.00 | 3.29 | 3.37 | 3.28 | 4.34 | 4.01 | 3.57 | 3.81 | 3.93 | 4.35 | 3.95 |
| $K_2O$ | 4.94 | 4.95 | 4.81 | 5.02 | 5.31 | 4.94 | 5.15 | 4.99 | 4.32 | 4.68 | 5.18 | 4.71 |
| $P_2O_5$ | 0.25 | 0.22 | 0.20 | 0.19 | 0.02 | 0.03 | 0.09 | 0.26 | 0.12 | 0.24 | 0.10 | 0.01 |
| Total | 100.02 | 99.88 | 100.50 | 99.99 | 100.00 | 100.26 | 100.97 | 99.80 | 100.00 | 100.67 | 100.35 | 100.22 |
| LOI | 0.59 | 0.76 | 0.77 | 0.90 | | 0.70 | 0.68 | | 2.90 | 0.60 | | 1.04 |
| U | 9.0 | 16 | 14 | 15 | 8.0 | 8.4 | 7.4 | 8.0 | 16 | 21 | 23 | 7.0 |
| Th | 18 | 26 | 22 | 31 | 12 | 13 | 12 | 8.0 | 28 | 31 | 14 | 15 |
| Zr | 115 | 100 | 116 | 117 | 53 | 46 | 50 | 33 | 56 | 86 | 59 | 57 |
| Hf | | | 4.2 | | 2.4 | 2.5 | 2.6 | 1.63 | | 3.7 | 3.9 | 1.8 |
| Nb | 20 | 19 | 19 | 19 | 18 | 12 | 12 | 12 | 14 | | 41 | 23 |
| Ta | | | 3.3 | | 4.0 | 3.7 | 3.0 | 4.25 | | 3.6 | 13 | 4.1 |
| Rb | 369 | 357 | 365 | 375 | 369 | 305 | 300 | 205 | 317 | 317 | 391 | 451 |
| Sr | 81 | 37 | 73 | 59 | 30 | 28 | 31 | 23 | 17 | 41 | 8 | 13 |
| Ba | 346 | 116 | 317 | 221 | | 63 | 92 | 44 | 60 | 180 | 42 | 12 |
| Rb/Sr | 4.6 | 9.6 | 5.0 | 6.4 | 12.3 | 11.1 | 9.7 | 8.91 | 18.6 | 7.7 | 48.9 | 34.7 |
| Sr/Ba | 0.23 | 0.32 | 0.23 | 0.27 | | 0.44 | 0.34 | 0.52 | 0.28 | 0.23 | 0.19 | 1.08 |
| Rb/Ba | 1.07 | 3.08 | 1.15 | 1.70 | | 4.84 | 3.26 | 4.66 | 5.28 | 1.76 | 9.31 | 37.58 |
| V | 23 | 13 | 19 | 19 | 6 | <5 | <5 | 3 | 6 | 11 | | 5 |
| Cr | 29 | 37 | 11 | 6 | | 6 | 5 | 8 | 6 | 4 | 17 | |
| Zn | 40 | 28 | 36 | 41 | 16 | 10 | 6 | 18 | 22 | 21 | 24 | 22 |
| Ga | 20 | 17 | 19 | 18 | 15 | 14 | 15 | 15 | 16 | 17 | 20 | 18 |
| Pb | 29 | 29 | 30 | 29 | 23 | 36 | 43 | 35 | 31 | 39 | 45 | 33 |
| Y | 24 | 47 | 27 | 51 | 40 | 31 | 34 | 33 | 78 | 115 | 53 | 52 |
| La | 24.1 | 27.4 | 22.3 | 27.3 | 8.6 | 9.2 | 8.0 | 9.5 | 19.1 | 19.1 | 6.1 | 10.5 |
| Ce | 52.9 | 63.3 | 53.8 | 64.0 | 21.2 | 18.8 | 21.3 | 25.9 | 46.1 | 56.9 | 19.8 | 25.8 |
| Pr | | | 6.7 | | 2.9 | 2.5 | 2.6 | 2.9 | | 8.0 | 3.1 | 3.2 |
| Nd | 22.9 | 27.6 | 25.6 | 28.8 | 10.8 | 9.3 | 10.1 | 11.5 | 21.1 | 31.4 | 13.2 | 12.4 |
| Sm | 4.9 | 6.1 | 5.0 | 6.8 | 2.7 | 2.8 | 3.1 | 2.5 | 5.7 | 10.5 | 5.4 | 3.2 |
| Eu | 0.6 | 0.2 | 0.6 | 0.4 | 0.2 | 0.3 | 0.3 | 0.3 | 0.1 | 0.3 | 0.1 | 0.1 |
| Gd | 3.8 | 4.2 | 5.5 | 5.5 | 3.6 | 3.1 | 3.3 | 4.6 | 4.4 | 14.3 | 6.9 | 4.1 |
| Tb | | | 0.75 | | 0.79 | 0.76 | 0.85 | 0.61 | | 2.34 | 1.18 | 0.58 |
| Dy | 3.1 | 2.9 | 4.4 | 4.9 | 4.5 | 4.6 | 4.8 | 4.4 | 4.9 | 19.1 | 8.6 | 4.9 |
| Ho | | | 0.93 | | 1.18 | 1.09 | 1.23 | 1.24 | | 4.22 | 1.99 | 1.11 |
| Er | | | 2.5 | | 3.2 | 3.2 | 3.2 | 3.2 | 3.1 | 12 | 5.8 | 3.2 |
| Tm | | | 0.44 | | 0.56 | 0.52 | 0.59 | 0.50 | 0.43 | 2.16 | 1.01 | 0.67 |
| Yb | 1.5 | 1.5 | 2.6 | 2.4 | 3.8 | 4.2 | 4.2 | 3.7 | 4.0 | 14.6 | 7.3 | 3.9 |
| Lu | 0.22 | 0.22 | 0.32 | 0.33 | 0.58 | 0.61 | 0.74 | 0.52 | 0.08 | 1.86 | 0.95 | 0.65 |
| La/Yb n | 10 | 12 | 5 | 7 | 1 | 1 | 1 | 2 | 3 | 1 | 1 | 2 |
| Y/Ho | | | 29 | | 34 | 28 | 28 | 26 | | 27 | 26 | 47 |
| Eu/Eu* | 0.46 | 0.16 | 0.35 | | 0.25 | 0.35 | 0.28 | 0.24 | 0.08 | 0.08 | 0.06 | 0.06 |
| Ce/Ce* | | | 1.2 | | 1.1 | 1.0 | 1.2 | 1.3 | | 1.3 | 1.3 | 1.2 |
| Pr/Pr* | | | 1.1 | | 1.2 | 1.1 | 1.1 | 1.1 | | 1.2 | 1.2 | 1.1 |
| TE1 | | | 1.1 | | 1.2 | 1.0 | 1.2 | 1.2 | | 1.3 | 1.2 | 1.1 |
| Q | 176 | 219 | 200 | 195 | 213 | 179 | 188 | 199 | 217 | 189 | 172 | 199 |
| P | −26 | −1 | −16 | −12 | 5 | −40 | −25 | −19 | −36 | −39 | −34 | −31 |
| A | 33 | 35 | 36 | 23 | 19 | 7 | 8 | 11 | 8 | 18 | 4 | 22 |
| B | 39 | 16 | 39 | 41 | 16 | 5 | 7 | 10 | 20 | 20 | 10 | 11 |
| F | 340 | 319 | 315 | 320 | 326 | 371 | 359 | 346 | 319 | 346 | 373 | 345 |
| B* | 7.1 | 3.0 | 7.1 | 7.3 | 2.8 | 0.9 | 1.3 | 1.8 | 3.6 | 3.6 | 1.7 | 2.0 |
| A/CNK | 1.14 | 1.16 | 1.16 | 1.10 | 1.08 | 1.03 | 1.03 | 1.05 | 1.03 | 1.07 | 1.02 | 1.09 |
| NK/A | 0.80 | 0.79 | 0.77 | 0.84 | 0.91 | 0.94 | 0.92 | 0.88 | 0.93 | 0.85 | 0.96 | 0.88 |
| MALI | 8.0 | 7.4 | 7.4 | 7.9 | 8.5 | 9.0 | 8.8 | 8.0 | 7.9 | 8.0 | 9.3 | 8.4 |
| Fe* | 0.83 | 0.80 | 0.78 | 0.71 | 0.74 | 0.93 | 0.98 | 0.75 | 0.76 | 0.73 | 0.89 | 0.92 |
| T sat zr | 766 | 761 | 771 | 767 | 707 | 690 | 697 | 669 | 707 | 740 | 706 | 712 |
| T sat ap | 1030 | 1046 | 1019 | 1012 | 793 | 854 | 958 | 1091 | 977 | 1051 | 968 | 771 |

Major elements (wt.%); trace elements (ppm).
Q, P, A, B, F and the proportion of dark minerals in wt.% $B^* = 100^*B/(Q+F+B)$ from Debon and Le Fort (1988).
$A/CNK = Al_2O_3/(CaO + Na_2O + K_2O)$ (mol%); $MALI = Na_2O + K_2O - CaO$ (wt.%); $Fe^* = FeOt/(FeOt + MgO)$ (wt.%); $mg\# = MgO/(MGO + FeO)$ (mol%).
T sat zr and T sat ap are the zircon and apatite saturation temperatures, after Harrison and Watson (1984) and Watson and Harrison (1983), respectively.
$Ce/Ce^* = Ce_N/(La_N^{0,66}*Nd_N^{0,33})$; $Pr/Pr^* = Pr_N/(La_N^{0,33}*Nd_N^{0,66})$; $TE1 = (Ce/Ce^* \times Pr/Pr^*)^{0.5}$.

The observation of mingling relationships, particularly of nested enclaves, the occurrence of several mafic magmas of different compositions, the evidence of a mixing process to form the series of rocks, and of fractional crystallization close to the eutectic composition point to a complex scenario for the formation of the Moulin Blanc granite and associated dykes.

| Pinet | | | | Capon | | | | Cross-cutting dykes | | | |
|---|---|---|---|---|---|---|---|---|---|---|---|
| Granite mingled with dolerite | | | | Granitoids mingled with dolerite | | | | | | | |
| 91M2 | 98M13 | 89M44 | 89M49 | 91M6 | 92M14 | 98M8 | 91M12B | 98M14 | 89M46 | 89M10 | 22CP |
| 76.19 | 74.61 | 75.75 | 75.24 | 76.62 | 75.56 | 74.56 | 73.05 | 73.44 | 75.17 | 75.81 | 76.22 |
| 0.04 | 0.07 | 0.07 | 0.05 | 0.02 | 0.02 | 0.02 | 0.16 | 0.01 | 0.03 | 0.03 | 0.02 |
| 14.19 | 14.05 | 14.36 | 14.15 | 15.40 | 14.99 | 15.08 | 14.99 | 15.12 | 14.12 | 15.07 | 14.54 |
| 0.98 | 1.05 | 0.99 | 0.64 | 0.66 | 0.77 | 0.86 | 2.43 | 0.88 | 0.69 | 0.37 | 0.69 |
| 0.02 | 0.05 | 0.03 | 0.05 | 0.07 | 0.09 | 0.07 | 0.04 | 0.19 | 0.09 | 0.12 | 0.08 |
| 0.09 | 0.25 | 0.36 | 0.01 | 0.06 | 0.13 | 0.01 | 0.98 | 0.06 | 0.38 | 0.35 | 0.00 |
| 0.36 | 0.74 | 0.56 | 0.52 | 0.39 | 0.47 | 0.45 | 0.81 | 0.27 | 0.37 | 0.17 | 0.35 |
| 3.78 | 3.86 | 2.65 | 4.17 | 4.69 | 5.54 | 4.72 | 6.72 | 4.01 | 5.44 | 3.69 | 4.35 |
| 4.76 | 4.71 | 4.92 | 4.75 | 2.38 | 2.46 | 3.58 | 0.68 | 5.18 | 3.79 | 4.54 | 3.89 |
| 0.10 | 0.12 | 0.44 | 0.27 | 0.37 | 0.37 | 0.39 | 0.29 | 0.18 | 0.28 | 0.30 | 0.17 |
| 100.50 | 99.51 | 100.14 | 99.86 | 100.66 | 100.40 | 99.75 | 100.15 | 99.35 | 100.35 | 100.45 | 100.30 |
| 1.06 | 1.00 | 1.07 | 0.69 | 1.49 | 1.27 | 0.87 | 1.54 | 0.79 | 0.80 | 0.59 | |
| 6.6 | 4.0 | 8.2 | 4.9 | 8.0 | 8.0 | 16 | 5.7 | 4.2 | 5.8 | 6.8 | 5.5 |
| 7.7 | 4.0 | 7.0 | 6.5 | 2.3 | 2.0 | 3.0 | 2.9 | 4.5 | 2.8 | 6.4 | 2.9 |
| 65 | 47 | 67 | 39 | 30 | 34 | 32 | 50 | 26 | 29 | 32 | 24 |
| | 1.5 | | | 1.5 | 2.2 | 1.8 | 3.1 | 2.0 | | | 1.9 |
| 11 | 10 | 12 | 10 | 23 | 21 | 21 | 27 | 35 | 12 | 14 | 16 |
| | 2.1 | | | 6.2 | 6.1 | 5.8 | 10 | 13 | | | 3.2 |
| 216 | 198 | 195 | 129 | 177 | 216 | 365 | 33 | 346 | 210 | 160 | 240 |
| 57 | 65 | 39 | 73 | 15 | 20 | 28 | 72 | 18 | 15.7 | 13 | 11 |
| 355 | 256 | 246 | 291 | 64 | 75 | 115 | 134 | 46 | 38 | 54 | 43 |
| 3.8 | 3.0 | 5.0 | 1.8 | 11.7 | 10.8 | 13.2 | 0.46 | 19.2 | 13.4 | 12.3 | 21.8 |
| 0.16 | 0.25 | 0.16 | 0.25 | 0.24 | 0.27 | 0.24 | 0.54 | 0.39 | 0.41 | 0.24 | 0.26 |
| 0.61 | 0.77 | 0.79 | 0.44 | 2.77 | 2.88 | 3.17 | 0.25 | 7.52 | 5.53 | 2.96 | 5.58 |
| <6 | 8 | <5 | <5 | <5 | 6 | 7 | 19 | <5 | <5 | <5 | <5 |
| 17 | 0 | 10 | 15 | 16 | 0 | 0 | ? | 5 | 10 | 30 | 0 |
| 30 | 33 | 32 | 20 | 37 | 43 | 25 | 45 | 12 | 24 | 10 | |
| 15 | 16 | 21 | 17 | 25 | 24 | 24 | 19 | 24 | 19 | 19 | 15 |
| 40 | 35 | 20 | 33 | 155 | 22 | 13 | 26 | 28 | 28 | 29 | 20 |
| 18 | 16 | 15 | 13 | 6 | 8 | 9 | 10 | 7 | 11 | 13 | 11 |
| 10.0 | 7.1 | 11.1 | 7.4 | 3.2 | 2.7 | 2.9 | 6.3 | 3.3 | | 3.7 | 3.9 |
| 23.2 | 15.4 | 22.0 | 15.1 | 9.5 | 7.8 | 6.3 | 14.4 | 6.2 | 6.7 | 7.6 | 9.9 |
| | 1.7 | | | 0.9 | 0.8 | 0.7 | 1.8 | 0.8 | | | 1.0 |
| 8.9 | 6.5 | 10.5 | 6.6 | 3.9 | 4.2 | 3.2 | 8.2 | 4.0 | 2.0 | 2.7 | 5.2 |
| 1.6 | 1.4 | 2.3 | 1.4 | 1.1 | 1.1 | 1.3 | 2.1 | 1.1 | 0.7 | 1.0 | 1.3 |
| 0.3 | 0.3 | 0.3 | 0.3 | 0.2 | 0.4 | 0.2 | 0.4 | 0.1 | 0.0 | 0.0 | 0.1 |
| 1.6 | 1.6 | 2.0 | 1.1 | 1.6 | | 1.3 | | 1.4 | 0.7 | 0.9 | 2.1 |
| | | | | | | | | 0.22 | | | 0.29 |
| 1.9 | 1.9 | 1.9 | 1.3 | 1.3 | 1.3 | 1.4 | 1.7 | 1.3 | 1.0 | 1.4 | 2.0 |
| | | | | | | | | 0.29 | | | 0.44 |
| | 1.2 | | | 0.66 | 0.75 | 0.76 | 0.97 | 0.75 | | | 0.88 |
| | | | | 0.09 | | | 0.15 | 0.08 | | | 0.19 |
| 1.2 | 1.2 | 0.82 | 0.90 | 0.60 | 0.84 | 0.88 | 0.94 | 0.70 | 0.82 | 1.2 | 1.2 |
| 0.17 | 0.16 | 0.12 | 0.13 | 0.08 | 0.10 | 0.12 | 0.12 | 0.08 | 0.11 | 0.17 | 0.15 |
| 5 | 4 | 9 | 5 | 3 | 2 | 2 | 4 | 3 | | 2 | 2 |
| | | | | | | | | 24 | | | 25 |
| 0.58 | 0.62 | 0.36 | 0.65 | 0.48 | | 0.44 | | 0.35 | 0.13 | 0.07 | 0.20 |
| | 1.1 | | | 1.4 | 1.2 | 1.0 | 1.1 | 0.9 | | | 1.2 |
| | 1.0 | | | 0.9 | 0.9 | 0.9 | 1.0 | 0.8 | | | 0.8 |
| | 1.1 | | | 1.1 | 1.1 | 1.0 | 1.0 | 0.8 | | | 1.0 |
| 195 | 181 | 224 | 176 | 219 | 183 | 180 | 164 | 165 | 157 | 203 | 196 |
| −27 | −38 | 9 | −43 | −108 | −135 | −84 | −217 | −24 | −102 | −26 | −64 |
| 42 | 25 | 72 | 23 | 86 | 46 | 51 | 34 | 47 | 8 | 74 | 50 |
| 15 | 20 | 22 | 9 | 10 | 13 | 11 | 57 | 13 | 18 | 14 | 9 |
| 345 | 354 | 309 | 370 | 326 | 359 | 364 | 334 | 378 | 380 | 338 | 350 |
| 2.7 | 3.7 | 4.0 | 1.6 | 1.8 | 2.4 | 2.0 | 10.2 | 2.3 | 3.3 | 2.5 | 1.6 |
| 1.18 | 1.10 | 1.34 | 1.09 | 1.40 | 1.19 | 1.21 | 1.13 | 1.19 | 1.03 | 1.33 | 1.21 |
| 0.80 | 0.81 | 0.67 | 0.85 | 0.67 | 0.79 | 0.77 | 0.79 | 0.81 | 0.92 | 0.73 | 0.78 |
| 8.2 | 7.8 | 7.0 | 8.4 | 6.7 | 7.5 | 7.8 | 6.6 | 8.9 | 8.9 | 8.1 | 7.9 |
| 0.91 | 0.79 | 0.71 | 0.98 | 0.91 | 0.84 | 0.99 | 0.69 | 0.93 | 0.62 | 0.49 | 1.00 |
| 726 | 695 | 739 | 681 | 681 | 677 | 674 | 698 | 658 | 655 | 682 | 656 |
| 960 | 966 | 1125 | 1060 | 1109 | 1102 | 1100 | 1049 | 998 | 1063 | 1077 | 1015 |

Mixing between magmas needs time and stirring, and this suggests the existence of a magma chamber at greater depths than the final depth of emplacement, in which convection could facilitate the hybridization process. Several influxes of dioritic magmas in this chamber can provide the mafic components of the mixture, can reheat the resident magma, and can develop a compositional zoning

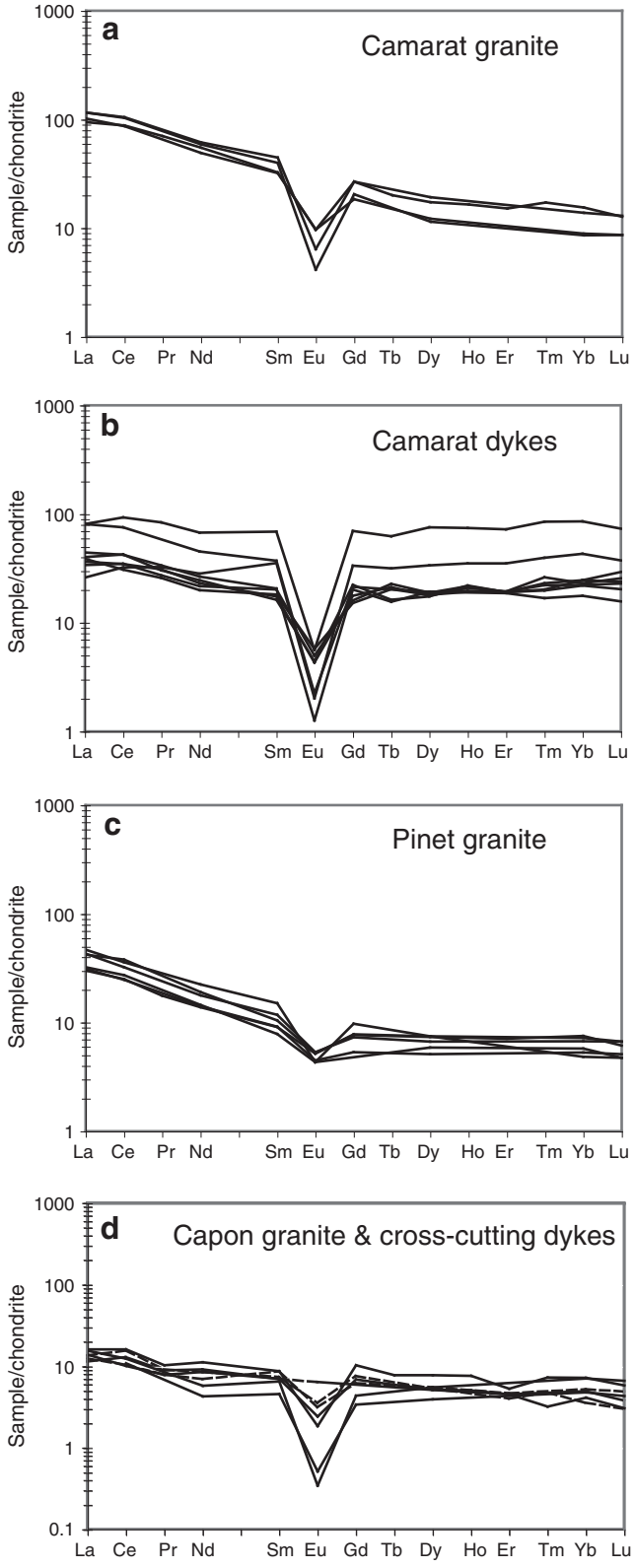


**Fig. 9.** REE distribution normalized to Sun and McDonough (1989) in: a. Camarat granite (line); b. Camarat granitic veins and dykes; c. Pinet granite; d: Capon granite (dashed) and cross-cutting leucogranitic dykes (line). Data in Table 2.

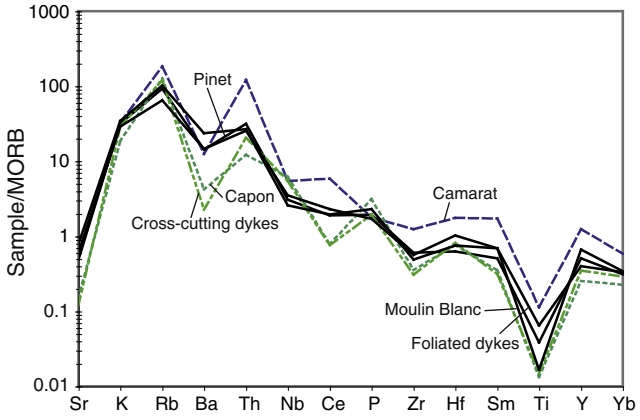


**Fig. 10.** The MORB normalized trace element distribution in average samples of Camarat granite, Pinet and Capon granites, cross-cutting leucogranitic dykes, Moulin Blanc granites (>74% $SiO_2$), and foliated granitic dykes. Normalizing values from Pearce (1983). Note the similar distributions in Pinet and Moulin Blanc granites and foliated leucogranitic dykes. Data in Tables 1 and 2.

in the chamber. Deformation of this magma chamber accompanied by new dioritic influxes can inject various batches in the final magma chamber, where rapidly chilled dioritic pillows could form. The deformation has also favored injection of magma in a dyke system, as discussed below. Some fractionation in the granite could take place during each step of the intrusive process. Finally, the occurrence of a massive diorite attests that the formation and intrusion of dioritic magma were late in the transpressional deformation or could even last longer than this tectonic event. The Moulin Blanc intrusion thus appears as a clear illustration of the formation of an igneous body constructed gradually by discontinuous magma inputs (Clemens et al., 2010b; Glazner et al., 2004; Vigneresse, 2007).

*6.1.2. CHARAC behavior in the Camarat dykes*

Bau (1996) has suggested that in evolved granites Zr/Hf, Y/Ho and the lanthanide tetrad effect could indicate non-CHARAC (non Charge and Radius Controlled) trace element behavior. The anomalous behavior of these high field strength elements results from the fact that the magmatic system is transitional between pure silicate melt and hydrothermal fluids, the latter favoring non-CHARAC behavior especially when F and Cl-rich. Fig. 14a shows that most Camarat dyke samples have anomalously low Zr/Hf ratio together with significant tetrad effect ($TE1 = (Ce/Ce^* \times Pr/Pr^*)^{0.5} \geq 1.10$).

Modeling of the relationship between the Camarat granite and the associated dykes in terms of fractional crystallization and mineral/melt partition coefficients does not lead to convincing results. We have followed the approach of Cocherie et al. (1994) who successfully showed that the sea-gull REE patterns can be obtained by crystallization of minute amounts of LREE enriched accessory phases (allanite, monazite, etc.). In the Camarat case, it is indeed possible to explain at eutectic conditions the enrichment in HREE and the decrease in La/Yb ratio by crystallizing 0.04% monazite or 0.4% allanite (using the $K_D$ values of e.g. Martin (1987)), but this does not account for the strong increase in the negative Eu anomaly (down to $Eu/Eu^* = 0.06$). Though not so well constrained, the non-CHARAC behavior seems a more convincing process to relate the Camarat dykes to the main granite.

It should be mentioned that the Y/Ho in the considered granites (except sample #98M2) remains within the accepted values for the CHARAC behavior (Bau, 1996) even for high tetrad values (Fig. 14b). This ratio does not appear to be systematically affected by hydrothermal alteration as already noted in the Woduhe and Baerze granites in China (Jahn et al., 2001).

Linnen and Keppler (2002) have shown experimentally that in peraluminous melts the solubility of $HfSiO_4$ is larger than that of $ZrSiO_4$, thus a strong decrease of Zr/Hf is expected to occur with fractional crystallization. In the Capon granite and in the cross-cutting leucogranitic dykes, most TE1 values being <1, the low Zr/Hf values can be explained by this process. A similar interpretation can also explain the low Nb/Ta (3 to 6) compared to the chondritic value of 17.5 (Linnen and Keppler, 1997).

**Table 3**
Major and trace element composition of selected samples of doleritic rocks.

| | Camarat | | | | | | | | Pinet | | Capon | |
|---|---|---|---|---|---|---|---|---|---|---|---|---|
| | Cam 1 | | | | | | | Cam 2 | | | | Contact |
| | 91M19 | 91M18 | 89M38 | 91M17 | 89M39 | 98M1 | 98M3 | 98M5 | 91M3 | 89M41 | 91M7 | 92M13 |
| $SiO_2$ | 50.10 | 50.68 | 51.30 | 51.53 | 52.25 | 52.35 | 54.65 | 48.10 | 51.39 | 53.27 | 55.13 | 56.30 |
| $TiO_2$ | 1.60 | 1.67 | 1.70 | 1.54 | 1.69 | 1.60 | 1.76 | 2.47 | 1.42 | 1.45 | 0.88 | 0.96 |
| $Al_2O_3$ | 16.22 | 16.01 | 16.84 | 16.44 | 16.27 | 16.71 | 15.20 | 15.00 | 16.05 | 16.32 | 17.08 | 17.72 |
| $Fe_2O_3t$ | 9.44 | 9.53 | 9.34 | 9.51 | 9.48 | 8.85 | 8.89 | 13.14 | 9.12 | 8.77 | 7.86 | 8.63 |
| MnO | 0.20 | 0.17 | 0.20 | 0.16 | 0.28 | 0.13 | 0.17 | 0.20 | 0.16 | 0.15 | 0.20 | 0.09 |
| MgO | 6.35 | 5.31 | 5.34 | 5.91 | 5.49 | 6.39 | 4.97 | 8.81 | 6.59 | 6.81 | 5.80 | 4.13 |
| CaO | 6.69 | 6.79 | 6.36 | 4.64 | 4.15 | 2.72 | 3.57 | 1.63 | 5.48 | 3.92 | 5.32 | 0.76 |
| $Na_2O$ | 2.83 | 3.06 | 3.31 | 3.82 | 2.96 | 3.95 | 4.44 | 2.60 | 3.24 | 2.72 | 1.12 | 2.72 |
| $K_2O$ | 1.58 | 1.80 | 1.68 | 1.60 | 2.98 | 2.35 | 1.88 | 1.57 | 1.76 | 2.26 | 2.71 | 2.91 |
| $P_2O_5$ | 0.35 | 0.43 | 0.44 | 0.34 | 0.58 | 0.37 | 0.63 | 1.11 | 0.31 | 0.39 | 0.22 | 0.24 |
| LOI | 3.74 | 3.70 | 3.10 | 3.81 | 3.10 | 3.87 | 3.11 | 4.59 | 3.48 | 3.47 | 2.73 | 5.37 |
| Total | 99.10 | 99.15 | 99.61 | 99.30 | 99.24 | 99.30 | 99.27 | 99.23 | 99.00 | 99.54 | 99.04 | 99.84 |
| U | | | 1.5 | | 1.9 | 1.2 | 1.5 | 2 | | 1.5 | 2.4 | 1.9 |
| Th | 5.1 | 5.3 | 6.6 | 5.3 | 11.1 | 4 | 5 | 4 | 4.0 | 4.0 | 7.4 | 7.2 |
| Zr | 223 | 222 | 222 | 228 | 222 | 223 | 276 | 360 | 196 | 180 | 165 | 173 |
| Hf | | | | | | 3.9 | 4.9 | 7.7 | | 3.7 | 5.6 | 4.4 |
| Nb | 12 | 13 | 12 | 12 | 13 | 13 | 16 | 22 | 10 | 10 | 9 | 9 |
| Ta | | | | | | 1.0 | 0.9 | 1.2 | | 0.7 | 1.3 | 0.6 |
| Rb | 70 | 78 | 68 | 123 | 123 | 155 | 105 | 103 | 53 | 72 | 178 | 157 |
| Sr | 333 | 305 | 318 | 310 | 204 | 268 | 259 | 177 | 331 | 362 | 309 | 167 |
| Ba | 316 | 294 | 309 | 262 | 451 | 290 | 277 | 223 | 281 | 392 | 1277 | 572 |
| Ni | 120 | 104 | 105 | 110 | 99 | 60 | 33 | 94.0 | 100 | 84 | 173 | 100 |
| V | 356 | 281 | 285 | 309 | 258 | 220 | 142 | 390 | 277 | 332 | 367 | 210 |
| Zn | 108 | 97 | 100 | 121 | 98 | 109 | 132 | 66 | 76 | 90 | 129 | 165 |
| Ga | 20 | 20 | 19 | 20 | 20 | 18 | 18 | 25 | 19 | 19 | 19 | 19 |
| Y | 35 | 37 | 36 | 37 | 38 | 42 | 43 | 62 | 30 | 30 | 28 | 24 |
| La | 26.9 | 27.6 | | 25.9 | | 24.8 | 25.9 | 31.9 | 23.0 | 20.4 | 25.6 | 15.0 |
| Ce | 57.4 | 60.6 | | 56.2 | | 49.7 | 62.5 | 85.0 | 49.5 | 51.0 | 58.1 | 44.6 |
| Pr | | | | | | 6.7 | 8.3 | 11.8 | | 6.3 | 7.6 | 4.8 |
| Nd | 30.7 | 32.8 | | 30.8 | | 26.8 | 34.4 | 57.2 | 26.2 | 27.6 | 29.5 | 21.9 |
| Sm | 6.8 | 7.3 | | 6.7 | | 6.1 | 6.8 | 10.3 | 6.0 | 6.2 | 6.1 | 3.5 |
| Eu | 2.1 | 2.3 | | 2.0 | | 2.1 | 1.9 | 3.3 | 1.8 | 2.0 | 1.5 | 0.9 |
| Gd | 6.5 | 6.9 | | 6.4 | | 5.7 | 5.8 | 10.1 | 5.7 | 6.4 | 5.8 | 3.6 |
| Tb | | | | | | 0.99 | 0.83 | 1.54 | | 0.91 | 0.90 | 0.66 |
| Dy | 6.0 | 6.3 | | 5.7 | | 5.1 | 5.0 | 9.0 | 5.2 | 5.5 | 4.8 | 3.7 |
| Ho | | | | | | 0.97 | 1.06 | 2.00 | | 1.18 | 1.05 | 0.94 |
| Er | | | | | | 2.7 | 2.6 | 4.9 | | 2.9 | 2.5 | 2.1 |
| Tm | | | | | | 0.37 | 0.41 | 0.73 | | | 0.37 | 0.28 |
| Yb | 3.2 | 3.3 | | 2.8 | | 2.3 | 2.5 | 4.9 | 2.8 | 2.6 | 2.5 | 2.3 |
| Lu | 0.46 | 0.46 | | 0.41 | | 0.29 | 0.41 | 0.67 | 0.39 | 0.44 | 0.34 | 0.40 |
| La/Yb n | 5 | 5 | | 6 | | 7 | 7 | 4 | 5 | 5 | 7 | 4 |
| Eu/Eu* | 0.97 | 0.99 | | 0.92 | | 1.08 | 0.93 | 1.01 | 0.92 | 0.98 | 0.79 | 0.82 |
| A/CNK | 0.88 | 0.83 | 0.89 | 1.00 | 1.04 | 1.19 | 0.96 | 1.68 | 0.93 | 1.16 | 1.18 | 1.97 |
| mg# | 0.57 | 0.52 | 0.53 | 0.55 | 0.53 | 0.59 | 0.53 | 0.57 | 0.59 | 0.61 | 0.59 | 0.49 |
| Fe* | 0.57 | 0.62 | 0.61 | 0.59 | 0.61 | 0.55 | 0.62 | 0.57 | 0.55 | 0.54 | 0.55 | 0.65 |
| MALI | −2.28 | −1.93 | −1.36 | 0.78 | 1.79 | 3.58 | 2.75 | 2.54 | −0.48 | 1.07 | −1.49 | 4.87 |

Major elements (wt.%); trace elements (ppm).
A/CNK = Al2O3/(CaO + Na2O + K2O) (mol%); MALI = Na2O + K2O − CaO (wt.%); Fe* = FeOt/(FeOt + MgO) (wt.%).
mg# = MgO/(MgO + FeO) (mol%).

*6.1.3. Source rocks of the various granites and diorites*

Peraluminous leucogranites can be generated by vapor-absent melting of a variety of crustal rocks (see Skjerlie and Johnston, 1996 and references therein). High $K_2O$ and low CaO contents and a corundum normative composition roughly point to a metapelite protolith. Numerous experimental data on the vapor-absent melting of pelites and graywackes (Clemens and Vielzeuf, 1987; Montel and Vielzeuf, 1997; Vielzeuf and Holloway, 1988; Vielzeuf and Montel, 1994) bring constraints on the nature of the protoliths that have been melted as well as on the conditions of the melting process. The trace element contents of the leucogranitic melt is constrained by the mineral assemblage of the restite at the time of separation from the source. In the following discussions, we will try to constrain the nature of the protolith of the leucogranites by using their Rb, Sr and Ba concentrations and the Eu/Eu* ratios (Table 5) because these elements are strongly influenced by the behavior of micas and feldspars in the source rock (Harris and Inger, 1992). In detail, the various granites show significant differences in Rb, Sr, and Ba contents, with Eu/Eu* ratios <1 (0.3–0.8). In a Rb/Sr vs. Rb/Ba ratios diagram (Fig. 15) the granites plot on a linear array. It is to be noted that the Moulin Blanc granite (and associated foliated dykes) and the Pinet granite form a group with Rb/Sr and Rb/Ba values which are similar within errors, while the Camarat granite slightly overlaps this group but, on average, shows higher values. The Capon granite and the cross-cutting leucogranitic dykes definitely plot in the higher portion of the trend. Sylvester (1998) has suggested that high Rb/Sr and Rb/Ba ratios indicate a metapelite protolith as the source material of the granite.

*6.1.3.1. The Camarat granite.* Accepting an average pelite with 150 ppm Rb, 125 ppm Sr and 650 ppm Ba as the source composition (Harris and Inger, 1992), and a range of values for the partition coefficients as given in Table 6, equilibrium batch melting models have been calculated to account for the various granite compositions. Compared to the other granites, the Camarat granite is the richest in Rb (366 ppm) with

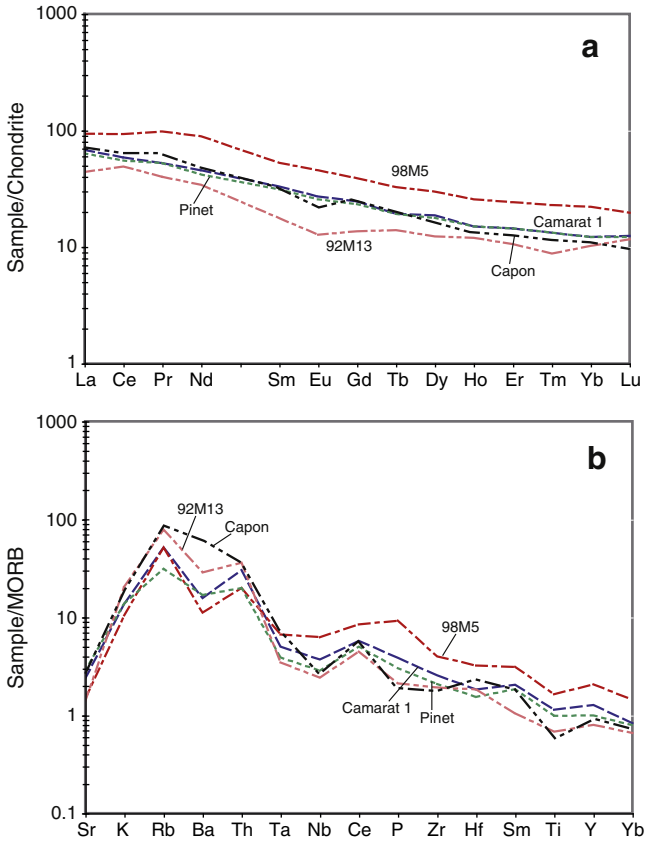


**Fig. 11.** Average trace element distribution in dolerite dykes: a. REE mantle normalized values (Sun and McDonough, 1989). b. MORB normalized values (Pearce, 1983). The REE distributions of Camarat 1, Pinet and Capon average dolerite are almost identical; Camarat 2 dyke (#98M5) is richer in REE with the same profile; sample #93M13 (Capon dolerite at the contact with granite component) is depleted in REE concentrations compared to the main Capon dolerite. Data in Table 3.

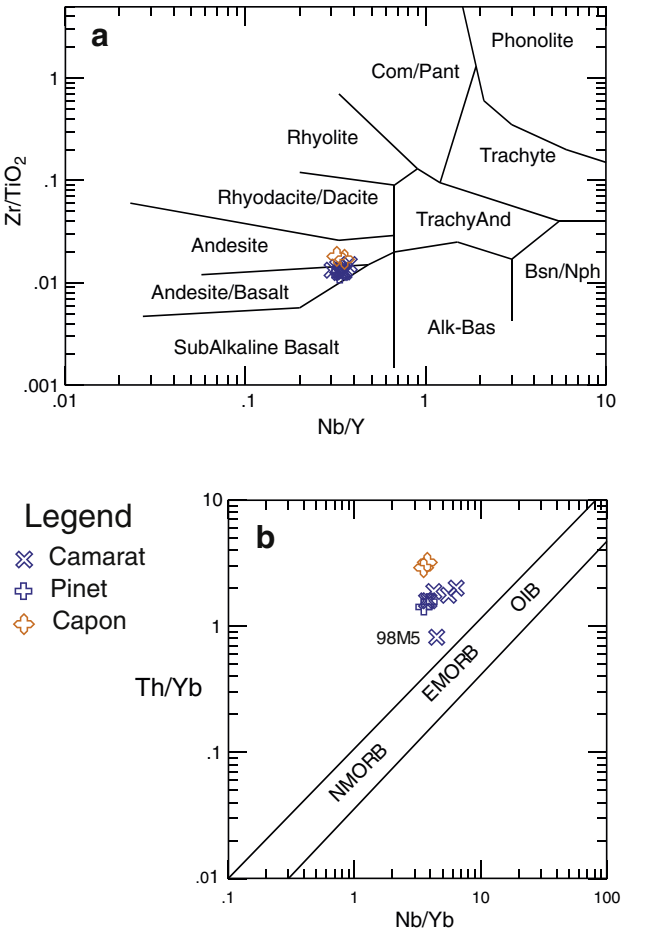


**Fig. 12.** a. $Zr/TiO_2$ vs Nb/Y discrimination diagram of Winchester and Floyd (1977). The dolerite dykes plot at the limit between andesite/basalt and andesite. b. Th/Yb vs Nb/Yb discrimination diagram of Pearce (1996). The high Th/Yb ratios are indicative of a crustal contamination, which is higher in the Capon dolerite than in the Camarat and Pinet dolerites. Data in Table 3.

moderate Ba (250 ppm) and Sr (63 ppm) concentrations. This points to the absence of biotite (which would block Rb in the residue) and the presence of K-feldspar (which would limit the enrichment of Ba in the melt) in the restitic rock. In vapor-absent conditions, with a fraction of melt F = 0.35, and a mica-free residue made up of quartz/plagioclase/K-feldspar/garnet/sillimanite in the proportions of 19/10/10/50/11, values which are close to those obtained by Vielzeuf and Holloway (1988) at 875 °C and 7 kbar, we account for the Camarat granite geochemistry, accepting some K-feldspar in the reaction products. The negative Eu anomaly in the granite corroborates the presence of feldspars in the restite or could also result from the source rock composition.

*6.1.3.2. The Moulin Blanc and Pinet granites.* In the Moulin Blanc granite and associated dykes as well as in the Pinet granite, the lower concentrations in Rb relative to the Camarat granite and Sr and Ba concentrations in the same ranges point to the presence of biotite and plagioclase in the residue. The relatively low Rb/Sr and Rb/Ba ratios are indicative of a metagraywacke source (Sylvester, 1998). Melting such a protolith in vapor absent conditions has been experimentally studied (Montel and Vielzeuf, 1997; Vielzeuf and Montel, 1994). At 10 kbar and 853 °C, these authors have obtained a residue made up of quartz/plagioclase/garnet/biotite in the proportion of 38/15/32/15 for a melt fraction of F = 0.30. It is interesting to note that the Saint-Tropez migmatitic gneisses, which are the country-rocks of the studied granites, are also metagraywackes with a major element composition (Pierre, 1979) close to that studied by Vielzeuf and Montel (1994). They also have trace elements slightly different from pelite composition with Rb = 140 ppm, Sr = 220 ppm and Ba = 500 ppm, accounting for the higher proportion of plagioclase in graywackes.

In Fig. 15, the Bonne Terrasse foliated dyke #91M4 is characterized by very low Rb/Sr and Rb/Ba ratios, definitely different from the other foliated dykes coming from the Pinet tip section. This can be taken as evidence that this dyke is related to a different source.

*6.1.3.3. The Capon granite and the cross-cutting leucogranitic dykes.* The Capon granite and the cross-cutting leucogranitic dykes have a very remarkable composition with high Rb (279 ppm) and, due to very low Sr (18 ppm) and Ba (75 ppm) concentrations, show very high Rb/Sr and Rb/Ba ratios. The high Rb value is in favor of the absence of biotite in the residue and the low Sr and Ba point to the presence of plagioclase and K-feldspar in the residue. We obtain satisfactory results with a residue made up of quartz/plagioclase/K feldspar/garnet/sillimanite in proportions 30/30/30/5/5 (close to the eutectic composition) and a fraction of melting F = 0.30. The high K-feldspar content points to a meta-arkose protolith in which we accept concentrations of Rb, Sr and Ba of 100 ppm, 90 ppm and 500 ppm, respectively. Fammenian micaceous sandstones ("psammites") with a major element composition close to the quartzo-feldspathic eutectic and adequate trace elements compositions (Wilmart et al., 1984) are plausible equivalent to the source composition.

It can be argued that the Capon and Pinet granites, which are intimately mingled with dolerite, might have been contaminated by interaction with the mafic material, thus invalidating the approach

**Table 4**
Rb–Sr and Sm–Nd isotopic compositions of rocks from granite and dolerite of the Saint-Tropez area.

| Provenance | Sample | Rb | Sr | $^{87}Rb/^{86}Sr$ | $^{87}Sr/^{86}Sr$ | ±2s | Sm | Nd | $^{147}Sm/^{144}Nd$ | $^{143}Nd/^{144}Nd$ | ±2s | $(^{87}Sr/^{86}Sr)_i$ | $\varepsilon_{Nd,300}$ | $T_{DM,1\text{-}ST}$ | $T_{DM,2\text{-}ST}$ |
|---|---|---|---|---|---|---|---|---|---|---|---|---|---|---|---|
| Moulin Blanc granite | 89M21 | 222 | 83 | 7.77 | 0.746125 | 0.000009 | 1.90 | 7.06 | 0.1628 | 0.512202 | 0.000009 | 0.712957 | −7.21 | – | 1501 |
| Moulin Blanc diorite | 98M9 | 161 | 232 | 2.01 | 0.717747 | 0.000011 | 5.21 | 26.40 | 0.1193 | 0.512172 | 0.000006 | 0.709165 | −6.13 | 1404 | 1412 |
| Foliated dyke | 91M4 | 109 | 149 | 2.13 | 0.721365 | 0.000009 | 5.82 | 21.75 | 0.1618 | 0.512132 | 0.000010 | 0.712278 | −8.54 | – | 1612 |
| Foliated dyke | 98M11 | 126 | 73 | 5.01 | 0.736754 | 0.000009 | 1.53 | 7.07 | 0.1309 | 0.512199 | 0.000012 | 0.715370 | −6.05 | 1548 | 1405 |
| Foliated dyke | 20CP | 134 | 61 | 6.39 | 0.739060 | 0.000012 | 1.83 | 7.27 | 0.1522 | 0.512189 | 0.000006 | 0.711761 | −7.06 | – | 1489 |
| Camarat granite | 89M27 | 365 | 73 | 14.56 | 0.769766 | 0.000011 | 4.99 | 25.60 | 0.1179 | 0.512259 | 0.000009 | 0.707618 | −4.38 | 1246 | 1267 |
| Camarat dyke | 98M15 | 305 | 28 | 32.42 | 0.848384 | 0.000011 | 2.78 | 9.31 | 0.1806 | 0.512359 | 0.000010 | 0.709970 | −4.83 | – | 1305 |
| Camarat dyke | 89M33 | 317 | 41 | 22.60 | 0.809487 | 0.000016 | 10.50 | 31.40 | 0.2022 | 0.512350 | 0.000009 | 0.713012 | −5.83 | – | 1388 |
| Camarat dyke | 98M2 | 451 | 12 | 113.5 | 1.151702 | 0.000012 | 3.15 | 12.40 | 0.1536 | 0.512374 | 0.000009 | 0.667071 | −3.50 | – | 1196 |
| Pinet granite | 91M2 | 216 | 57 | 11.08 | 0.757451 | 0.000011 | 1.60 | 8.90 | 0.1087 | 0.512302 | 0.000010 | 0.710158 | −3.19 | 1078 | 1170 |
| Capon granite | 91M6 | 177 | 15 | 34.43 | 0.859165 | 0.000010 | 1.12 | 3.92 | 0.1728 | 0.512295 | 0.000013 | 0.712191 | −5.78 | – | 1383 |
| Capon granite | 98M8 | 365 | 28 | 39.53 | 1.031182 | 0.000014 | 1.31 | 3.23 | 0.2453 | 0.512392 | 0.000007 | 0.862594 | −6.67 | – | 1456 |
| Capon tonalite | 91M12b | 33 | 72 | 1.33 | 0.713782 | 0.000009 | 2.08 | 8.17 | 0.1540 | 0.512325 | 0.000007 | 0.708124 | −4.47 | – | 1275 |
| Cross-cutting dyke | 98M14 | 346 | 18 | 57.12 | 0.980193 | 0.000012 | 1.08 | 4.00 | 0.1635 | 0.512410 | 0.000012 | 0.736342 | −3.18 | – | 1169 |
| Cross-cutting dyke | 89M46 | 210 | 16 | 39.47 | 0.896954 | 0.000016 | 0.70 | 2.00 | 0.2117 | 0.512418 | 0.000012 | 0.728466 | −4.87 | – | 1308 |
| Dolerite Camarat | 98M1 | 155 | 268 | 1.67 | 0.712295 | 0.000009 | 6.10 | 26.80 | 0.1377 | 0.512507 | 0.000005 | 0.705148 | −0.29 | 1076 | 934 |
| Dolerite Camarat | 98M3 | 105 | 259 | 1.17 | 0.710356 | 0.000010 | 6.78 | 34.40 | 0.1192 | 0.512484 | 0.000008 | 0.705346 | −0.04 | 908 | 913 |
| Dolerite Camarat 2 | 98M5 | 103 | 177 | 1.69 | 0.712321 | 0.000010 | 10.30 | 57.20 | 0.1089 | 0.512390 | 0.000004 | 0.705129 | 2.43 | 672 | 715 |
| Dolerite Pinet | 91M3 | 53 | 330 | 0.468 | 0.711801 | 0.000009 | 6.00 | 26.20 | 0.1385 | 0.512562 | 0.000009 | 0.709801 | 0.75 | 980 | 850 |
| Dolerite Capon | 91M7 | 178 | 309 | 1.67 | 0.714553 | 0.000009 | 6.13 | 29.45 | 0.1259 | 0.512319 | 0.000006 | 0.707432 | −3.51 | 1255 | 1197 |
| Dolerite Capon | 92M13 | 157 | 167 | 2.72 | 0.720659 | 0.000012 | 3.46 | 21.90 | 0.0955 | 0.512299 | 0.000007 | 0.709051 | −2.74 | 964 | 1133 |

used here. The Capon dolerite is characterized by concentrations of Sr (309 ppm) and Ba (1277 ppm) (Table 3), much higher than in the Capon granite (Table 2). Given the low Sr and Ba contents in the Capon granite a (bulk or a selective) contamination by the dolerite can be precluded. Similarly the higher Sr concentration in the Pinet dolerite than in the associated granite makes a bulk contamination unlikely.

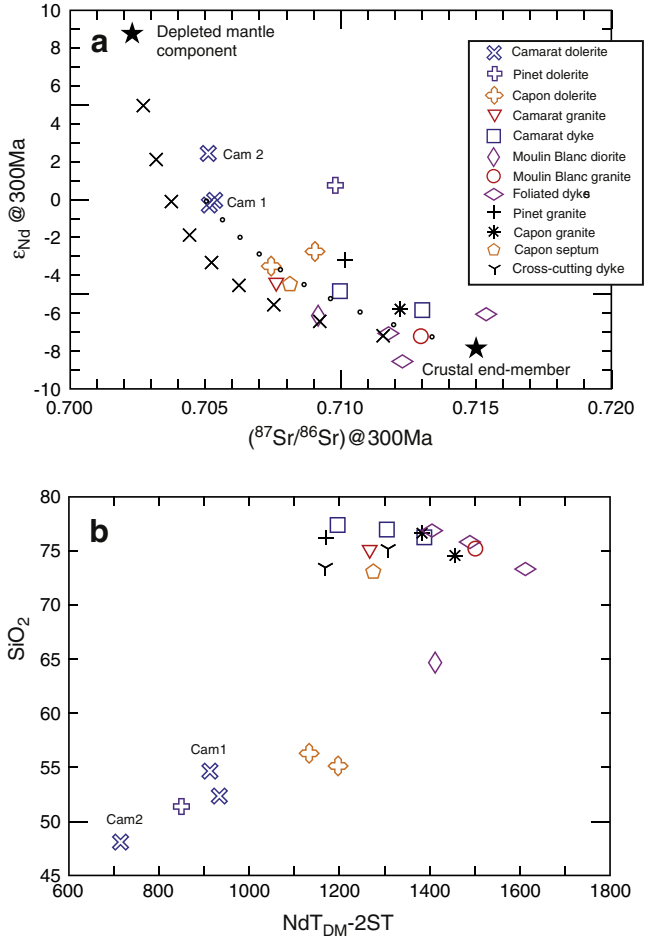


**Fig. 13.** a: $\varepsilon_{Nd}$ vs $^{87}Sr/^{86}Sr$ ratios at 300 Ma in representative samples of the Saint-Tropez granites and dykes. The stars are the end-member components of the Variscan crust in the French Massif Central in the model of Downes et al. (1990). Mixing hyperbolae linking the crustal end-member with the depleted mantle component and the Camarat 1 dolerite are shown with 10% ticks. b: $SiO_2$ vs $NdT_{DM}$-2ST values. Data in Table 4.

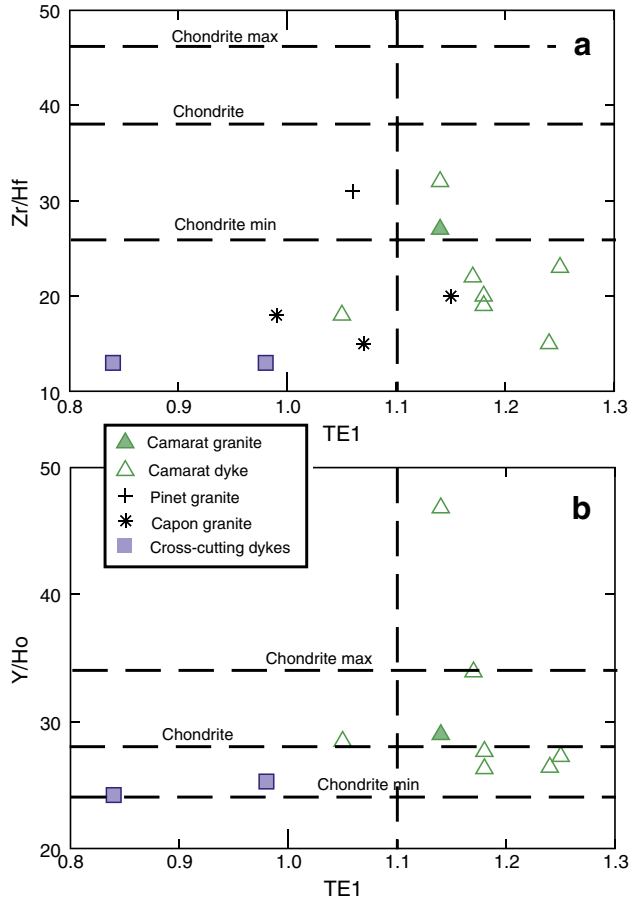


**Fig. 14.** a: Zr/Hf vs TE1 in the Camarat, Pinet and Capon granites and in cross-cutting leucogranitic dykes. Most Camarat dykes show a distinct Tetrad effect with low Zr/Hf ratios. The cross-cutting leucogranitic dykes have Zr/Hf ratios similar to the Capon granite. Range of chondrite values for Zr/Hf ratio from Bau (1996). b: Y/Ho vs TE1 in the same samples. Chondrite values from Bau (1996). Only one Camarat dyke sample shows an anomalous Y/Ho value. Data in Table 2.

**Table 5**
Synthesis of geochemical characteristics of the Saint-Tropez granites.

| | Moulin Blanc | Foliated dykes | Pinet | Camarat | Capon | Cross-cut. dykes |
|---|---|---|---|---|---|---|
| $SiO_2$ | 74.7 (7)[a] | 74.4 (13) | 75.4 (7) | 75.1 (15) | 75.6 (10) | 75.2 (12) |
| CaO | 0.38 (17) | 0.53 (12) | 0.54 (16) | 0.59 (8) | 0.44 (4) | 0.29 (9) |
| $Na_2O$ | 3.5 (4) | 3.5 (5) | 3.6 (7) | 3.3 (3) | 5.0 (5) | 4.4 (8) |
| Rb | 204 (26) | 134 (6) | 185 (38) | 367 (8) | 253 (99) | 239 (79) |
| Sr | 95 (17) | 59 (15) | 58 (15) | 63 (19) | 21 (6) | 14 (3) |
| Ba | 473 (62) | 207 (61) | 287 (49) | 250 (104) | 85 (27) | 45 (7) |
| Rb/Sr | 2.2 (7) | 2.5 (10) | 3.4 (14) | 6.4 (23) | 11.9 (12) | 16.7 (46) |
| Rb/Ba | 0.4 (1) | 0.7 (2) | 0.7 (2) | 1.7 (9) | 2.9 (2) | 5.4 (19) |
| Sr/Ba | 0.20 (1) | 0.29 (7) | 0.21 (5) | 0.26 (4) | 0.25 (2) | 0.33 (9) |
| Eu/Eu* | 0.80 (2) | 0.57 (40) | 0.55 (13) | 0.32 (15) | 0.46 (3) | 0.19 (12) |

[a] Units in parentheses are 1 SD of replicate analyses in terms of the last unit(s) cited.

**Table 6**
Mineral/melt partition coefficient for granitic/rhyolitic compositions (Bea et al., 1994; Ewart and Griffin, 1994; Henderson, 1982; Nash and Crecraft, 1985).

| | Biotite | K-feldspar | Plagioclase | Reference |
|---|---|---|---|---|
| Rb | 3.4 | 0.38 | 0.09 | Henderson (1982) |
| | **9.6** | 0.11–0.74 | **0.011–0.029** | Ewart and Griffin (1994) |
| | 6.98 | **2.85** | 0.06 | Bea et al. (1994) |
| | **3.2** | 1.2–2.4 | 0.06–0.19 | Nash and Crecraft (1985) |
| Sr | **0.24** | 9.4 | 6 | Henderson (1982) |
| | 0.25 | **2.1–22.1** | **4.4–12.2** | Ewart and Griffin (1994) |
| | 0.29–0.53 | 4.5–7.3 | 6.8–33 | Nash and Crecraft (1985) |
| Ba | 7.6 | 6.6 | **0.5** | Henderson (1982) |
| | **3.7–7.0** | **2.7–20.9** | 1.0–1.8 | Ewart and Griffin (1994) |
| | 5.6–36 | 4.9–24 | 0.6–3.3 | Nash and Crecraft (1985) |

Values adopted in granite modeling are shown in bold.

In conclusion, the geochemical signature is consistent with fluid-absent equilibrium melting processes of metapelitic, metagraywacke and meta-arkose protoliths. The fraction of melt produced ranges between 0.30 and 0.35, values well above the melt extraction threshold (Sawyer, 2008; Vigneresse et al., 1996) from the source rock.

*6.1.3.4. The Moulin Blanc diorites.* Three different dioritic melts have been identified in the Moulin Blanc intrusion on the basis of the major and trace element contents (Fig. 7): (1) the MMEs which form the mafic pole of the linear trend (#10MB and #98M9); (2) a dioritic melt represented by the foliated sample #89M52; and (3) the massive diorite (intruded late in the deformation of the surrounding granite or after) (#89M19).

The occurrence of several melts of intermediate compositions associated with granites has been reported in numerous cases (e.g. Bogaerts et al., 2003; Duchesne et al., 2008; Jung et al., 2002; Vander Auwera et al., 2003 and many others) and their formation as melting product of mafic rocks has been studied experimentally by a number of authors (Rapp and Watson, 1995; Rushmer, 1991 and references therein). We focus here on the dehydration melting of metabasalt experiments of Rapp and Watson (1995) in order to identify the various source rocks of the 3 types of diorite documented in the Moulin Blanc pluton.

We first note that, discarding Na, K and Ca that might have been modified by interaction with the associated granitic melts, the other elements Si, Al, Mg and Fe in MMEs and the foliated diorite can be compared to the composition of partial melts produced in the 1025–1050 °C range at 8 and 16 kbar from the alkali basaltic and high-aluminous basaltic amphibolites (see Fig. 4 of Rapp and Watson, 1995). The other two amphibolite compositions (migmatitic amphibolite and Archaean greenstone) studied by these authors give partial melts much higher

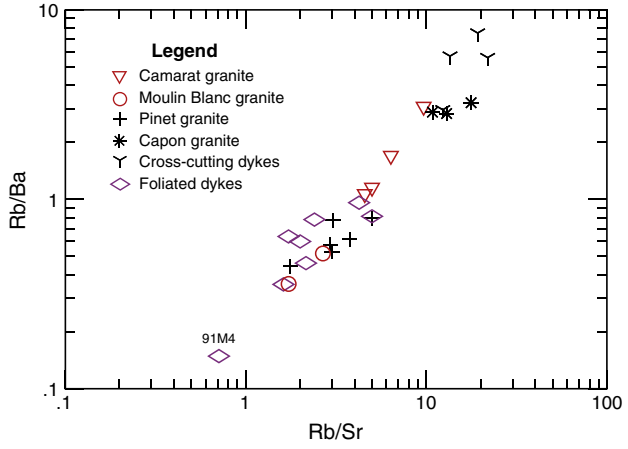


**Fig. 15.** Rb/Ba vs Rb/Sr ratio diagram for the Camarat, Pinet, Capon and Moulin Blanc granites, as well as for the foliated and cross-cutting leucogranitic dykes. Note the very low values of dyke sample #91M4 (from the Bonne Terrasse tip).

in $FeO_t$ in this P–T range, and may be rejected as potential source rocks. For the MMEs, we further use the REE distributions to refine the discrimination process. In an equilibrium melting model, using commonly used partition coefficients (viz. those of Martin, 1987), we calculate the REE concentrations of the melts in equilibrium with the residue for a given melt fraction. Using as a source an amphibolite having the composition of a high-alumina basalt (composition no. 2 of Rapp and Watson, 1995), melting at 16 kbar and 1035 °C produces a residue made up of clinopyroxene/garnet/plagioclase/amphibole in the proportions 61/15/12/12 with a melt fraction of 0.18 (Rapp and Watson, 1995). Considering that the source has an E-type (LREE-enriched) mid-ocean ridge REE pattern, we have calculated that the melt in equilibrium with this residue has a REE pattern very similar to the Moulin Blanc MME composition. It is thus possible to account for the major and trace elements compositions of the Moulin Blanc MMEs by melting an amphibolite in the garnet stability field, i.e. definitively over 8 kbar.

A similar approach has been used to identify the source rock of the massive diorite #89M19 characterized by a lower $[La/Yb]_N$ than the MME. At 8 kbar and 1050 °C, melting an alkali-basaltic amphibolite leaves a residue containing plagioclase/orthopyroxene/amphibole/olivine in the proportions 47/27/16/10 and gives a melt in a 27% proportion. This source rock has a mild N-type (slightly light REE-depleted) mid-ocean REE pattern (composition no. 1 of Rapp and Watson (1995)) which explains the lower $[La/Yb]_N$ in the diorite. Moreover, we had to add 3% of garnet to the residue for correctly accounting for the low Yb content, which indicates that the source amphibolite was probably melted slightly over 8 kbar. This amphibolite was also clearly enriched in P and Nb compared to the MME source.

The foliated diorite #89M52 has a MgO content of 3.46%, and a Cr concentration of 150 ppm, much higher than in the other two diorite types, and this value cannot be produced by partial melting of any of the source amphibolites investigated by Rapp and Watson (1995). The high values of these elements suggest that the protolith of this amphibolite was a mafic mineral cumulate rather than a metabasalt, and this type of rock has not been investigated by Rapp and Watson (1995). It is thus not possible to assess the residue composition and the melting process cannot be quantitatively modeled. However, the $[La/Yb]_N$ value of 5, higher than in the massive diorite and lower than in the MME, suggests that the source rock was an amphibolite with a garnet content intermediate between the other two amphibolites.

*6.1.4. Dyke transport of granitic magmas*

In the Pinet–Capon section, the folded granitic dykes related to the Moulin Blanc granite (see Fig. 3D) and the cross-cutting leucogranitic dykes (see Fig. 4D), display average thicknesses of 40 cm and 15 cm, respectively. This character permits to constrain the physical mechanism of emplacement of the granitic melt. On the basis of fluid-dynamical analyses, it has been suggested that melt emplacement and propagation in dyke were controlled by viscosity and density contrast with country rocks (Clemens and Mawer, 1992; Petford et al., 1993, 1994).

Following Petford et al. (1993), the critical dyke width $w_c$ required to transport melt through the crust can be estimated as follows:

$$w_c = 1.5\left(S_m/S_\infty^2\right)^{3/4}(\mu\kappa H/g\Delta\rho)^{1/4}$$
$$\text{with } S_\infty = L/c(T_{sol}-T_{enc}) \text{ and } S_m = L/c\left(T_{liq}-T_{sol}\right)$$

in which the gravitational acceleration $g = 9.8\ ms^{-2}$, $\Delta\rho$ is the density contrast between the melt and the country rocks (a value close to 400 kg/m$^3$), $\mu$ is the magma viscosity controlled by temperature, composition and $H_2O$ content, $H$ is the dyke length, $\kappa$ is the thermal diffusivity (0.008 cm$^2$/s), $L$ is the latent heat of solidification (418 J/g), $c$ is the specific heat (1.254 J/g °C), and $T_{liq}$, $T_{sol}$ and $T_{enc}$ are the initial, freezing and country rock temperatures, respectively. It is clear from the formulae that the parameter $S_\infty$ which reflects the temperature difference between the freezing temperature and the regional temperature is the strongest constraint on the dyke critical width, the lower its value, the larger the dyke width. In the present cases, several parameters need not be estimated with accuracy and, thus, we assume that (1) the dyke length $H$ is 1000 m, the distance from outcrop to a possible magma chamber; (2) the $H_2O$ content of the magma is 6%, a conservative value for leucogranitic melts (Holtz and Johannes, 1994), and (3) the freezing temperature $T_{sol}$, which is independent of the water content (Johannes and Holtz, 1996) is taken at 640 °C. The viscosity $\mu$ can be calculated from the chemical composition with the model of Giordano et al. (2008) at various temperatures.

The Moulin Blanc granite emplaced at 301 ± 2 Ma shortly before exhumation and crossing of the closing temperature of the K–Ar system of white micas in the 400–450 °C range at 301.5 ± 0.6 Ma (see above). A conservative regional temperature of 450 °C can thus be considered. Assuming a typical melt temperature of 800 °C and a water concentration of 6 wt.% (Johannes and Holtz, 1996), the average composition of dyke samples #89M15 and #89M16 leads to $\mu = 4.59$ log units and critical dyke width $w_c$ of 3.3 m, that is nearly an order of magnitude higher than the observed width (*c.* 40 cm). Allowing extreme values of $L = 900$ J/g and $\Delta\rho = 600$ kg/m$^3$ (Scaillet, pers. comm.) and reducing $H$ to 500 m, lowers $w_c$ to 1.4 m, a value still well above the dyke width.

The Camarat granite crossed the 400–450 °C white mica closing isotherm at 299.8 ± 0.3 Ma. It can thus be accepted that the regional temperature was lower when the dolerites and related cross-cutting leucogranitic dykes intruded. The composition of sample #98M14 gives a $\mu = 4.42$ log units at 800 °C and $H_2O$ concentration of 6 wt.%. Assuming conservative values of the regional temperatures of 400 °C and 450 °C, brings the critical width to 4.2 m and 3.0 m, respectively. If the granitic melt was superheated by its contact with the doleritic melt up to say 1000 °C, the resulting viscosity would be 3.00 log units and the $w_c$ at 400 °C and 450 °C would be 1.0 m and 0.7 m, respectively. With the extreme values of $L$, $\Delta\rho$ and $H$ considered above, the $w_c$ becomes 0.44 m and 0.31 m for regional temperatures of 400 °C and 450 °C, still more than twice the observed dyke width.

The above calculations highly suggest that, in the present case, buoyancy of the granitic melt is not sufficient to transport granitic magmas in thin dykes. An externally applied tectonic stress gradient related to transpression could have played a role in the emplacement of the dyke material, especially for the foliated and folded Moulin Blanc dykes that were obviously affected by the transpression (see below the discussion of the tectonic status of the dykes). Assuming that the granitic melt could have exploited tension fractures, it can also be stated that, as the dyke opens, the pressure drop between the opening fracture and the surrounding rock could be the driving force ["sucking" veins of Clemens and Mawer (1992)]. Another possibility is that the leucogranitic melt could have degassed during ascent, thus becoming overpressured by the volatiles release. The low pressure of emplacement would favor such boiling of the melt before complete solidification (Annen et al., 2006; Holtz and Johannes, 1994). A haplogranitic magma starting at 800 °C with 6 wt.% $H_2O$ and 50% melt (the model presented above) and ascending adiabatically would be boiling at *c.* 2 kbar (Holtz and Johannes, 1994).

### 6.2. The doleritic dykes

#### 6.2.1. Evidence of alteration processes

Noteworthily, the major elements that show the largest variations in the doleritic samples, i.e. $SiO_2$, CaO, $K_2O$ and $Na_2O$, are known to be mobile in metasomatic processes. On the other hand, except #98M5, all dolerites (Camarat 1, Pinet and Capon) cluster in one group in the triangular plot of $Al_2O_3$, $FeO_t$, and MgO, elements that are generally considered as immobile or less mobile (Besson and Fonteilles, 1974) (Fig. 16). This strongly suggests that the observed geochemical variations result from the mobility of some elements. The isocon diagram of Fig. 17 (Grant, 1986), in which the Camarat 1 dolerite samples displaying the lowest and the highest $SiO_2$ contents are compared, confirms the immobility of Al, Fe, Mg, Ti, Zr, Nb, REE and Th (which plot on the isocon or close to it), and the mobility of Si, Na, Ca, Ni, V, Ba and Sr. K and Rb appear immobile in the present case, but this is an exception because, for other pairs of samples, the mobility is the rule. In agreement with the petrographic description, it can be concluded that the dolerites have been affected by alteration processes (hydrothermal alteration and/or weathering), and that the observed elemental variations, particularly between the Camarat, Pinet and Capon samples, are not due to a differentiation process such as fractional crystallization. This conclusion is corroborated by the small variation in HFSE and REE concentrations. This approach also confirms that ratios of immobile elements can be used to discriminate the nature of the primary magma – in the present case, an andesite basalt–, as proposed by Pearce (1996) and Winchester and Floyd (1977). The very low CaO content of dolerites #98M5 (Camarat 2) and #92M13 (contact sample with the granite component in the Capon composite dyke) is a good evidence that these rocks have also been altered. This makes modeling of a relationship with Camarat 1 dolerites and the Capon dolerite, respectively, difficult. In #92M13, the REE distribution (Fig. 11) has been modified but not the Th/Yb and Nb/Yb ratios (Fig. 12b).

#### 6.2.2. Evidence of crustal contamination in dolerites

In the dolerites, crustal contamination or interaction with coeval granitic melts is also revealed by considering the $\varepsilon_{Nd}$ at 300 Ma. The

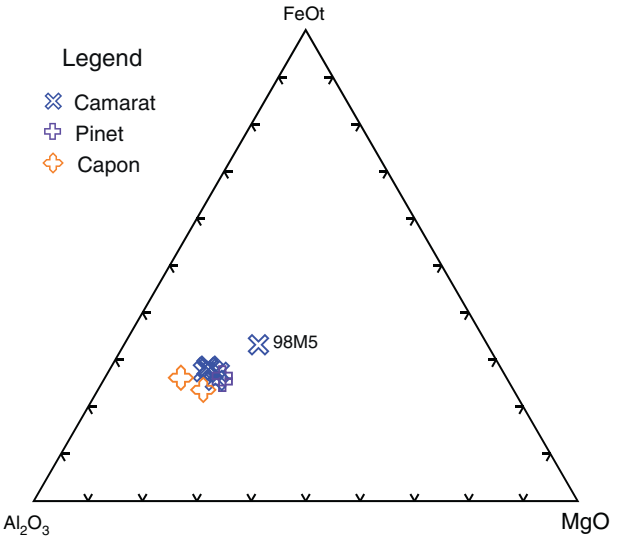


**Fig. 16.** Dolerite samples plotted in $Al_2O_3$–$FeO_t$–MgO triangle. The slight scattering of the points in the immobile element plot confirms that the Camarat 1 and Pinet dolerites are not fractionated. The Capon samples are slightly more aluminous than the Camarat 1 and Pinet dolerites.

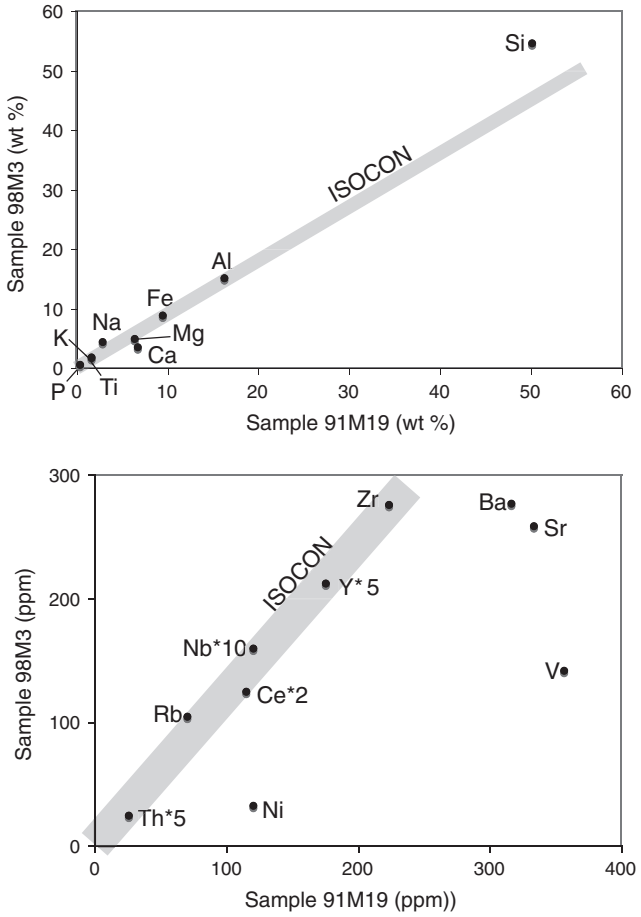


**Fig. 17.** Major and trace element composition in sample #98M3 (the highest $SiO_2$ content) vs composition in sample #91M9 (the lowest $SiO_2$ and probably the less affected by metasomatic alteration in Camarat 1 samples). The concentrations of Th, Ce, Nb and Y have been multiplied by 5, 2, 10 and 5, respectively, in order to avoid scale changes. Data in Table 3.

values of the Camarat 1 dolerite are distinctly lower than in Camarat 2 and this can be accounted for by crustal contamination (Fig. 13). Accordingly, the Th/Yb ratios are higher in Camarat 1 than in Camarat 2 (Fig. 12b). The Capon dolerite shows a more negative $\varepsilon_{Nd}$ at 300 Ma value and a higher Th/Yb ratio than the Camarat dolerite (Figs. 11 & 12), again either due to crustal contamination or to interaction with coeval granite. The Capon contact dolerite #98M13, shows a similar isotopic signature to the sample collected at the interior of the dolerite pillow (#91M7) in agreement with similar Th/Yb and Nb/Yb ratios (Fig. 12a). This indicates that the isotopes were not modified by the alteration processes revealed above by the REE and the major elements.

*6.2.3. Chasing the primary composition*

Sample #91M19 in the Camarat 1 dyke, with the lowest $SiO_2$ and $K_2O$ contents for the highest MgO content of the Camarat 1 dyke samples, can be accepted as the least altered sample. It very much resembles the Andean andesite basalt reported in Table 7.2 of Wilson (1988), all elements differing by less than 12% of their contents, and Nb/Yb, Th/Yb and Zr/Y ratios being similar. Such composition is also in agreement with that obtained in the Winchester and Floyd discrimination diagram (Fig. 12). This conclusion is valid for the source composition only, and is not indicating a subduction-related environment, the remelting of a mafic crustal source generated by a previous subduction being also an adequate model for generating the observed compositions. The Camarat 1, Pinet and Capon dolerite isotopic signatures, with negative $\varepsilon_{Nd}$ values, preclude a mantle origin and, thus, several crustal processes can be envisaged. Dehydration-melting of metabasalts (amphibolites) (e.g. Petford and Atherton, 1996) or mixing between silicic magmas produced in the crust and mantle-derived magmas (e.g. Heiken and Eichelberger, 1980) are possible mechanisms.

*6.2.4. Composite dykes: why they are mingled rather than mixed?*

The occurrence of dolerite-granite composite dykes in the Pinet–Capon section permits to investigate the thermal and mechanical/viscosity constraints on mixing between mafic and felsic magmas in contact. This problem was tackled by the pioneering work of Fernandez and Gasquet (1994), Frost and Mahood (1987), Scaillet et al. (1999) and Sparks and Marshall (1986) among others. Given that the heat diffusion is several orders of magnitude faster than chemical diffusion in silicate melts, Sparks and Marshall (1986) pointed out that the temperature at which the system comes to thermal equilibrium is the crucial parameter to describe the state of the system. This equilibrium temperature θ can be calculated with the following equation, adapted from Eq. (3) of Sparks and Marshall (1986) and considering that the felsic magma contains no crystals (superheated melt):

$$\theta = (-1/C)[T_f C(x-1) - x(XL + CT_m)] \quad (1)$$

in which $T_m$ and $T_f$ are the mafic and felsic magma temperatures, respectively, C the heat capacity of the magmas (taken at 1.254 J/g °C), L the heat of crystallization of the solid phases (taken at 418 J/g), x the proportion of the mafic magma and, importantly, X its crystallinity. The latter factor can be estimated by various methods: experimentally (e.g. Scaillet et al., 1999), as an error function of temperature (Frost and Mahood, 1987), or by analogy with natural suites of rocks (Sparks and Marshall, 1986). We suggest here to use the PELE algorithm (Boudreau, 1999) to calculate the crystal content of the magma. This software also allows calculation, at the temperature of interest, of the viscosity of the melt from its composition (following the data of Giordano et al. (2008)) and the viscosity of the bulk magma following the Roscoe–Einstein relationship with the parameter values of McBirney and Murase (1984). An iterative process using Eq. (1) and PELE permits to calculate for various proportions of mafic magma x, the equilibrium temperature θ and the corresponding crystallinity of the mafic magma X.

We consider the two cases illustrated at Fig. 4 with x and θ values respectively of 0.85 and 1217 °C (case 1, Fig. 4C) and 0.35 and 997 °C (case 2, Fig. 4A). Results of the calculation are reported in Fig. 18. The dolerite with 2% $H_2O$ is less viscous than the granites with 4% and 6% $H_2O$ in case 1 and both components are liquids that could have mixed. Nevertheless, as there is no evidence of mixing between the two magmas, this can be explained only by the rapid cooling of the dyke. Similarly, in case 2, the two components are liquid and the dolerite magma is now more viscous than the granites. Again there is no indication of mixing or hybridization. It must be noted that in this case the interstitial melt of the dolerite has the same viscosity as the 4% $H_2O$ granite, a case that would particularly favor mixing. We are forced to admit that in this case the kinetic conditions also prevented the mixing process. The cases that are considered here are theoretical because some parameters such as the $H_2O$ content of the mafic and felsic components have been chosen somewhat arbitrarily. We however think that a better knowledge of their values will not significantly change the conclusions.

The Capon composite dyke permits to tackle another problem, the origin of the leucotonalitic septum. A similar approach to that of the Pinet composite dyke leads to the same conclusion, the leucotonalitic melt viscosity at the equilibrium temperature is close to the dolerite interstitial melt viscosity, but the two magmas do not show any evidence of hybridization. Moreover the granitic component of the dyke is not modified. This implies that the leucotonalitic septum is xenolithic, either a melted inclusion of leucotonalite, or a granitic melt which has been chemically modified before being mingled with the dolerite. This

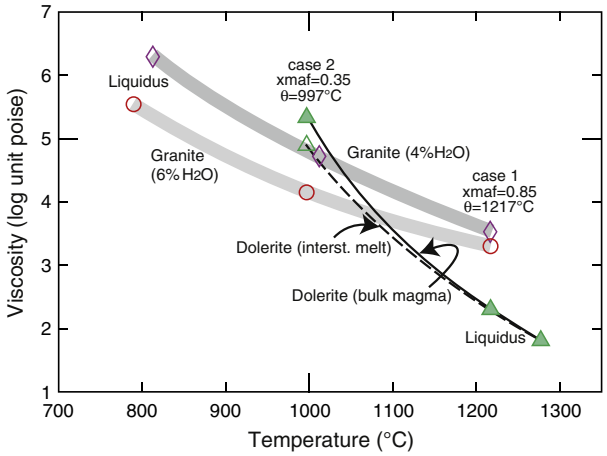


**Fig. 18.** Viscosity values (poise, log unit) vs temperature (°C) diagram illustrating the thermomechanical properties of the Pinet composite dykes. The dolerite composition (triangle) is the average of samples #91M8 and #91M9 (Table 1) with 2% $H_2O$ content. With FMQ as the oxygen buffer and at 2 kbar pressure, the liquidus temperature is 1277 °C. The viscosity increases rapidly with decreasing temperature partly due to the temperature fall and the crystallinity increase. The evolution of the interstitial melt viscosity (dashed line) is slightly less rapid than that of the bulk magma (melt + crystals). The felsic compositions which are modeled are the average Pinet granite with 4% (losange) and 6% $H_2O$ (circle) contents at FMQ buffer and 2 kbar pressure. The felsic liquidus temperature is *c.* 800 °C and the viscosities of the superheated felsic melts decrease with increasing temperatures. In case 1 ($x_{maf} = 0.85$), the crystallinity of the dolerite is 0.05 and both magmas are liquids at the equilibrium temperatures (*c.* 1217 °C) and, thus, could mix. In case 2 ($x_{maf} = 0.35$), the dolerite crystallinity is 0.33 and it has now a higher viscosity than the 6% $H_2O$ granite, both components being liquids, but the 4% $H_2O$ granite viscosity is equal to the viscosity of the dolerite interstitial melt, an ideal condition for mixing and hybridization.

interaction has most probably taken place in a magma chamber at a deeper level in the crust than the dyke emplacement.

## 7. Geotectonic considerations

Granite plutons and associated dykes of the Saint-Tropez peninsula that are investigated in the present work, as well as other granitic bodies from the Maures–Tanneron Massif (Demoux et al., 2008) emplaced in a very short period of time (a few myr), at about 300 Ma. This age falls within the period (315–290 Ma) when large post-collisional granitic bodies were emplaced in Southern Variscides (Orejana et al., 2012 and references therein).

According to current models of Variscan evolution of the Maures–Tanneron Massif (Bellot, 2005; Corsini and Rolland, 2009; Rolland et al., 2009), this short-lived period of magmatism took place during the last phase of deformation ($D_4$). We propose, however, that the Moulin Blanc granite and related dykes were emplaced during the $D_3$ phase, probably at the $D_3$–$D_4$ transition. Indeed, structural arguments (strong foliation in the Moulin Blanc granite vs. poorly defined fabric in the Camarat granite, plus crosscutting relationships between the cross-cutting leucogranitic dykes and the foliated and folded granitic dykes related to the Moulin Blanc granite), as well as modifications of the geochemical signature of the granites indicate that the Moulin Blanc granite and related dykes emplaced first, in a different context. This context is probably that of the $D_3$ phase, since the Moulin Blanc dykes are affected by upright folds, a fold style which is typical of the $D_3$ phase. Emplacement at the $D_3$–$D_4$ transition is suggested by the occurrence, in the Moulin Blanc granite, of a diorite showing a poorly defined fabric (#89M52), which seems to be the structural signature of igneous bodies emplaced during the $D_4$ phase.

There is a general agreement to ascribe $D_3$ (and the previous phase, $D_2$) to transpressive tectonics due to oblique collision, but the status of the $D_4$ phase is still debated. Based on the occurrence of ductile-brittle normal faults in the western and central units of the Maures Massif, it has been argued that the $D_4$ phase could witness a classical syn- to post-orogenic extensional regime such as the one evidenced in the French Massif Central (Bellot, 2005 and references therein). This extensional (or transtensional) regime would correspond to the beginning of the N–S Permian extension marked in the western and northern Maures Massif by a series of grabens well-marked in the sedimentary record (Toutin-Morin et al., 1993) and by volcanism marking a lithospheric thinning (Lapierre et al., 1999). Following Rolland et al. (2009), extensional movements during the $D_4$ phase are not ascribed to regional extension, but accommodated doming and exhumation in the ongoing transpressional context that would have lasted up to the infill of the intracontinental basins. The latter interpretation is in keeping with an evolution model considering that the Maures–Tanneron Massif was experiencing post-collisional transpression at 320–300 Ma, whereas at the same time other portions of the Variscan chain, such as the French Massif Central, were in a context of extensional tectonics (Corsini and Rolland, 2009; Rolland et al., 2009). Following the most recent models (Carosi et al., 2012; Guillot and Ménot, 2009), such a transpressional tectonic setting was widespread in the SE branch of the Variscan belt in late-Variscan times, along the northern margin of Gondwana that acted as a major shear zone (Fig. 19).

It is worth noting that the emplacement of the Camarat granite, the dolerite dykes and associated cross-cutting leucogranitic dykes, that are all E–W-striking, seems to have been favored by a N–S extension. This cannot be taken as an argument of a generalized N–S extensional regime, firstly because the transpressional context in the Maures–Tanneron Massif is featured by a combination of E–W shortening (N–S folding) and N–S stretching (N–S-striking mineral and stretching lineations) (Rolland et al., 2009). Secondly, E–W aplite and (leuco)granite dykes are also observed further north, where they cut across the Plan-de-la-Tour–Rouet granite (Onézime et al., 1999). These dykes testify syn- to post-magmatic N–S stretching and are associated with evidence of dextral N–S strike-slip movement at the pluton margins, suggesting that the emplacement of the Plan-de-la-Tour–Rouet granite was controlled by a dextral pull-apart along the Grimaud–Joyeuse Fault (Onézime et al., 1999).

Whatever their exact tectonic significance, the Saint-Tropez granitic intrusions and related dykes are a relevant illustration of the functioning of a deep crustal hot zone, a concept defined by Annen et al. (2006). In this model, a hot zone is generated by the emplacement at various levels in the crust of sill-like intrusions of mantle-derived basaltic magmas. Numerical modeling shows that the hot zone can trigger melting of the crust and produce intermediate to silicic melts. The resulting magmas can ascend through dykes from the hot zone to shallower storage reservoirs where they crystallize. Melts from different portions of the hot zone can mix or mingle at the source prior to ascent, in the feeder dykes, or in the reservoirs.

Accepting the model of Corsini and Rolland (2009) and Rolland et al. (2009), the hot zone would be linked in the present case to the development of an orogen-parallel shearing in a transpressional regime due to oblique collision, related to a major shear zone bounding Gondwana (Fig. 19; Carosi et al., 2012; Guillot and Ménot, 2009). Heating of the crust and intrusion of mantle-derived basalts resulted from bringing into contact the asthenospheric mantle with the base of the crust. This requires some form of detachment of the lithospheric mantle along the shear zone either by linear delamination (Lachenbruch et al., 1985; Teyssier and Tikoff, 1998) or convective removal (e.g. Platt and England, 1994).

## 8. Conclusions

The Moulin Blanc cordierite granite emplaced in a transpressional regime at 301 ± 2 Ma, during the post-collisional granitic period of Southern Variscides (310–290 Ma; Orejana et al., 2012) resulting from the oblique collision between Gondwana and Laurentia, and giving rise to continental-scale strike-slip movements (Matte, 2001). It was


**Fig. 19.** Terrane map of Western Europe at *c.* 300 Ma based on Ballèvre et al. (2009) and modified with information from Carosi et al. (2012) and Guillot and Ménot (2009). The Maures Massif straddles the large shear zone bounding Gondwana. Major dextral transpression period (320–300 Ma) following Rolland et al. (2009). Minor sinistral transtension (300–298 Ma) suggested in this study.

quickly exhumed through the 400 °C–450 °C white mica isotherm. The intrusion was built up by successive inputs of magmas formed in a deeper magma chamber in which hybridization, mixing and mingling processes could have taken place. It perfectly illustrates the formation of a pluton in a stressed environment, following the concept developed by Vigneresse (2004) among others. The Moulin Blanc series of rocks was formed by mixing between a dioritic melt (MME) and a peraluminous granite melt. The former was produced by dehydration melting of a garnet amphibolite with an E-type high-alumina composition at 16 kbar and 1035 °C. The latter resulted from the melting at 10 kbar and 853 °C of a metagraywacke source, similar to the Saint-Tropez migmatitic gneiss. The two other types of diorites involved in the Moulin Blanc system are produced by melting at *c.* 8 kbar of an alkali-basaltic amphibolite and of an amphibolite whose protolith was a mafic cumulate. The foliated (cordierite-) leucogranitic dykes show a geochemical signature similar to that of the Moulin Blanc granite. They can thus be related to this pluton. Deformation, not only buoyancy, was the driving mechanism for their emplacement.

The 300 Ma Camarat equant granite emplaced shortly after the Moulin Blanc pluton, along an E–W direction. Dykes spatially associated to the granite show evidence of non-CHARAC behavior for some elements as frequently observed in highly evolved compositions. The high Rb content of the Camarat granite can be explained by dehydration melting of a metapelitic source at 875 °C and 7 kbar.

Field relationships indicate that the dolerite dykes are penecontemporaneous with the Camarat granite. Although their major element compositions have been altered to various degrees, their immobile trace element signature points to an andesite–basalt nature. Dolerite dykes at the Pinet and Capon tips are associated with various amounts of granitic component in spectacular mingling relationships. The source of the granitic component of the Pinet dolerite is similar to that of the Moulin Blanc granite and could thus be the Saint-Tropez migmatitic gneiss (metagraywacke). The age of most inherited zircons in the Pinet granite corroborates this origin. The Capon granite is geochemically similar to a series of leucogranitic dykes cross-cutting the host migmatitic gneiss. The latter dykes could thus be able to emplace independently of the dolerite. The small thickness of some of these dykes precludes emplacement solely by buoyancy, a gas overpressure or a tectonic process being required. Analogous dykes in the Tanneron Massif have a monazite age similar to the Camarat granite, which supports the hypothesis that the dolerite dykes emplaced penecontemporaneously with the Camarat granite. The very high Rb/Sr and Rb/Ba ratios of the Capon granite and cross-cutting leucogranitic dykes suggest that these rocks result from the dehydration melting of a meta-arkose source rock.

The crustal source material at the origin of the granites and diorites matches the isotopic signature of the Variscan crust in the French Massif Central (Downes et al., 1990). The isotopic signature of the dolerite implies contamination of mantle material by a large amount of crustal component, either during crystallization or in a previous subduction event. The isotopic signature also suggests that Mesoproterozoic lithologies are absent in the crust affected by melting processes, as is also the case in terranes at the periphery of northern Gondwana.

Finally, the most remarkable feature of the Saint-Tropez granites and related dykes is the short time interval between the emplacement of the foliated Moulin Blanc granite and the late cross-cutting leucogranitic dykes. This implies that a hot zone developed in a

large-scale, orogen-parallel shear zone at the end of a transpressional regime.

## Acknowledgments

Egide Nzojibwami and Timothy Nzali have helped in collecting part of the data. Discussions in the field with Jacques Bellière, Robert Maquil, Hervé Diot and Steve Ayrton have been very rewarding. Bruno Scaillet and Pierre Barbey have kindly commented on some aspects of the research. Guy Bologne is thanked for his constant help and interest in the chemical analyses. The reviews of J.L. Vigneresse and an anonymous reviewer have greatly improved the quality of the manuscript.

## Appendix A

### *Major and trace elements*

Whole-rock analyses were performed by XRF on an ARL 9400 XP spectrometer and on a CGR Alpha-2020 semi-automatic spectrometer on lithium tetra- and metaborate glass disks (FLUORE-X65®), with matrix corrections following the Traill–Lachance algorithm (ARL) or the Norrish and Hutton (1969) method (CGR) (Bologne and Duchesne, 1991).

Selected samples were analyzed for REE, U, Th, Zr, Hf, Nb, Ta, and Ba by ICP-MS on a VG Elemental Plasma Quad PQ2 after alkali fusion, following the method described in Vander Auwera et al. (1998). All other trace elements were analyzed on an ARL 9400 XP spectrometer on pressed pellets. U, Th, Y, Nb, Zr, Rb, Sr, Ga, Zn, Cu, Ni, and Co were corrected for matrix effects by Compton peak monitoring. 56 international reference samples were used to calibrate the determinations. When XRF and ICP-MS determinations were available, comparison between the two methods was very good but ICP-MS values were preferred, particularly for diadochic pairs. A series of REE determinations were carried out by ICP-AES on an ARL 3510 sequential spectrometer after extraction on a DOWEX 50W-X8 cation-exchange column, a method described in Roelandts and Deblond (1992). The international reference samples ACE, GH, GSN, DRN and BEN were used to assess the accuracy of the method that varies between 3 and 4%. The reproducibility estimated on triplicate analyses is between 1 and 2%.

### *Sr and Nd isotopes*

Sr and Nd isotopic compositions (Table 4) have been obtained at the Royal Museum for Central Africa on an IsotopX GV Sector 54 multicollector thermo-ionization mass spectrometer (TIMS). The average $^{87}Sr/^{86}Sr$ ratio of the NBS SRM987 standard and $^{143}Nd/^{144}Nd$ ratio of the Rennes Nd standard during the period of analyses were $0.710276 \pm 7$ ($2\sigma$ on 12 measurements) and $0.511965 \pm 5$ ($2\sigma$ on 14 measurements), respectively. Sample ratios have been standardized to a value of 0.710250 for NBS987 and to 0.511963 for the Merck standard (corresponding to a La Jolla value of 0.511858). Data are given in Table 3.

**Table 7**
LA-ICP-MS U–Pb results for Moulin Blanc zircon and monazite (sample #89M55).

| Sample | Pb* (ppm) | Th (ppm) | U (ppm) | Th/U | $^{208}Pb/^{206}Pb$ | $^{207}Pb/^{206}Pb$ | ± (1s) | $^{207}Pb/^{235}U$ | ± (1s) | $^{206}Pb/^{238}U$ | ± (1s) | Rho | Apparent ages (Ma) | | | |
|---|---|---|---|---|---|---|---|---|---|---|---|---|---|---|---|---|
| | | | | | | | | | | | | | $^{206}Pb/^{238}U$ | ± (1s) | $^{207}Pb/^{206}Pb$ | ± (1s) |
| *Zircon* | | | | | | | | | | | | | | | | |
| #1-1 | 97 | 1842 | 2330 | 0.79 | – | 0.0527 | 0.0005 | 0.3437 | 0.0071 | 0.0473 | 0.0009 | 0.89 | 298 | 5 | 315 | 21 |
| #2-1 | 102 | 1253 | 2331 | 0.54 | – | 0.0524 | 0.0006 | 0.3429 | 0.0062 | 0.0474 | 0.0007 | 0.81 | 299 | 4 | 304 | 24 |
| #3-1 | 180 | 2408 | 4000 | 0.60 | – | 0.0535 | 0.0008 | 0.3500 | 0.0076 | 0.0475 | 0.0008 | 0.74 | 299 | 5 | 349 | 33 |
| #4-1 | 172 | 2569 | 3971 | 0.65 | – | 0.0535 | 0.0005 | 0.3513 | 0.0071 | 0.0477 | 0.0009 | 0.88 | 300 | 5 | 348 | 22 |
| #5-1 | 137 | 1896 | 3179 | 0.60 | – | 0.0541 | 0.0006 | 0.3561 | 0.0081 | 0.0477 | 0.0010 | 0.89 | 300 | 6 | 377 | 23 |
| #6-1 | 169 | 2099 | 3852 | 0.54 | – | 0.0535 | 0.0008 | 0.3524 | 0.0068 | 0.0478 | 0.0005 | 0.59 | 301 | 3 | 351 | 35 |
| #7-1 | 184 | 2812 | 4204 | 0.67 | – | 0.0528 | 0.0006 | 0.3488 | 0.0079 | 0.0479 | 0.0009 | 0.88 | 302 | 6 | 319 | 25 |
| #8-1 | 122 | 1122 | 2786 | 0.40 | – | 0.0528 | 0.0020 | 0.3498 | 0.0152 | 0.0481 | 0.0010 | 0.49 | 303 | 6 | 320 | 84 |
| #9-1 | 104 | 1913 | 2387 | 0.80 | – | 0.0519 | 0.0005 | 0.3455 | 0.0069 | 0.0483 | 0.0009 | 0.90 | 304 | 5 | 281 | 20 |
| #10-1 | 128 | 1549 | 2994 | 0.52 | – | 0.0528 | 0.0009 | 0.3552 | 0.0093 | 0.0488 | 0.0010 | 0.77 | 307 | 6 | 319 | 38 |
| #11-1 | 78 | 1797 | 1254 | 1.43 | – | 0.0525 | 0.0003 | 0.3479 | 0.0068 | 0.0481 | 0.0009 | 0.96 | 303 | 6 | 306 | 12 |
| #12-1 | 77 | 1853 | 1281 | 1.45 | – | 0.0522 | 0.0003 | 0.3448 | 0.0050 | 0.0479 | 0.0007 | 0.94 | 302 | 4 | 295 | 11 |
| #13-1 | 148 | 1589 | 2932 | 0.54 | – | 0.0522 | 0.0004 | 0.3411 | 0.0042 | 0.0474 | 0.0005 | 0.80 | 298 | 3 | 295 | 17 |
| #14-1 | 83 | 2002 | 1367 | 1.46 | – | 0.0529 | 0.0003 | 0.3473 | 0.0054 | 0.0476 | 0.0007 | 0.94 | 300 | 4 | 323 | 12 |
| #15-1 | 81 | 1858 | 1330 | 1.40 | – | 0.0522 | 0.0003 | 0.3491 | 0.0051 | 0.0485 | 0.0007 | 0.93 | 305 | 4 | 294 | 12 |
| #16-1 | 166 | 1198 | 3515 | 0.34 | – | 0.0535 | 0.0003 | 0.3532 | 0.0067 | 0.0479 | 0.0009 | 0.95 | 302 | 5 | 349 | 14 |
| #17-1 | 142 | 967 | 2991 | 0.32 | – | 0.0524 | 0.0008 | 0.3443 | 0.0066 | 0.0476 | 0.0006 | 0.65 | 300 | 4 | 304 | 33 |
| #18-1 | 103 | 1257 | 2071 | 0.61 | – | 0.0523 | 0.0003 | 0.3386 | 0.0053 | 0.0469 | 0.0007 | 0.91 | 296 | 4 | 300 | 15 |
| *Monazite* | | | | | | | | | | | | | | | | |
| #1-1 | 1597 | – | 2721 | – | 2.159 | 0.0511 | 0.0003 | 0.3359 | 0.0037 | 0.0476 | 0.0004 | 0.82 | 300 | 3 | 247 | 14 |
| #2-1 | 2346 | – | 4250 | – | 2.007 | 0.0516 | 0.0003 | 0.3370 | 0.0035 | 0.0474 | 0.0004 | 0.79 | 299 | 2 | 266 | 15 |
| #3-1 | 1795 | – | 2054 | – | 3.760 | 0.0532 | 0.0005 | 0.3482 | 0.0042 | 0.0474 | 0.0004 | 0.66 | 299 | 2 | 339 | 21 |
| #4-1 | 2114 | – | 3939 | – | 1.905 | 0.0511 | 0.0003 | 0.3345 | 0.0031 | 0.0474 | 0.0003 | 0.68 | 299 | 2 | 248 | 16 |
| #5-1 | 1825 | – | 3436 | – | 1.872 | 0.0519 | 0.0004 | 0.3417 | 0.0039 | 0.0477 | 0.0004 | 0.73 | 300 | 2 | 283 | 18 |
| #6-1 | 1782 | – | 2608 | – | 2.723 | 0.0514 | 0.0003 | 0.3367 | 0.0039 | 0.0475 | 0.0005 | 0.82 | 299 | 3 | 260 | 15 |
| #7-1 | 1930 | – | 2364 | – | 3.385 | 0.0516 | 0.0004 | 0.3406 | 0.0034 | 0.0478 | 0.0003 | 0.67 | 301 | 2 | 270 | 17 |
| #8-1 | 1563 | – | 2282 | – | 2.683 | 0.0525 | 0.0012 | 0.3444 | 0.0083 | 0.0476 | 0.0004 | 0.39 | 300 | 3 | 307 | 50 |
| #9-1 | 1710 | – | 2618 | – | 2.576 | 0.0515 | 0.0004 | 0.3370 | 0.0039 | 0.0474 | 0.0004 | 0.79 | 299 | 3 | 265 | 16 |
| #10-1 | 1300 | – | 1882 | – | 2.725 | 0.0513 | 0.0004 | 0.3396 | 0.0035 | 0.0480 | 0.0003 | 0.71 | 302 | 2 | 253 | 17 |
| #11-1 | 1212 | – | 1784 | – | 2.652 | 0.0518 | 0.0004 | 0.3452 | 0.0035 | 0.0483 | 0.0004 | 0.73 | 304 | 2 | 276 | 16 |
| #12-1 | 1432 | – | 1839 | – | 3.180 | 0.0517 | 0.0003 | 0.3443 | 0.0028 | 0.0483 | 0.0003 | 0.63 | 304 | 2 | 273 | 15 |
| #13-1 | 1846 | – | 2785 | – | 2.600 | 0.0518 | 0.0004 | 0.3383 | 0.0036 | 0.0474 | 0.0004 | 0.71 | 298 | 2 | 276 | 17 |
| #14-1 | 1865 | – | 2936 | – | 2.462 | 0.0520 | 0.0003 | 0.3390 | 0.0034 | 0.0472 | 0.0004 | 0.80 | 298 | 2 | 287 | 14 |
| #15-1 | 1975 | – | 3645 | – | 1.931 | 0.0521 | 0.0004 | 0.3396 | 0.0033 | 0.0473 | 0.0003 | 0.63 | 298 | 2 | 288 | 17 |
| #16-1 | 2107 | – | 2798 | – | 3.079 | 0.0519 | 0.0004 | 0.3391 | 0.0038 | 0.0474 | 0.0003 | 0.63 | 299 | 2 | 279 | 20 |

**Table 8**
SHRIMP U–Pb results for Pinet granite zircon (sample #92M11).

| Spot | % $^{206}Pb_c$ | ppm U | ppm Th | $^{232}Th/^{238}U$ | ppm $^{206}Pb^*$ | $^{206}Pb/^{238}U$ age[a] | $^{207}Pb/^{206}Pb$ age[a] | % discordant | Total $^{238}U/^{206}Pb$ | ± % | Total $^{207}Pb/^{206}Pb$ | ± % | $^{238}U/^{206}Pb^{*,a}$ | ± % | $^{207}Pb^*/^{206}Pb^{*,a}$ | ± % | $^{207}Pb^*/^{235}U^a$ | ± % | $^{206}Pb^*/^{238}U^a$ | ± % | Err corr |
|---|---|---|---|---|---|---|---|---|---|---|---|---|---|---|---|---|---|---|---|---|---|
| 92M11.8.1 | 0.24 | 1321 | 237 | 0.19 | 53.3 | 295 ± 11 | 315 ± 47 | 7 | 21.31 | 3.6 | 0.05 | 1.1 | 21.36 | 3.6 | 0.05 | 2.1 | 0.340 | 4.2 | 0.05 | 3.6 | .869 |
| 92M11.1.1 | 0.36 | 319 | 93 | 0.30 | 13.6 | 311 ± 11 | 263 ± 130 | −16 | 20.13 | 3.7 | 0.05 | 2.2 | 20.2 | 3.7 | 0.05 | 5.9 | 0.351 | 6.9 | 0.05 | 3.7 | .534 |
| 92M11.9.1 | 0.83 | 354 | 149 | 0.44 | 14.8 | 304 ± 11 | 382 ± 110 | 26 | 20.56 | 3.7 | 0.06 | 2 | 20.73 | 3.7 | 0.05 | 4.7 | 0.361 | 6.0 | 0.05 | 3.7 | .615 |
| 92M11.10.1 | 0.23 | 1217 | 947 | 0.80 | 52.2 | 313 ± 11 | 325 ± 58 | 4 | 20.04 | 3.6 | 0.05 | 1.1 | 20.09 | 3.6 | 0.05 | 2.6 | 0.363 | 4.5 | 0.05 | 3.6 | .819 |
| 92M11.2.1 | – | 655 | 171 | 0.27 | 29.3 | 327 ± 12 | 325 ± 39 | −1 | 19.24 | 3.6 | 0.05 | 1.5 | 19.23 | 3.6 | 0.05 | 1.7 | 0.379 | 4.0 | 0.05 | 3.6 | .903 |
| 92M11.7.1 | 1.20 | 363 | 87 | 0.25 | 16.1 | 321 ± 12 | 1002 ± 98 | 212 | 19.36 | 3.7 | 0.08 | 1.6 | 19.59 | 3.7 | 0.07 | 4.8 | 0.510 | 6.1 | 0.05 | 3.7 | .608 |
| 92M11.6.1 | 1.81 | 327 | 6 | 0.02 | 17 | 371 ± 13 | 887 ± 110 | 139 | 16.57 | 3.7 | 0.08 | 1.6 | 16.87 | 3.7 | 0.07 | 5.3 | 0.560 | 6.5 | 0.06 | 3.7 | .570 |
| 92M11.5.1 | – | 784 | 239 | 0.31 | 53.9 | 497 ± 17 | 546 ± 41 | 10 | 12.51 | 3.6 | 0.06 | 1.1 | 12.49 | 3.6 | 0.06 | 1.9 | 0.645 | 4.1 | 0.08 | 3.6 | .888 |
| 92M11.3.1 | 0.00 | 991 | 388 | 0.40 | 73 | 530 ± 18 | 505 ± 20 | −5 | 11.67 | 3.6 | 0.06 | 0.9 | 11.67 | 3.6 | 0.06 | 0.9 | 0.677 | 3.7 | 0.09 | 3.6 | .971 |
| 92M11.4.1 | 0.14 | 195 | 116 | 0.62 | 28.6 | 1015 ± 35 | 1014 ± 39 | 0 | 5.85 | 3.7 | 0.07 | 1.3 | 5.86 | 3.7 | 0.07 | 1.9 | 1.717 | 4.2 | 0.17 | 3.7 | .887 |

Errors are 1-sigma; $Pb_c$ and $Pb^*$ indicate the common and radiogenic portions, respectively.
Error in standard calibration was 1.43%.
[a] Common Pb corrected using measured $^{204}Pb$.

*Zircon and monazite*

*LA-ICP-MS U–Pb zircon and monazite dating*

The sample selected for laser ablation U–Th–Pb geochronology was processed by crushing, heavy liquid and magnetic separation following conventional techniques. Zircons and monazites from the non magnetic fractions were hand-picked and mounted along with chips of the G91500 zircon standard (Wiedenbeck et al., 1995) onto an adhesive tape. The grains were then enclosed in epoxy resin and polished to expose internal structures. Laser ablation analyses were conducted using a Geolas platform housing a 193 nm CompEx 102 laser from LambdaPhysik, which was connected to an Element XR ICP-MS from ThermoFinnigan at Géosciences Montpellier UMR5243-CNRS (France). Details of the analytical procedure are described in Bosch et al. (2011) and Bruguier et al. (2009), and are only briefly summarized below. Data were acquired in the peak-jumping mode with the laser operating at an energy density of 12 J $cm^{-2}$ and a frequency of 3 Hz for zircon and 2 Hz for monazite. The laser spot size was 26 μm. Measured isotopic ratios were monitored with reference to the G91500 zircon standard (Wiedenbeck et al., 1995) and Managotry monazite (Poitrasson et al., 2000). Pb/Pb ratios in the unknown were mass-bias corrected using a power law whose parameters were determined by repetitive analysis of the reference material measured during the whole analytical session. This mass bias factor was used to correct the $^{207}Pb/^{206}Pb$ ratios measured on the unknown and its associated error was added in quadrature to the $^{207}Pb/^{206}Pb$ ratios measured on each unknown following the procedure described in Horstwood et al. (2003). Inter-element fractionation for U and Pb is more sensitive to analytical conditions and the Pb/U ratios of each batch of five unknowns were calibrated against the bias factor calculated using four standards bracketing the five unknowns. The mean Pb/U ratio of the four measured standards was used to calculate the inter-element fractionation and its error was then added in quadrature to the individual error measured on each $^{206}Pb/^{238}U$ unknown. Reproducibility of the standard Pb/U ratio was 0.9% (RSD; n = 24) for the whole LA-ICP-MS session required to analyze the samples and mass bias was 0.21%. Accurate common lead correction is difficult to achieve, mainly because of the isobaric interference of $^{204}Hg$ on $^{204}Pb$. The contribution of $^{204}Hg$ on $^{204}Pb$ was estimated by measuring the $^{202}Hg$ and assuming a $^{204}Hg/^{202}Hg$ natural isotopic composition of 0.2298. This allows monitoring the common lead content of the analyzed grain, but corrections often result in spurious ages. Analyses yielding $^{204}Pb$ were thus rejected and Table 7 reports only analyses for which no $^{204}Pb$ was detected. Quoted ratios correspond to measured ratios corrected from background and mass discrimination (+ elemental fractionation for the $^{206}Pb/^{238}U$ ratios). All ages have been calculated using the U and Th decay constants recommended by Steiger and Jäeger (1977). Analytical data were plotted and ages were calculated using the IsoplotEx program (Ludwig, 2000). Individual analyses in the data of Table 7 and in concordia plots are ±1σ errors and uncertainties in ages are quoted in the text at the 2σ level.

*SHRIMP*

Zircon grains were hand selected and mounted in epoxy resin, together with chips of the TEMORA (Middledale Gabbroic Diorite, New South Wales, Australia, age = 417 Ma (Black and Kamo, 2003)) and 91500 (Geostandard zircon, age = 1065 Ma, Wiedenbeck et al. (1995)) reference zircons. The grains were sectioned approximately in half and polished. Each analysis consisted of 5 scans through the mass range; the spot diameter was about 18 μm and the primary beam intensity was about 4 nA. The data were reduced in a manner similar to that described by Williams (1998) and references therein), using the SQUID Excel Macro of Ludwig (2000). The Pb/U ratios were normalized relative to a value of 0.0668 for the $^{206}Pb/^{238}U$ ratio of the TEMORA zircon, equivalent to an age of 416.75 Ma (Black and Kamo, 2003). Uncertainties given for individual analyses (ratios and ages) in Table 8 are at the 1σ level,

whereas uncertainties in calculated concordia ages are reported at the 2σ level.

## References


Amenzou, M., 1988. Les granitoïdes hercyniens du massif des Maures (Var, France). Etude géologique et minéralogique. Implications génétiques. University of Nice (280 pp.).

Amenzou, M., Pupin, J.-P., 1986. Le granite de Camarat (Maures, Var, France): un ensemble polygénique, zone clé entre la Provence et la Corse. Comptes Rendus Académie Sciences Paris (série IIa) 303 (8), 697–700.

Annen, C., Blundy, J., Sparks, R., 2006. The genesis of intermediate and silicic magmas in deep crustal hot zones. Journal of Petrology 47 (3), 505–539.

Avigad, D., Gerdes, A., Morag, N., Bechstädt, T., 2012. Coupled U–Pb–Hf of detrital zircons of Cambrian sandstones from Morocco and Sardinia: implications for provenance and Precambrian crustal evolution of North Africa. Gondwana Research 21, 690–703.

Ballèvre, M., Bosse, V., Ducassou, C., Pitra, P., 2009. Palaeozoic history of the Armorican Massif: models for the tectonic evolution of the suture zones. Comptes Rendus Géoscience 341, 174–201.

Barbey, P., 2009. Layering and schlieren in granitoids: a record of interactions between magma emplacement, crystallization and deformation in growing plutons. Geologica Belgica 12 (3–4), 109–133.

Bau, M., 1996. Controls on the fractionation of isovalent trace elements in magmatic and aqueous systems: evidence from Y/Ho, Zr/Hf, and lanthanide tetrad effect. Contributions to Mineralogy and Petrology 123, 323–333.

Bea, F., Fershtater, G., Corretgé, L.G., 1992. The geochemistry of phosphorus in granite rocks. Lithos 29, 43–56.

Bea, F., Pereira, M., Stroh, A., 1994. Mineral/leucosome trace-element partitioning in a peraluminous migmatite (a laser ablation-ICP-MS study). Chemical Geology 117, 291–312.

Bellot, J.-P., 2005. The Palaeozoic evolution of the Maures massif (France) and its potential correlation with other areas of the Variscan belt: a review. Journal of the Virtual Explorer 19 (paper 4).

Besson, M., Fonteilles, M., 1974. Relations entre les comportements contrastés de l'alumine et du fer dans la différenciation des séries tholéitique et calco-alcalines. Bulletin Société française de Minéralogie et Cristallographie 97, 445–449.

Black, L., Kamo, S., 2003. TEMORA 1: a new zircon standard for U–Pb geochronology. Chemical Geology 200, 155–170.

Bogaerts, M., Scaillet, B., Liégeois, J.P., Vander Auwera, J., 2003. Petrology and geochemistry of the Lyngdal granodiorite (Souther Norway) and the role of fractional crystallization in the genesis of the Proterozoic ferro-potassic A-type granites. Precambrian Research 124, 149–184.

Bologne, G., Duchesne, J.C., 1991. Analyse des roches silicatées par spectrométrie de fluorescence X: précision et exactitude. Belgian Geological Survey Professional Paper 249, 1–11.

Bordet, P., Guierard, S., Nesteroff, W., 1967. Carte géologique de la France au 1/50000, feuille n°1047 (St-Tropez-Cap Lardier). B.R.G.M., Orléans. Notice explicative anonyme (1967), 12 pp.

Bosch, D., et al., 2011. Building an island-arc crustal section: time constraints from a LA-ICP-MS zircon study. Earth and Planetary Science Letters 309, 268–279.

Boudreau, 1999. PELE — a version of the MELTS software program for the PC platform. Computers & Geosciences 25, 201–203.

Brichau, S., Respaut, J., Monié, P., 2008. New age constraints on emplacement of the Cévenol granitoids, South French Massif Central. International Journal of Earth Science 97, 725–738.

Bruguier, O., et al., 2003a. Application of in situ zircon geochronology and accessory phase chemistry to constraining basin development during post-collisional extension: a case study from the French Massif Central. Chemical Geology 201, 319–336.

Bruguier, O., Becq-Giraudon, J., Clauer, N., Maluski, H., 2003b. From late Visean to Stephanian: pinpointing a two-scale basinal evolution in the Variscan belt. A case study from the Bosmoreau basin (French Massif Central) and its geodynamic implications. International Journal of Earth Science 92, 338–347.

Bruguier, O., Hammor, D., Bosch, D., Caby, R., 2009. Miocene incorporation of peridotite into the Hercynian basement of the Maghrebides (Edough massif, NE Algeria): implications for the geodynamic evolution of the Western Mediterranean. Chemical Geology 261, 172–184.

Burgisser, A., Bergantz, G., 2011. A rapid mechanism to remobilize and homogenize highly crystalline magma bodies. Nature 471, 212–215.

Carosi, R., Montomoli, C., Tiepolo, M., Frassi, C., 2012. Geochronological constraints on post-collisional shear zones in the Variscides of Sardinia (Italy). Terra Nova 24, 42–51.

Cavazza, W., Roure, F., Spakman, W., Stampfli, G., Ziegler, P., 2004. The TRANSMED Atlas. The Mediterranean Region from Crust to Mantle. Springer, Berlin, Heidelberg, New York.

Clemens, J., Mawer, C., 1992. Granitic magma transport by fracture propagation. Tectonophysics 204, 339–360.

Clemens, J.D., Vielzeuf, D., 1987. Constraints on melting and magma production in the crust. Earth and Planetary Science Letters 86, 287–306.

Clemens, J., et al., 2010a. Sixth Hutton symposium on the origin of granites and related rocks. Geological Society of America Special Series.

Clemens, J., Helps, P., Stevens, G., 2010b. Chemical structure in granitic magmas — a signal from the source. Earth and Environmental Science Transactions of the Royal Society of Edinburg 100, 159–172.

Cocherie, A., Rossi, P., Fouillac, A.M., Vidal, P., 1994. Crust and mantle contributions to granite genesis: an example from the Variscan batholith of Corsica, studied by trace element and Nd–Sr–O isotope systematics. Chemical Geology 115, 173–211.

Cocks, L., Torsvik, T., 2006. European geography in a global context from the Vendian to the end of the Palaeozoic. In: Gee, D., Stephenson, R. (Eds.), European Lithosphere Dynamics: Geological Society London Memoirs, pp. 83–95.

Corsini, M., Rolland, Y., 2009. Late evolution of the southern European Variscan belt: exhumation of the lower crust in a context of oblique convergence. Comptes Rendus Géoscience 341, 214–223.

Debon, F., Le Fort, P., 1988. A cationic classification of common plutonic rocks and their magmatic associations: principles, method, applications. Bulletin de Mineralogie 111, 493–510.

Demoux, A., Schärer, U., Corsini, M., 2008. Variscan evolution of the Tanneron massif, SE France, examined through U–Pb monazite ages. Journal of the Geological Society of London 165, 467–478.

Downes, H., Dupuy, C., Leyreloup, A., 1990. Crustal evolution of the Hercynian belt of Western Europe: evidence from lower-crustal granulitic xenoliths (French Massif Central). Chemical Geology 83, 209–231.

Duchesne, J.-C., et al., 2008. Post-collisional melting of crustal sources: constraints from geochronology, petrology and Sr, Nd isotope geochemistry of the Variscan Sichevita and Poniasca granitoid plutons (South Carpathians, Romania). International Journal of Earth Sciences 97, 705–723.

Ennih, N., Liégeois, J., 2008. The boundaries of the West African craton, with a special reference to the basement of the Moroccan metacratonic Anti-Atlas belt. In: Ennih, N., Liégeois, J. (Eds.), The Boundaries of the West African Craton: Geological Society of London, Special Publications, pp. 1–17.

Ewart, A., Griffin, W., 1994. Application of proton microprobe data for determination of partition coefficients for selected elements in volcanic rocks. Chemical Geology 117, 251–284.

Fernandez, A., Gasquet, D., 1994. Relative rheological evolution of chemically contrasted coeval magmas: example of the Tichka plutonic complex (Morocco). Contributions to Mineralogy and Petrology 116, 316–326.

Fezaa, N., et al., 2010. Late Ediacaran geological evolution (575–555 Ma) of the Djanet Terrane, Eastern Hoggar, Algeria, evidence for a Murzukian intracontinental episode. Precambrian Research 180, 299–327.

Franke, W., 1989. Tectonostratigraphic units in the Variscan belt of central Europe. In: Dallmeyer, R. (Ed.), Terranes in the Circum-Atlantic Palaeozoic Ocean: Geological Society of America, Special Papers, 230, pp. 67–90.

Frost, T., Mahood, G., 1987. Field, chemical and physical constraints on mafic–felsic magma interaction in the Lamarck Granodiorite, Sierra Nevada, California. Geological Society of America Bulletin 99, 272–291.

Frost, B.R., et al., 2001. A geochemical classification for granitic rocks. Journal of Petrology 42, 2033–2048.

Geoffroy, L., Angelier, J., 1995. Existence de dykes en tension-cisaillement: définition et interprétation mécanique. Comptes Rendus Académie des Sciences de Paris (série IIa) 321, 505–511.

Giordano, D., Russel, J., Dingwell, D., 2008. Viscosity of magmatic liquid: a model. Earth and Planetary Science Letters 271 (1–4), 123–134.

Glazner, A., Bartley, J., Coleman, D., Gray, W., Taylor, R., 2004. Are plutons assembled over millions of years by amalgamation from small magma chambers? GSA Today 14, 4–11.

Grant, J.A., 1986. The isocon diagram — a simple solution to Gresens's equation for metasomatic alteration. Economic Geology 81, 1976–1982.

Guillot, S., Ménot, R.-P., 2009. Paleozoic evolution of the external crystalline massifs of the Western Alps. Comptes Rendus Geosciences 341, 253–265.

Harris, N.B.W., Inger, S., 1992. Trace element modelling of pelite-derived granites. Contributions to Mineralogy and Petrology 110, 46–56.

Harrison, T.M., Watson, E.B., 1984. The behavior of apatite during crustal anatexis: equilibrium and kinetic considerations. Geochimica et Cosmochimica Acta 48, 1467–1477.

Heiken, G., Eichelberger, J.C., 1980. Eruptions at Chaos Crags, Lassen Volcanic National Parks, California. Journal of Volcanology and Geothermal Research 7, 443–481.

Henderson, P., 1982. Inorganic Geochemistry. Pergamon, Oxford.

Holtz, F., Johannes, W., 1994. Maximum and minimum water content of granitic melts — implications for chemical and physical properties of ascending magmas. Lithos 32, 149–159.

Horstwood, M., Foster, G., Parrish, R., Noble, S., Nowell, G., 2003. Common-Pb corrected in situ U–Pb accessory mineral geochronology by LA-MC–ICPMS. Journal of Analytical Atomic Spectrometry 18, 837–846.

Innocent, C., Michard, A., Guerrot, C., Hamelin, B., 2003. U–Pb zircon age of 548 Ma for the leptynites (high-grade felsic rocks) of the central part of the Maures massif. Geodynamic significance of the so-called leptynoamphibolitic complexes of the Variscan belt in western Europe. Bulletin de la Société Géologique de France 174, 585–594.

Irber, W., 1999. The lanthanide tetrad effect and its correlation with K/Rb, Eu/Eu*, Se/Eu, Y/Ho and Zr/Hf of evolving peraluminous granite suites. Geochimica et Cosmochimica Acta 63 (3–4), 489–508.

Jahn, B.M., et al., 2001. Highly evolved juvenile granites with tetrad REE patterns: the Woduhe and Baerzhe granites from the Great Xing'an Mountains in NE China. Lithos 59, 171–198.

Johannes, W., Holtz, F., 1996. Petrogenesis and Experimental Petrology of Granitic Rocks. Minerals and Rocks. Springer.

Jung, S., Hoernes, S., Mezger, K., 2002. Synorogenic melting of mafic lower crust: constraints from geochronology, petrology and Sr, Nd, Pb and O isotope geochemistry of quartz diorites (Damara orogen, Namibia). Contributions to Mineralogy and Petrology 143, 551–566.

Lachenbruch, A.H., Sass, J.H., Galanis Jr., S.P., 1985. Heat flow in southernmost California and the origin of the Salton trough. Journal of Geophysical Research 90, 6709–6736.
Lapierre, H., Basile, C., Dupuis, V., 1999. Permian basalts and trachytes from Esterel (SE France): a transitional tholeiitic suite emplaced during lithosphere thinning. Bulletin de la Société Géologique de France, 170.
Liégeois, J., Stern, R., 2010. Sr–Nd isotopes and geochemistry of granite–gneiss complexes from the Meatiq and Hafafit domes, Eastern Desert, Egypt: No evidence for pre-Neoproterozoic crust. Journal of African Earth Sciences 57, 31–40.
Liégeois, J.P., Navez, J., Hertogen, J., Black, R., 1998. Contrasting origin of post-collisional high-K calc-alkaline and shoshonitic versus alkaline and peralkaline granitoids. Lithos 45, 1–28.
Linnen, R., Keppler, H., 1997. Columbite solubility in granitic melts: consequences for the enrichment and fractionation of Nb and Ta in the Earth's crust. Contributions to Mineralogy and Petrology 128, 213–227.
Linnen, R., Keppler, H., 2002. Melt composition control of Zr/Hf fractionation in magmatic processes. Geochimica et Cosmochimica Acta 66 (18), 3293–3301.
Lofgren, G., 1980. Experimental studies on the dynamic crystallization of silicate melts. In: Hargraves, R.B. (Ed.), Physics of Magmatic Processes. Princeton University Press, Princeton, pp. 487–551.
Ludwig, K., 2000. SQUID 1.00: a user's manual. Berkeley Geochronology Center Special Publication, 2, pp. 1–19.
Martin, H., 1987. Petrogenesis of Archaean trondhjemites, tonalites and granodiorites from Eastern Finland: major and trace element geochemistry. Journal of Petrology 28, 921–953.
Matte, P., 1986. Tectonics and plate tectonic model for the Variscan belt of Europe. Tectonophysics 126, 329–374.
Matte, P., 2001. The Variscan collage and orogeny (480–290 Ma) and the tectonic definition of the Armorica microplate: a review. Terra Nova 13 (2), 129–134.
McBirney, A.R., Murase, T., 1984. Rheological properties of magmas. Annual Reviews of Earth and Planetary Sciences 12, 337–357.
Melleton, J., Cocherie, A., Faure, M., Rossi, P., 2009. Precambrian protoliths and Early Paleozoic magmatism in the French Massif Central: U–Pb data and the North Gondwana connection in the west European Variscan belt. Gondwana Research 17, 13–25.
Miller, C., et al., 2011. Growth of plutons by incremental emplacement of sheet in crystal-rich host: evidence from Miocene intrusions of the Colorado River region, Nevada, USA. Tectonophysics 500, 65–77.
Montel, J., Vielzeuf, D., 1997. Partial melting of metagreywackes, Part II. Compositions of minerals and melts. Contributions to Mineralogy and Petrology 128, 176–196.
Morillon, A.C., et al., 2000. Diachronous cooling on both sides of a major strike slip fault in the Variscan Maures Massif (south-east France), as deduced from a detailed 40Ar/39Ar study. Tectonophysics 321, 103–126.
Moussavou, M., 1998. Contribution à l'histoire thermo-tectonique varisque du massif des Maures, par la typologie du zircon et la géochronologie U/Pb sur des minéraux accessoires, Doctorat thesis, Montpellier University, Montpellier.
Nash, W.P., Crecraft, H.R., 1985. Partition coefficients for trace elements in silicic magmas. Geochimica et Cosmochimica Acta 49, 2309–2322.
Nelson, B.K., DePaolo, D.J., 1985. Rapid production of continental crust 1.7 to 1.9 b.y. ago: Nd isotopic evidence from the basement of the North American mid-continent. Geological Society of America Bulletin 96, 746–754.
Norrish, K., Hutton, J.T., 1969. An accurate X-ray spectrographic method for the analysis of a wide range of geological samples. Geochimica et Cosmochimica Acta 33, 431–453.
Onézime, J., Faure, M., Crévola, G., 1999. Etude pétro-structurale du complexe granitique Rouet — Plan-de-la-Tour (massif des Maures et du Tanneron occidental, Var). Comptes Rendus Académie Sciences de Paris, Sciences de la Terre et des Planètes 328, 773–779.
Orejana, D., Villaseca, C., Valverde-Vaquero, P., Belousova, E., Armstrong, R., 2012. U–Pb geochronology and zircon composition of the late Variscan S- and I-type granitoids from the Spanish Central System batholith. International Journal of Earth Science 101, 1789–1815.
Pearce, J.A., 1983. Role of sub-continental lithosphere in magma genesis at active continental margins. In: Hawkesworth, C.L., Norry, M.J. (Eds.), Continental Basalts and Mantle Xenoliths. Shiva, Nantwich, pp. 230–249.
Pearce, J., 1996. Sources and settings of granitic rocks. Episodes 19 (4), 120–125.
Petford, N., Atherton, M., 1996. Na-rich partial melts from newly underplated basaltic crust: the Cordillera Blanca Batholith, Peru. Journal of Petrology 37, 1491–1521.
Petford, N., Kerr, R.C., Lister, J.R., 1993. Dike transport of granitoid magmas. Geology 21, 845–848.
Petford, N., Lister, J., Kerr, R., 1994. The ascent of felsic magmas in dykes. Lithos 32, 161–168.
Petford, N., Cruden, A., McCaffrey, K., Vigneresse, J.-L., 2000. Granite magma formation, transport and emplacement in the Earth's crust. Nature 408, 669–673.
Pierre, D., 1979. Géochimie et pétrologie des gneiss migmatitiques et des amphibolites de la presqu'île de Saint-Tropez, massif des Maures, Var, France, MSc thesis, University of Liège, (65 pp.).
Platt, J.P., England, P.C., 1994. Convective removal of lithosphere beneath mountain belts: thermal and mechanical consequences. American Journal of Science 294, 307–336.
Poitrasson, F., Chenery, S., Shepperd, T., 2000. Electron microprobe and LA-ICP-MS study of monazite hydrothermal alteration: implications for U–Th–Pb geochronology and nuclear ceramics. Geochimica et Cosmochimica Acta 64, 3283–3297.
Rapp, R.P., Watson, E.B., 1995. Dehydration melting of metabasalt at 8–32 kbar: implications for continental growth and crust–mantle recycling. Journal of Petrology 36, 891–932.
Roelandts, I., Deblond, A., 1992. Rare-earth element composition of Devonian sediments from southern Belgium. Application of an inductively coupled plasma atomic emission-spectrometry method. Chemical Geology 95, 167–176.
Rolland, Y., Corsini, M., Demoux, A., 2009. Metamorphic and structural evolution of the Maures–Tanneron massif (SE Variscan chain): evidence of doming along a transpressional margin. Bulletin de la Société Géologique de France 180, 217–230.
Roubault, M., Bordet, P., Leutwein, F., Sonet, J., Zimmermann, J., 1970. Ages des formations cristallophylliennes des massifs des Maures et du Tanneron. Comptes Rendus Académie des Sciences de Paris (série D) 271, 1067–1070.
Rouire, J. et al., 1979a. Carte géologique de la France à 1/250000, feuille n°40 (Nice). B.R.G.M., Orléans. Notice explicative par J. Rouire, A. Autran, A. Prost, J. Rossi, C. Rousset (1980), (94 pp.).
Rouire, J., L'Homer, A., Blanc, J., Gabert, J., 1979b. Carte géologique de la France à 1/250000, feuille n°39 (Marseille). B.R.G.M., Orléans, Notice explicative par J. Rouire, J.J. Blanc (1979), (88 pp.).
Rushmer, T., 1991. Partial melting of two amphibolites: contrasting experimental results under fluid absent conditions. Contributions to Mineralogy and Petrology 107, 41–59.
Sawyer, E., 2008. Atlas of migmatites. The Canadian Mineralogist, Special Publication, 9. NRC Research Press, Ottawa, Ontario, Canada.
Scaillet, B., Whittington, A., Martel, C., Pichavant, M., Holtz, F., 1999. Phase equilibrium constraints on the viscosity of silicic magmas. II. Implications for mafic–silicic mixing processes. Transactions of the Royal Society of Edinburgh, Earth Sciences 99 (1–2), 61–72.
Skjerlie, K., Johnston, A.D., 1996. Vapor-absent melting from 10 to 20 kbar of crustal rocks that contain multiple hydrous phases: implications for anatexis in the deep to very deep continental crust and active continental margins. Journal of Petrology 37, 661–691.
Sparks, R.S.J., Marshall, L.A., 1986. Thermal and mechanical constraints on mixing between mafic and silicic magmas. Journal of Volcanology and Geothermal Research 29, 99–124.
Steiger, R., Jäeger, E., 1977. Subcommission on geochronology: convention on the use of decay constants in geo- and cosmo-chronology. Earth and Planetary Science Letters 36, 359–362.
Stern, R., et al., 2010. Distribution and significance of Pre-Neoproterozoic zircons in juvenile Neoproterozoic igneous rocks of the Arabo-Nubian Shield. American Journal of Science 310, 791–811.
Sun, S.S., McDonough, W.F., 1989. Chemical and isotopic systematics of oceanic basalts: implications for mantle composition and processes. In: Saunders, A.D., Norry, M.J. (Eds.), Magmatism in Ocean Basins: Geological Society of London Special Publication, pp. 313–345.
Sylvester, P.J., 1989. Post-collisional alkaline granites. Journal of Geology 97, 261–280.
Sylvester, P., 1998. Post-collisional strongly peraluminous granites. Lithos 45, 29–44.
Teyssier, C., Tikoff, B., 1998. Strike-slip partitioned transpression of the San Andreas fault system: a lithospheric-scale approach. In: Holdworth, R.E., Strachan, R.A., Dewey, J. (Eds.), Continental Transpressional and Transtensional Tectonics: Geological Society of London Special Publication, pp. 143–158.
Toutin-Morin, N., Bonijoly, D., Brocard, C., Dardeau, G., Dubar, M., 1993. The sedimentary record of post-Hercynian evolution along the edge of the Maures and Tanneron Massifs from the late Carboniferous to the present. Géologie de la France 2, 3–22.
Vander Auwera, J., Bologne, G., Roelandts, I., Duchesne, J.C., 1998. Inductively coupled plasma-mass spectrometry (ICP-MS) analysis of silicate rocks and minerals. Geologica Belgica 1 (1), 49–53.
Vander Auwera, J., et al., 2003. Derivation of the 1.0–0.9 Ga ferro-potassic A-type granitoids of southern Norway by extreme differentiation from basic magmas. Precambrian Research 124, 107–148.
Vauchez, A., Bufalo, M., 1988. Charriage crustal, anatexie et décrochemenr ductiles dans les Maures orientales (Var, France) au cours de l'orogenèse varisque. Geologische Rundschau 77 (1), 45–62.
Vielzeuf, D., Holloway, J., 1988. Experimental determination of the fluid-absent melting relations in the pelitic system. Contributions to Mineralogy and Petrology 98, 257–276.
Vielzeuf, D., Montel, J., 1994. Partial melting of metagreywackes. Part 1. Fluid-absent experiments and phase relationships. Contributions to Mineralogy and Petrology 117, 375–393.
Vigneresse, J.-L., 2004. Toward a new paradigm for granite generation. Transactions Royal Society of Edinburgh, Earth Sciences 95, 11–22.
Vigneresse, J.L., 2007. The role of discontinuous magma inputs in felsic magma and ore generation. Ore Geology Reviews 30, 181–216.
Vigneresse, J.-L., Barbey, P., Cuney, M., 1996. Rheological transitions during partial melting and crystallization with application to felsic magma segregation and transfer. Journal of Petrology 37 (6), 1579–1600.
von Raumer, J.F., Stampfli, G.M., Borel, G., Bussy, F., 2002. Organization of pre-Variscan basement areas at the north-Gondwana margin. International Journal of Earth Science 91, 35–52.
Watson, E.B., Harrison, T.M., 1983. Zircon saturation revisited: temperature and compositional effects in a variety of crustal magma types. Earth and Planetary Science Letters 64, 295–304.
Wiebe, R.A., Blair, K.D., Hawkins, D.P., Sabine, C.P., 2002. Mafic injections, in situ hybridization, and crustal accumulation in the Pyramid Peak granite, California. Geological Society of America Bulletin 114 (7), 909–920.
Wiedenbeck, M., et al., 1995. Three natural zircon standards for U–Th–Pb, Lu–Hf, trace element and REE analyses. Geostandards Newsletters 19, 1–23.
Williams, I., 1998. U–Th–Pb geochronology by ion microprobe. In: McKibben, M., Shanks III, W., Ridley, W. (Eds.), Applications of Microanalytical Techniques to Understanding Mineralizing Processes: Review in Economic Geology, pp. 1–35.
Wilmart, E., et al., 1984. Modèle géochimique des sédiments paléozoïques du sud de la Belgique. Méthodologie pour l'étude des matériaux pélitiques. Fonds de la Recherche Fondamentale Collective, Programme d'initiative ministérielle n°112.
Wilson, M., 1988. Igneous Petrogenesis. Unwin Hyman, London.
Winchester, J.A., Floyd, P.A., 1977. Geochemical determination of different magma series and their differentiation products using immobile elements. Chemical Geology 20, 325–343.
Zheng, J.S., et al., 1992. Datation $^{40}Ar/^{39}Ar$ du magmatisme et de filons minéralisés permiens en Provence Orientale (France). Geodinamica Acta 5 (3), 203–215.